# Impact of noble-gas filler atoms on the lattice thermal conductivity of CoSb$_3$ skutterudites: first-principles modelling

Jianqin Tang[1] and Jonathan M. Skelton[1*]

[1] Department of Chemistry, University of Manchester, Oxford Road, Manchester M13 9PL, UK
[*] Corresponding author. E-Mail: jonathan.skelton@manchester.ac.uk.

**Abstract**

We present a systematic first-principles modelling study of the structural dynamics and thermal transport in the CoSb$_3$ skutterudites with a series of noble-gas filler atoms. Filling with chemically-inert atoms provides an idealised model for isolating the effects of the fillers from the impact of redox changes to the host electronic structure. A range of analysis techniques are proposed to estimate the filler rattling frequencies, to quantify the separate impacts of the filler on the phonon group velocities and lifetimes, and to show how changes to the phonon spectra and interaction strengths lead to suppressed lifetimes. The noble-gas fillers are found to reduce the thermal conductivity of the CoSb$_3$ framework by up to 15 % primarily by suppressing the group velocities of low-lying optic modes. The filler rattling frequencies are determined by a detailed balance of increasing atomic mass and stronger interactions with the framework, and are found to be a good predictor of the impact on the heat transport. Lowering the rattling frequency below ~1.5 THz by selecting heavy fillers that interact weakly with the framework is predicted to lead to a much larger suppression of the thermal transport, by inducing avoided crossings in the acoustic-mode dispersion and facilitating enhanced scattering and a consequent large reduction in phonon lifetimes. Approximate rattling frequencies determined from the harmonic force constants may therefore provide a useful metric for selecting filler atoms to optimise the thermal transport in skutterudites and other cage compounds such as clathrates.

# 1. Introduction

Mitigating climate change by switching to sustainable sources of energy and reducing global greenhouse gas emissions is among the most pressing scientific and technological challenges of the 21st century. As renewable energy technologies such as photovoltaics mature and fossil-fuel power plants are decommissioned, an increasingly large proportion of emissions come from energy-intensive industries and the automotive and transportation sectors.[1] An internal combustion engine wastes up to 60 % of its energy as heat, and by recent estimates ~10 % of the greenhouse gas emissions in Europe are from heavy-duty transport vehicles.[1] A coordinated approach to reducing emissions therefore requires technologies to improve the efficiency of existing energy-intensive processes alongside the expansion of primary renewables.

Thermeoelectric generators (TEGs) make use of the Seebeck effect in a thermoelectric material to extract energy from a temperature gradient and recover otherwise wasted heat as electrical energy, and are among the front-running technologies to meet this challenge. TEGs are solid-state devices with no moving parts, and can be deployed at scales from wireless sensors, to vehicle exhausts, to industrial plants, and possibly even as primary renewable power sources.[1] The large amount of global energy wasted as heat means that even modestly efficient TEGs could have a large impact on climate change - for example, a typical nuclear power plant loses ~60 % of its energy as waste heat, and a mere 5-10 % recovery would provide enough additional power for tens of thousands of homes.

The efficiency of a thermoelectric material is typically described using the dimensionless figure of merit $ZT$:[2]

$$ZT = \frac{S^2 \sigma T}{\kappa_{\text{latt}} + \kappa_{\text{el}}} \qquad (1)$$

where $S$ is the Seebeck coefficient, $\sigma$ is the electrical conductivity, the product $S^2\sigma$ is the power factor, and $\kappa_{\text{latt}}$ and $\kappa_{\text{el}}$ are the lattice (phonon) and electronic contributions to the thermal conductivity. $S$, $\sigma$ and $\kappa_{\text{el}}$ depend on the electronic structure and the carrier concentration, and are interdependent such that the $ZT$ at a target operating temperature is typically maximised in heavily-doped semiconductors. The bulk of the $\kappa_{\text{latt}}$ in semiconductors is from heat transport through phonons. This is largely independent of the electronic structure, and can be minimised to improve the $ZT$ using a variety of strategies spanning chemical doping and alloying, to including nanoscale phase impurities, to mesoscale structuring.[2]

The majority of the current flagship TEs are heavy p-block chalcogenides including PbTe, SnSe and the current industry standard $Bi_2Te_3$.[1] These systems have in common narrow bandgaps and favourable electronic transport, together with large intrinsic phonon anharmonicity leading to low $\kappa_{\text{latt}}$.[2,3] However, the constituent elements are rare and/or environmentally hazardous, which prohibits the large-scale adoption of TEGs based on these materials.

The desire for crystalline-like electron transport and amorphous (glass)-like heat transport is encapsulated by the "phonon glass electron crystal" (PGEC) concept originally put forward by Slack.[4] Among the most widely-studied PGEC materials are the skutterudites and inorganic clathrates,[5–9] which are "cage" compounds with large intrinsic cavities that can incorporate loosely-bound guest ions to act as phonon-scattering centres while electronic transport occurs through the crystalline host framework.

Skutterudite itself is the mineral $CoAs_3$, but the structure is adopted by a range of compositions with the formula $M_4X_{12}$, where M is a transition metal and X is one of the pnictogens P, As, or Sb. $CoSb_3$ has attracted the most attention as a potential high-performance TE due to its large Seebeck coefficient.[10–12] Pristine $CoSb_3$ has a low $ZT$ of just 0.05 at 723 K[12] due its high $\kappa_{latt}$, which can reach 10 W m$^{-1}$ K$^{-1}$ at room temperature in single crystals.[10,11] However, $CoSb_3$ is chemically very flexible and is amenable both to doping the host framework, e.g. with transition metals[13,14] and chalcogenides,[14] and to filling the cavities with atoms including alkali and alkaline earth metals,[15,16] Group III elements,[17] chalcogens,[18] halogens,[19] transition metals[20] and rare-earth elements.[21,22]. This extraordinary flexibility has led to the experimental synthesis of a wide variety of compounds including examples doped at the Co and Sb sites, incorporating up to seven filler atoms, and with concomitant doping and filling. Some compositions with notable improvements to the $ZT$ include $Ni_{0.3}Co_{3.7}Sb_{12}$ ($ZT = 0.52$ at 773 K),[23] $Na_{0.48}Co_3Sb_{12}$ ($ZT = 1.25$ at 800 K),[16] $Sr_{0.16}Yb_{0.03}Co_4Sb_{11.82}$ ($ZT = 1.32$ at 850 K),[24] $Ba_{0.08}La_{0.05}Yb_{0.04}Co_4Sb_{12}$ ($ZT = 1.7$ at 850 K),[25] $Yb_{0.2}Ba_{0.1}Al_{0.1}Ga_{0.1}In_{0.1}La_{0.05}Eu_{0.05}Co_4Sb_{12}$ ($ZT = 1.2$ at 800 K),[26] and $Ce_{0.12}Fe_{0.71}Co_{3.29}Sb12$ ($ZT = 0.8$ at 750 K).[27]

First-principles modelling of the structural dynamics and thermal transport, typically using density-functional theory (DFT), has been instrumental in understanding the intrinsically low $\kappa_{latt}$ of flagship thermoelectrics and other highly-anharmonic materials,[28–32] and has also been applied to identify novel candidate TEs.[33–35] Despite a large body of experimental work on the skutterudites, there are comparatively few modelling studies on the phonon thermal transport.[36–40] Guo *et al.* used first-principles lattice-dynamics calculations to study the thermal transport in $CoSb_3$ and to investigate the impact of nanostructuring and Sb → As substitution on the $\kappa_{latt}$.[39] Wu and Mingo used similar calculations to study fully-filled $BaCo_4Sb_{12}$ and $YbFe_4Sb_{12}$, and were able to establish the mechanisms by which these fillers suppress the heat transport,[36,38] and also to explain the higher $\kappa_{latt}$ of $IrSb_3$ relative to $CoSb_3$.[37] There are also a small number of modelling studies based on force-field techniques, for example using non-equilibrium molecular-dynamics simulations to explore the impact of Sb vacancies on the thermal transport in $CoSb_3$.[40]

More systematic modelling studies could provide valuable insight into the underlying microscopic mechanisms by which doping and filling reduce the $\kappa_{latt}$ and thereby direct future work to identify and optimise novel high-performance skutterudite TEs. In this study, we present a systematic set of calculations on $CoSb_3$ and $XCo_8Sb_{24}$ skutterudites filled with the noble gases X = He, Ne, Ar, Kr and Xe and explore the links between the size and mass of the filler atoms and their impact the thermal conductivity. By selecting chemically-inert filler atoms, we are able to isolate the effects of the fillers from the impact of changes to the electronic structure

of the host framework through the redox reactions that can occur with most other fillers. We propose and apply a variety of analysis techniques to elucidate the microscopic mechanisms by which the fillers suppress the heat transport through the $CoSb_3$ framework, and show that an approximate rattling frequency, determined from the atomic mass and harmonic force constants, is a good predictor of the effect of a filler on the $\kappa_{latt}$. The general conclusions and modelling techniques from this study are readily applicable to other filled skutterudites, and can help to improve our fundamental understanding of the heat transport in cage compounds and identify promising research directions towards future high-performance TEs.

## 2. Computational Modelling

Calculations were performed using pseudopotential plane-wave density-functional theory (DFT) as implemented in the Vienna *Ab initio* Simulation Package (VASP) code.[41] Calculations on pristine $CoSb_3$ were performed using the 32-atom conventional cell, while calculations on filled models were performed by placing a single filler ion X = He, Ne, Ar, Kr and Xe at the centre of one of the two cavities at (0.5, 0.5, 0.5). The filled models have the composition $XCo_8Sb_{24}$, corresponding to a filling fraction of 50 %.

The electronic structure was modelled using a plane-wave basis set with a 500 eV kinetic-energy cutoff and Γ-centered Monkhorst-Pack **k**-point meshes[42] with $4 \times 4 \times 4$ subdivisions. These values were determined from explicit testing to converge the total energy to < 0.1 meV atom$^{-1}$ and the external pressure to < 1 kbar (0.1 GPa). Electron exchange and correlation were modelled using the PBEsol generalised-gradient approximation (GGA) functional,[43] with a Hubbard $U$ correction of $U_{eff}$ = 5 eV applied to the Co 3d states using the rotationally-invariant Dudarev model.[44] Some additional tests were performed including the semi-empirical DFT-D3 dispersion correction.[45] Projector augmented-wave (PAW) pseudopotentials[46,47] were used to model the ion cores, with the following valence electron configurations: Co - $3p^64s^23d^7$, Sb - $5s^25p^3$, He - $1s^2$, Ne - $2s^22p^6$ Ar - $3s^23p^6$, Kr - $4s^24p^6$, and Xe - $5s^25p^6$. Tolerances of $10^{-8}$ eV and $10^{-2}$ eV Å$^{-1}$ were applied to the electronic wavefunctions and ionic forces during electronic structure solution and geometry optimisation, respectively. The PAW projection was performed in reciprocal space, non-spherical contributions to the gradient correction were included inside the PAW spheres, and the precision of the charge-density grids was automatically set to avoid aliasing errors.

Lattice-dynamics and thermal-conductivity calculations were performed using the Phonopy and Phono3py packages.[48,49] The second- and third-order interatomic force constants (IFCs) were determined using the supercell finite-displacement method[50] with displacement step sizes of $10^{-2}$ and $3 \times 10^{-2}$ Å respectively. The second-order IFCs were determined in $2 \times 2 \times 2$ supercells with 256/264 atoms, while the third-order IFCs were calculated in the base cells with 32/33 atoms. During the single-point force calculations an auxiliary charge-density grid with 8× the number of grid points was used to evaluate the forces, and the **k**-point sampling for the 256/264-atom supercells was reduced proportionately to $2 \times 2 \times 2$.

During post-processing, phonon density of states (DoS) curves $g(f)$ were computed by interpolating the frequencies onto a uniform Γ-centered grid with $48 \times 48 \times 48$ subdivisions and applying a Gaussian broadening with $\sigma$ = 0.032 THz, corresponding to a full-width at half-maximum of 2.5 cm$^{-1}$. Atom-projected

phonon DoS (PDoS) curves were computed on $24 \times 24 \times 24$ grids. For pristine $CoSb_3$ a transformation matrix was used to project to the primitive cell, and the grids were increased to $60 \times 60 \times 60$ and $30 \times 30 \times 30$, respectively, to account for the 2× larger Brillouin zone. The phonon dispersion of undoped $CoSb_3$ was obtained by evaluating the frequencies along paths connecting the high-symmetry wavevectors in the $Im\overline{3}$ Brillouin zone. The phonon dispersions of the filled models were referenced to the $CoSb_3$ primitive cell using the band-unfolding approach of Allen *et al*.[51] When calculating the thermal conductivity, the phonon Brillouin zones were sampled with $9 \times 9 \times 9$ meshes, and selected analyses were performed using smaller $7 \times 7 \times 7$ meshes. Additional data from the thermal-conductivity calculations, including a comparison of supercell sizes, an assessment of the numerical quality of the calculated force constants, and selection of appropriate sampling meshes, is given in Section 1 of the ESI.

## 3. Results and Discussion

*a. Pristine CoSb₃*

$CoSb_3$ is cubic with the $Im\overline{3}$ spacegroup. The 32-atom conventional unit cell (Fig. 1a) consists of eight corner-sharing $CoSb_6$ octahedra surrounding large cavities located at the corners and the centre of the cell (Fig. 1b). The optimised lattice constant of $a_0 = 8.952$ Å obtained using PBEsol + $U$ is within 1 % of typical experimental measurements of 9.035-9.039 Å.[11,52–54]

The calculated phonon dispersion and atom-projected density of states of $CoSb_3$ are shown in Fig. 2. The 16 atoms in the primitive cell produce $3N = 48$ branches at each phonon wavevector. The three acoustic modes span a frequency range of ~2.5 THz. The 48 modes can be partitioned into low- and high-frequency groups in a 3:1 ratio separated by a "phonon bandgap". The lower-frequency group extends up to ~6 THz, while the upper-frequency group spans from ~7-8.5 THz. With reference to the atom-projected phonon DoS, these bands can be assigned as predominantly vibrations involving Sb and Co motion respectively. Our results are a good match to experimental data[52,54,56,57] and to other modelling studies.[39]
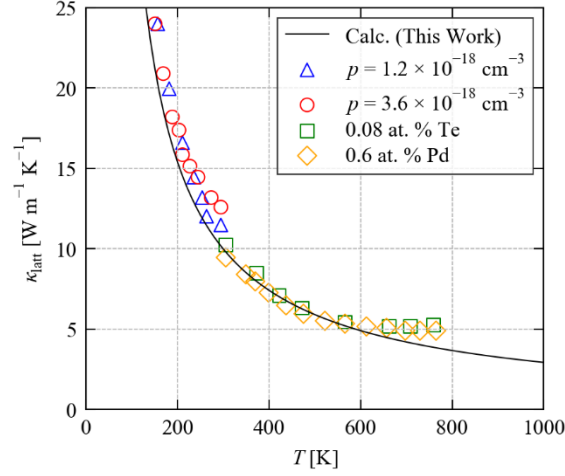
The lattice thermal conductivity $\kappa_{latt}$ as a function of temperature, calculated using the single-mode relaxation-time approximation (RTA) model, is shown in Fig. 3. The diagonal elements $\kappa_{xx}$, $\kappa_{yy}$ and $\kappa_{zz}$ of the $3 \times 3$ $\kappa_{latt}$ tensor correspond to the transport along the principal Cartesian directions. In a cubic system, the diagonal elements are equal, so for simplicity we discuss the scalar diagonal average $\kappa_{latt} = \frac{1}{3}\text{Tr}[\kappa_{latt}]$. The calculations are an excellent match to measurements on single crystals with modest doping levels,[10,11] and the predicted 9.98 and 4.91 W m$^{-1}$ K$^{-1}$ at $T = 300$ and 600 K, respectively, agree quantitatively with the experimental measurements of 10 W m$^{-1}$ K$^{-1}$ and 5-5.5 W m$^{-1}$ K$^{-1}$ in Ref. [11]. The calculations and measurements diverge beyond 600 K due to a plateau in the measured $\kappa_{latt}$, which may be due to the neglect of higher-order anharmonic effects and/or thermal expansion in the RTA, or to other thermal effects such as the onset of oxidation or decomposition.[58]
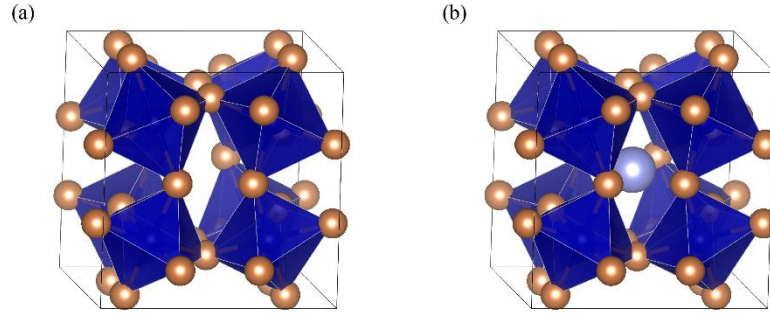
**Figure 1** (a) Conventional unit cell of $CoSb_3$ comprising a network of corner-sharing $CoSb_6$ octahedra (dark blue/brown) surrounding cavities centred at (0, 0, 0) and (0.5, 0.5, 0.5). (b) Representative $XCo_8Sb_{24}$ filled model with the filler atom X in the central cavity (pale blue). These images were prepared using the VESTA software.[55]
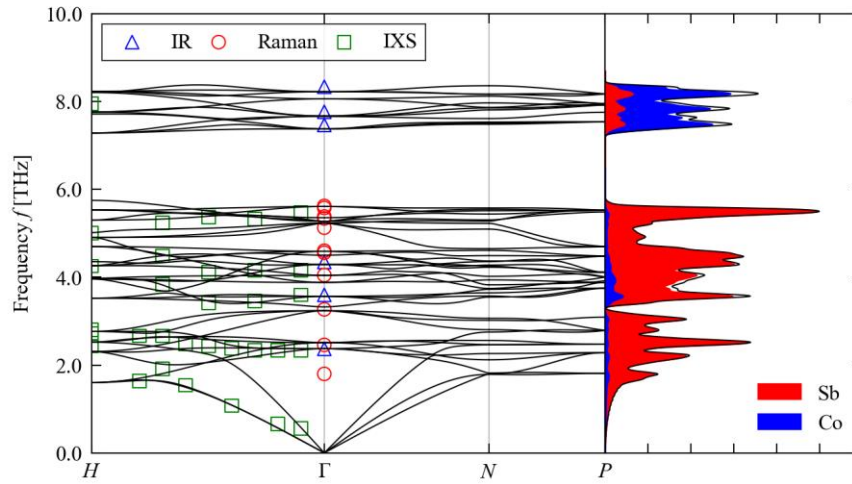


**Figure 2** Calculated phonon dispersion and density of states $g(f)$ of $CoSb_3$. The projections of the $g(f)$ onto the Co and Sb atoms is shown by the blue and red shaded curves respectively. Experimental measurements of the $\Gamma$-point phonon frequencies from infrared (IR)[52] and Raman spectroscopy[56,57] and measurements of the frequencies along the $\Gamma \rightarrow H$ segment of the phonon dispersion from inelastic X-ray scattering (IXS)[54] are overlaid for comparison.

**Figure 3** Calculated temperature dependence of the lattice thermal conductivity $\kappa_{\text{latt}}$ of CoSb$_3$. The experimental measurements from Refs. [10] and [11] are overlaid for comparison.

Within the RTA $\kappa_{\text{latt}}$ is computed as a sum over phonon modes $\lambda$ according to:

$$\boldsymbol{\kappa}_{\text{latt}} = \frac{1}{N} \sum_\lambda \boldsymbol{\kappa}_\lambda = \frac{1}{NV_0} \sum_\lambda C_\lambda \boldsymbol{v}_\lambda \otimes \boldsymbol{v}_\lambda \tau_\lambda \tag{2}$$

where $C_\lambda$ is the modal volumetric heat capacity, $\boldsymbol{v}_\lambda \otimes \boldsymbol{v}_\lambda$ is the outer product of the group velocity $\boldsymbol{v}_\lambda$, $\tau_\lambda$ is the lifetime, $N$ is the number of phonon wavevectors $\mathbf{q}$ included in the summation, and $V_0$ is the volume of the unit cell. The product $\boldsymbol{v}_\lambda \tau_\lambda$ is the phonon mean-free path $\boldsymbol{\Lambda}_\lambda$ (MFP), which appears in an alternative form of Eq. 2. The $C_\lambda$ and $\boldsymbol{v}_\lambda = \partial\omega_\lambda/\partial\mathbf{q}_\lambda$ ($\omega_\lambda = 2\pi f_\lambda$) are calculated within the harmonic approximation, while the $\tau_\lambda$ are calculated based on a perturbative model for the phonon-phonon interactions. A detailed overview of this method is given in Ref. [49] and in the following section.

Accumulating the $\kappa_\lambda$ as a function of frequency and comparing the result to the phonon DoS shows how modes in different frequency ranges contribute to the overall $\kappa_{\text{latt}}$ (Fig. 4). At 300 K, modes up to 2.5 THz contribute ~ 80 % to the $\kappa_{\text{latt}}$, and the remaining 20 % is accumulated up to ~6 THz. The majority of the thermal transport is therefore through the acoustic modes and the remainder is through the lower-frequency Sb-based optic modes (c.f. Fig. 2). The contribution of the high-frequency Co-based modes is negligible. Analysis of the $\kappa_{\text{latt}}$ at 600 K yields similar conclusions but with a marked reduction in the $\kappa_\lambda$ across the frequency spectrum.
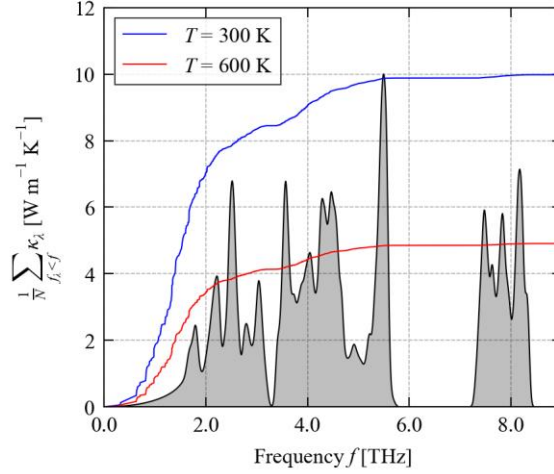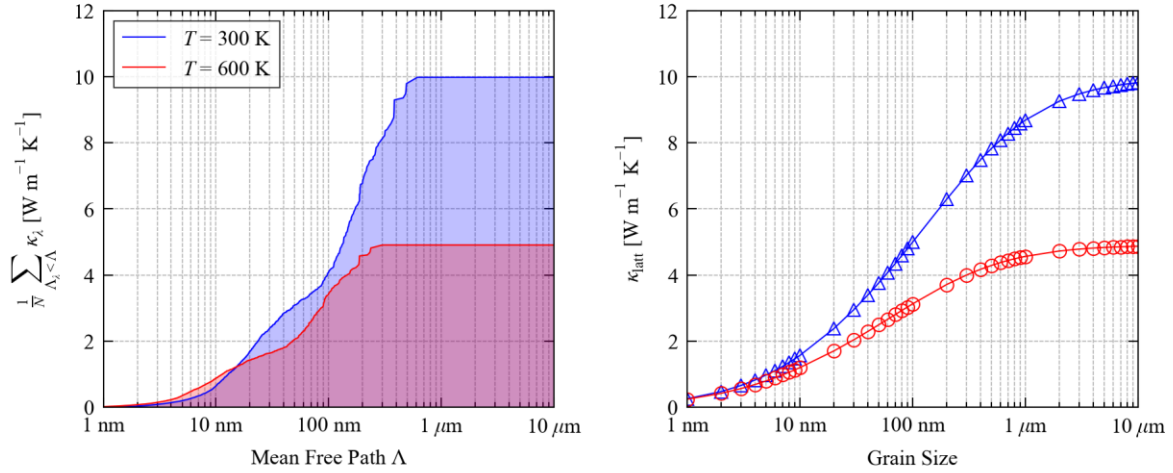
**Figure 4** Accumulation of the modal thermal conductivity $\kappa_\lambda$ of CoSb$_3$ as a function of frequency at $T = 300$ (blue) and $600$ K (red). The phonon density of states $g(v)$ is overlaid as a filled black/grey curve for comparison.

Further insight into the nature of the $\kappa_{\text{latt}}$ can be obtained from the frequency spectra of the modal terms in Eq. 2 and the mean-free paths $\Lambda_\lambda$ (Fig. 5). We consider the group velocity/mean free path norms $|\boldsymbol{v}_\lambda|/|\boldsymbol{\Lambda}_\lambda|$ and the diagonal averages of the $\boldsymbol{\kappa}_\lambda$ and $\boldsymbol{v}_\lambda \otimes \boldsymbol{v}_\lambda$ tensors, i.e. $\frac{1}{3}\text{Tr}[\boldsymbol{\kappa}_\lambda]$ and $\frac{1}{3}\text{Tr}[\boldsymbol{v}_\lambda \otimes \boldsymbol{v}_\lambda]$, which we denote $v_\lambda$, $\Lambda_\lambda$, $\kappa_\lambda$, and $v_\lambda^2$. The $\kappa_\lambda$ range from $10^{-5}$ to $1$ W m$^{-1}$ K$^{-1}$ and are a maximum for the low-frequency acoustic modes as expected. The $C_\lambda$ are a shallow function of frequency and vary by ~30 % from $7.4$-$9.6 \times 10^{-5}$ eV over the 9 THz range of the phonon spectrum. The $v_\lambda$ and $v_\lambda^2$ span 3 and 6 orders of magnitude, respectively, and the group velocities reach up to ~5,000 ms$^{-1}$. At 300 K the $\tau_\lambda$ range from ~200 ps at low frequencies to < 10 ps for the high-frequency Co-based optic modes. The large $\kappa_\lambda$ of the acoustic modes thus arises from their high $v_\lambda$ and long $\tau_\lambda$, while the negligible contribution of the high-frequency optic modes is due to their low $v_\lambda$ and a short $\tau_\lambda$. The $\Lambda_\lambda$ approach microns for the acoustic modes but reduce steadily with frequency so that the MFPs of the high-frequency optic modes are on the order of nm. The lifetimes are substantially lowered at 600 K with a corresponding reduction in the MFPs (see Figure S2.1).
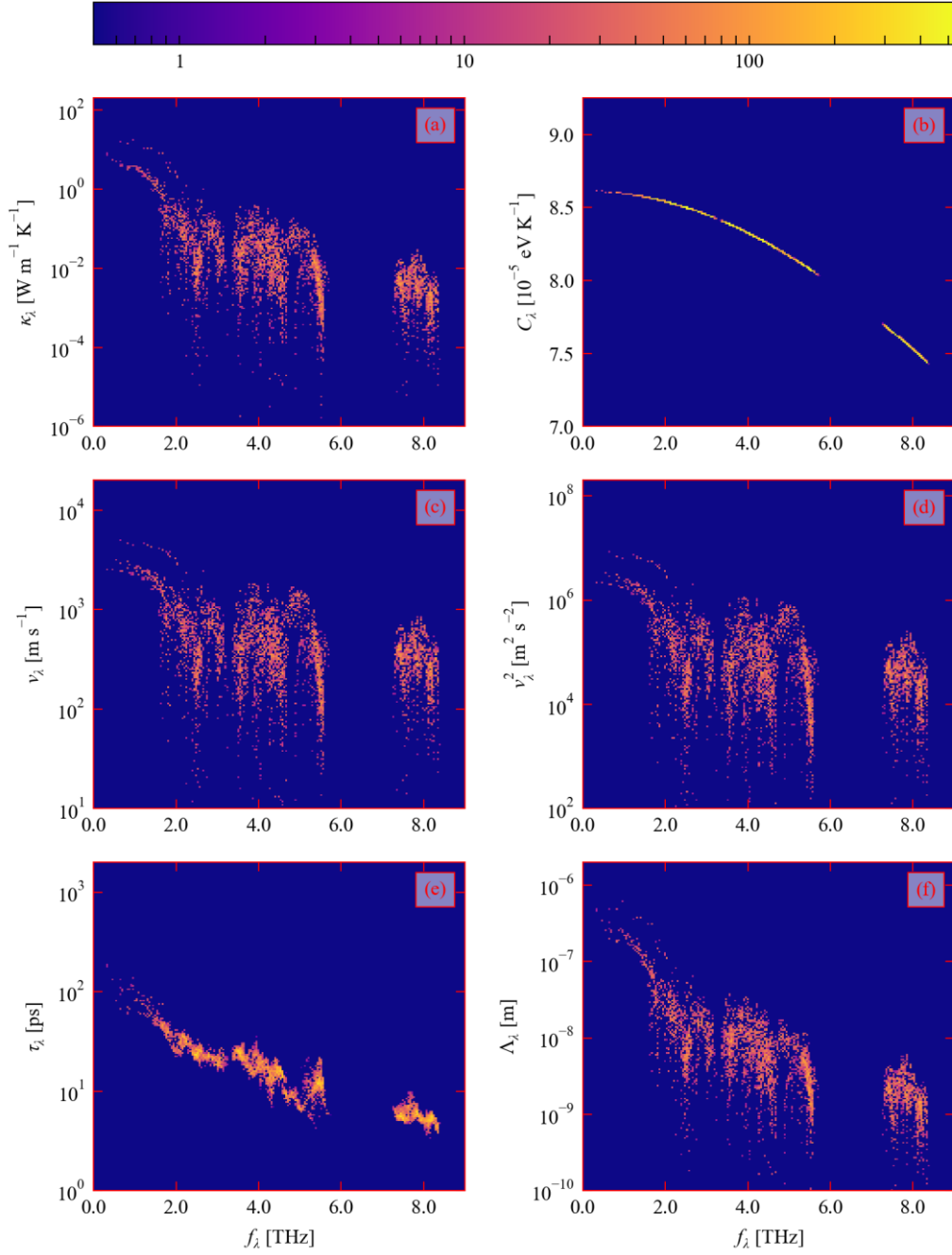
**Figure 5** Frequency spectra of the modal terms in Eq. 2 at $T = 300$ K, *viz.* the thermal conductivities $\kappa_\lambda$ (a), heat capacities $C_\lambda$ (b), group velocities $v_\lambda$ (c) and outer products $v_\lambda^2$ (d), and the lifetimes $\tau_\lambda$ (e), together with the mean-free paths $\Lambda_\lambda = v_\lambda \tau_\lambda$ (f). Note that quantities in (a) and (c)-(f) are shown on a logarithmic scale, while the $C_\lambda$ in (b) are shown on a linear scale.

**Figure 6** (a) Accumulation of the thermal conductivity $\kappa_{latt}$ of CoSb$_3$ as a function of the phonon mean-free path $\Lambda_\lambda = v_\lambda \tau_\lambda$ at $T = 300$ and $600$ K (blue/red). (b) Estimated dependence of the $\kappa_{latt}$ at 300 and 600 K on the crystal grain size obtained using a boundary-scattering model.

It is also of interest to analyse how the $\kappa_\lambda$ accumulate as a function of the phonon MFP (Fig. 6a). At 300 K, around 10 % of the $\kappa_{latt}$ is through modes with $\Lambda_\lambda < 10$ nm, a further 30 % is through modes with $\Lambda_\lambda < 100$ nm, and 60 % is through modes with MFPs up to 1 $\mu$m. At 600 K the MFPs are suppressed due to the reduced lifetimes and modes with $\Lambda_\lambda$ from 10-100 nm account for ~70 % of the $\kappa_{latt}$. The effect of limiting the transport through modes with long MFPs can be investigated by using a boundary-scattering model to mimic a finite grain size (Fig. 6b), and this analysis indicates that nanostructuring can potentially yield a substantial reduction in the $\kappa_{latt}$, in keeping with its widespread use as a strategy for optimising thermoelectric performance.[2]

This analysis also highlights the sensitivity of experimental measurements to sample preparation methods. While our calculated bulk $\kappa_{latt}$ agree very well with experimental measurements on single crystals, they are 25-30 % higher than measurements on annealed powders.[12] According to the calculations in Fig. 6b, this reduction could be obtained with a grain size of ~200 nm, which is not unreasonable given that the samples in Ref. [12] were calculated to be 89 % of the theoretical density with an Sb/Co ratio of 2.65.

*b. CoSb₃ with noble gas fillers*

The lattice constants of the five filled models, *viz.* HeCo$_8$Sb$_{24}$, NeCo$_8$Sb$_{24}$, ArCo$_8$Sb$_{24}$, KrCo$_8$Sb$_{24}$ and XeCo$_8$Sb$_{24}$, are listed in Table 1. Filling with Ne-Xe results in a small expansion of the unit cell, increasing in proportion with the atomic radii of the fillers, and the maximum 0.64 % expansion with Xe suggests the cavity is large enough to accommodate all five atoms. Geometry optimisations including the DFT-D3 dispersion correction produced lattice constants around 0.75 % smaller with the same overall trend, suggesting that a dispersion correction is not required for these systems (Table S2.1).

| | $a_0$ [Å] | $\Delta a_0$ [%] | $r_X$ [pm] |
|---|---|---|---|
| $CoSb_3$ | 8.952 | - | - |
| $HeCo_8Sb_{24}$ | 8.952 | 0.00 | 31 |
| $NeCo_8Sb_{24}$ | 8.960 | 0.09 | 38 |
| $ArCo_8Sb_{24}$ | 8.975 | 0.26 | 71 |
| $KrCo_8Sb_{24}$ | 8.987 | 0.39 | 88 |
| $XeCo_8Sb_{24}$ | 9.010 | 0.64 | 108 |

**Table 1** Optimised lattice constants of $CoSb_3$ and $XCo_8Sb_{24}$ with X = He, Ne, Ar, Kr and Xe. The second column gives the % difference in the lattice constants of the filled models to pristine $CoSb_3$, and the third column lists the atomic radii $r_X$ of the filler atoms for comparison.

The unfolded phonon dispersions and DoS curves of the filled models are shown in Fig. 7. In the "rattler" model of filled cage compounds, the fillers introduce localised bands of modes with a narrow dispersion.[59] However, theoretical studies on $BaFe_4Sb_{12}$ have shown that some fillers introduce features into the DoS over a wide range of frequencies.[36] Filling with He introduces a narrow peak into the phonon DoS at ~6 THz, which lies in the phonon bandgap and is suggestive of "rattling" behaviour (this peak has a small spectral weight un the unfolded phonon dispersion and is therefore difficult to discern). The other four fillers introduce broader bands of modes among the lower-frequency optic modes, similar to the Ba filler in $BaFe_4Sb_{12}$.[36] Interestingly, modes associated with Ne appear around 4 THz in $NeCo_8Sb_{24}$, 4-6 THz $ArCo_8Sb_{24}$, and ~3.5-4 THz in the Kr- and Xe-filled systems. None of the curves show any evidence of imaginary modes, suggesting that there are no driving forces for the fillers to move off centre.

The frequencies at a wavevector **q** are the eigenvalues obtained by constructing and diagonalising the dynamical matrix $D(\mathbf{q})$ built from $3 \times 3$ blocks according to:

$$D_{\alpha\beta}(jj', \mathbf{q}) = \frac{1}{\sqrt{m_j m_{j'}}} \sum_{l'} \Phi_{\alpha\beta}(j0, j'l') \times \exp\{i\mathbf{q} \cdot [\mathbf{r}(j'l') - \mathbf{r}(j0)]\} \tag{3}$$

where the indices $j$ and $j'$ denote atoms with masses $m_j$ located at $\mathbf{r}(jl)$ in the $l$th unit cell, and $\mathbf{\Phi}(j0, j'l')$ are the second-order force-constant matrices:

$$\Phi_{\alpha\beta}(j0, j'l') = \frac{\partial^2 E}{\partial r_\alpha(j0) \partial r_\beta(j'l')} = -\frac{\partial F_\beta(j'l')}{\partial r_\alpha(j0)} \tag{4}$$

If the filler atoms are modelled as moving within a rigid $CoSb_3$ cage, an approximate rattling frequency $\tilde{f}_X$ can be determined by diagonalising a $3 \times 3$ dynamical matrix at $\mathbf{q} = \Gamma$ built from the "self" force constants of the filler atom, i.e. with $j = j' = X$. For the cubic crystal this yields a single unique eigenvalue. Table 2 lists for each filler atom the $\tilde{f}_X$ determined from this analysis together with the atomic masses $m_X$ and the Frobenius norms of the $\mathbf{\Phi}(X0, X0)$ force constants, calculated as:
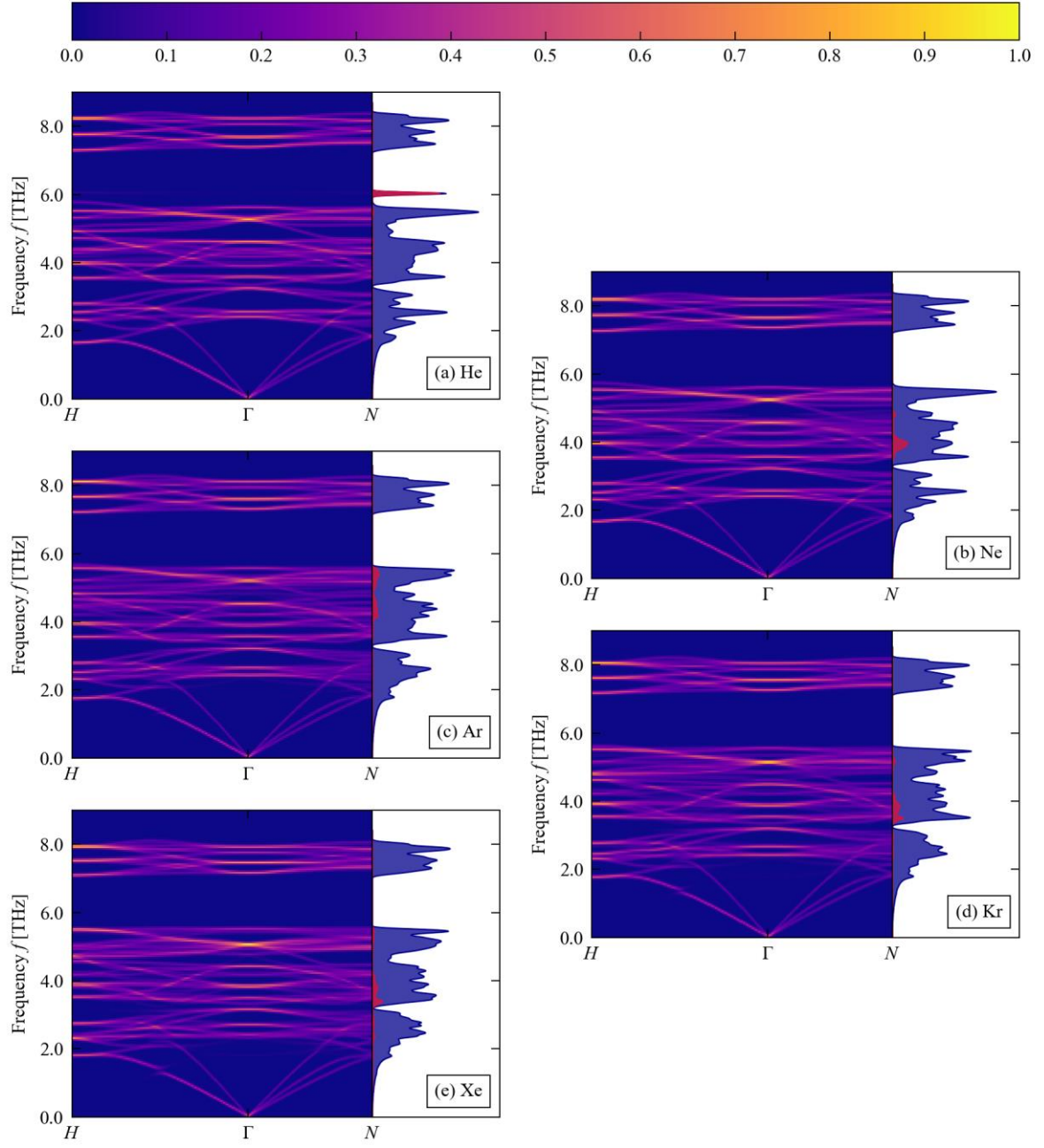
**Figure 7** Unfolded phonon band dispersions and density of states $g(f)$ (DoS) of $XCo_8Sb_{24}$ with X = He (a), Ne (b), Ar (c), Kr (d) and Xe (e). The colour scale shows the spectral weights obtained from the band-unfolding procedure. In each of the DoS plots the total $g(f)$ is shown in dark blue with the projection onto the filler atom X overlaid in red.

| | $m_X$ [amu] | $\|\Phi(X0, X0)\|$ [eV Å$^{-2}$] | $\tilde{f}_X$ [THz] |
|---|---|---|---|
| HeCo$_8$Sb$_{24}$ | 4.0026 | 1.005 | 5.960 |
| NeCo$_8$Sb$_{24}$ | 20.180 | 2.316 | 4.022 |
| ArCo$_8$Sb$_{24}$ | 39.948 | 6.410 | 4.745 |
| KrCo$_8$Sb$_{24}$ | 83.798 | 8.643 | 3.798 |
| XeCo$_8$Sb$_{24}$ | 131.29 | 12.35 | 3.613 |

**Table 2** Atomic masses $m_X$, force-constant norms $\|\Phi(X0, X0)\|$ and approximate rattling frequencies $\tilde{f}_X$ of the filler atoms X in the five XCo$_8$Sb$_{24}$ models. The force-constant norms and $\tilde{f}_X$ are calculated using Eqs. 3-5.

$$\|\Phi(j0, j'l')\| = \sum_\alpha \sum_\beta \left| \Phi_{\alpha\beta}(j0, j'l') \right|^2 \tag{5}$$

This simple model predicts the centre of the filler peaks in Fig. 7 remarkably well. On going from He to Xe, the $\|\Phi(X0, X0)\|$ increase by an order of magnitude from 1.01 to 12.4 eV Å$^{-2}$, indicating that the larger filler atoms experience stronger restoring forces from the framework atoms. As per Eq. 5, a larger $m_X$ and $\|\Phi\|$ will respectively decrease and increase $\tilde{f}_X$. From He to Ne, the $\|\Phi\|$ increases by a factor of two but the mass increases fivefold, resulting in a ~30 % reduction in $\tilde{f}_X$. On the other hand, from Ne to Ar the $\|\Phi\|$ increases by ~3× while the mass doubles, producing an overall increase in $\tilde{f}_X$. From Ar to Kr and Xe, the mass increases faster than the $\|\Phi\|$ and the rattling frequency falls from 4.75 to 3.80 and 3.61 THz.

Comparison of the unfolded phonon dispersions to the dispersion of CoSb$_3$ (c.f. Figs. 2 and 7; see also Figs. S2.2-S2.6) shows the heavier filler atoms have a progressively larger effect on the vibrations of the host framework. In HeCo$_8$Sb$_{24}$, the spectrum is largely unchanged save for the localised branch in the phonon bandgap. From NeCo$_8$Sb$_{24}$ to XeCo$_8$Sb$_{24}$ the frequencies of the acoustic and low-lying optic modes up to ~2.5 THz are raised, with the largest increases towards the *H* wavevector, while the frequencies of the higher-energy optic modes are reduced. The reduction in bandwidth ("depression") of the phonon spectrum would lead to a reduction in the mode group velocities, one of the two main mechanisms by which fillers can suppress the thermal conductivity of cage compounds.[59] This mechanism is most usually observed when the rattling frequency falls among the acoustic modes and introduces avoided crossings into the phonon dispersion.[38,60,61] In these systems, however, the noble gas fillers have higher rattling frequencies and would therefore mainly affect the optic modes, and the density of phonon branches makes it difficult to clearly identify any avoided crossings.

When placed in the centre of the cavity, as shown in Fig. 1b, the first, second and third neighbours of the filler atoms are 12 Sb atoms, 8 Co atoms, and a further 24 Sb atoms respectively. The corresponding $\|\Phi\|$ increase by an order of magnitude from He to Xe, from $1.78 \times 10^{-1}$, $1.78 \times 10^{-2}$ and $4.66 \times 10^{-3}$ eV Å$^{-2}$ in HeCo$_8$Sb$_{24}$ to 1.63, $2.32 \times 10^{-1}$ and $4.88 \times 10^{-2}$ eV Å$^{-2}$ in XeCo$_8$Sb$_{24}$ (Table S2.2). The stronger interactions between the larger/heavier filler atoms and the host framework explains the increasingly prominent frequency shifts in the unfolded phonon dispersions. The $\|\Phi\|$ for the nearest-neighbour Co-Sb and Sb-Sb interactions in

pristine CoSb$_3$ are 4.40 and 5.02 eV Å$^{-2}$, respectively, so the first-neighbour Kr-Sb and Xe-Sb interactions are of comparable strength to the bonding in the host framework.
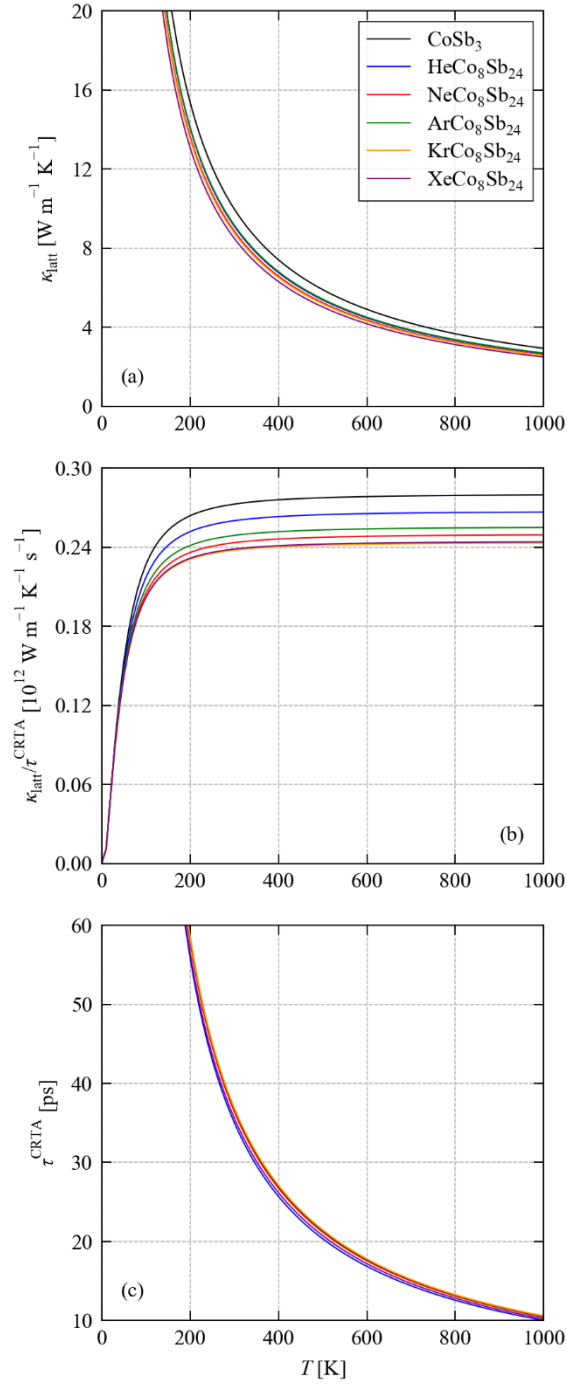
The calculated thermal-conductivity curves for the five filled models (Fig. 8a) show that filling produces a modest reduction in $\kappa_{\text{latt}}$ compared to pristine CoSb$_3$, with a somewhat intricate trend among the five fillers. A comparison of values at 300 and 600 K (Table 3, Table S2.3) show that the $\kappa_{\text{latt}}$ fall in the order of Ar $\approx$ He $>$ Ne $\approx$ Kr $>$ Xe, with reductions of 8-9, 11-12 and 15 % compared to CoSb$_3$. This correlates with the $\tilde{f}_{\text{X}}$: He and Ar have the highest $\tilde{f}_{\text{X}}$ and produce the smallest reduction in $\kappa_{\text{latt}}$, Ne and Kr have similar $\tilde{f}_{\text{X}}$ and produce similar reductions, and Xe has the lowest $\tilde{f}_{\text{X}}$ and has the largest effect on $\kappa_{\text{latt}}$. It is therefore evident that the effect of the fillers on the $\kappa_{\text{latt}}$ depends both on their mass and how strongly they interact with the framework.

The two mechanisms by which filler atoms in cage compounds suppress the heat transport are through resonant scattering, which reduces the lifetimes of framework modes close in frequency to localised "rattling" modes, and by reducing the group velocities.[59] Calculations suggest that these are not mutually exclusive, as the changes to the phonon spectrum that reduce the $v_\lambda$ can introduce new phonon-scattering channels that reduce the $\tau_\lambda$ of modes over a broader spectrum of frequencies.[38] The small differences in the $\kappa_{\text{latt}}$ of the filled models makes it difficult to draw quantitative conclusions by inspecting the spectra of modal properties (Figs. S2.7-S2.11). We therefore developed an analysis following the constant relaxation-time approximation (CRTA) approach commonly used in electronic-structure modelling and computed a quantity $\kappa_{\text{latt}}/\tau^{\text{CRTA}}$ defined as:

$$\kappa_{\text{latt}}/\tau^{\text{CRTA}} \approx \frac{1}{NV_0}\sum_\lambda \frac{\kappa_\lambda}{\tau_\lambda} \approx \frac{1}{NV_0}\sum_\lambda C_\lambda v_\lambda \otimes v_\lambda \tag{6}$$

where $\tau^{\text{CRTA}}$ is an effective phonon lifetime (relaxation time) and the other terms are defined as in Eq. 2. Both $\kappa_{\text{latt}}/\tau^{\text{CRTA}}$ and $\tau^{\text{CRTA}}$ are temperature dependent due to the temperature dependence of the $C_\lambda$ and $\tau_\lambda$. For cubic systems the diagonal elements of $\kappa_{\text{latt}}$ are equal and the off-diagonal elements are negligible, so it is possible to choose a single $\tau^{\text{CRTA}}$ at each temperature such that the separation in Eq. 6 is exact. We discuss the scalar averages $\kappa_{\text{latt}}$ and $\kappa_{\text{latt}}/\tau^{\text{CRTA}}$ in the following.

Fig. 8 compares the $\kappa_{\text{latt}}$, $\kappa_{\text{latt}}/\tau^{\text{CRTA}}$ and $\tau^{\text{CRTA}}$ of pristine CoSb$_3$ and the five XCo$_8$Sb$_{24}$ filled models as a function of temperature. Values at 300 and 600 K listed in Tables 3 and S2.3. The $\kappa_{\text{latt}}/\tau^{\text{CRTA}}$ of the filled models are reduced by 4.6 - 13 % compared to pristine CoSb$_3$ and fall in a similar order to the rattling frequencies with HeCo$_8$Sb$_{24}$ $>$ ArCo$_8$Sb$_{24}$ $>$ NeCo$_8$Sb$_{24}$ $>$ KrCo$_8$Sb$_{24}$ $\approx$ XeCo$_8$Sb$_{24}$. In the RTA model, these reductions are purely due to changes in the harmonic frequency spectrum. On the other hand, the $\tau^{\text{CRTA}}$ in HeCo$_8$Sb$_{24}$ are reduced by ~5 % compared to pristine CoSb$_3$, whereas filling with Ne, Ar and Kr changes the lifetimes by at most 1 % and in some cases increases them, and filling with Xe decreases the $\tau^{\text{CRTA}}$ by a smaller 2.5-3 %. These changes in lifetimes may arise both from changes in the frequency spectrum and in the strength of the anharmonic interactions between modes, which we return to later in the discussion.

**Figure 8** Analysis of the thermal conductivity of $CoSb_3$ and $XCo_8Sb_{24}$ (X = He, Ne, Ar, Kr, Xe) using the constant relaxation-time approximation (CRTA) as defined in Eq. 6. The three subplots show the thermal conductivity $\kappa_{latt}$ (a), the $\kappa_{latt}/\tau^{CRTA}$ (b) and the calculated $\tau^{CRTA}$ (c) as a function of temperature.

| | $\bar{\kappa}_{\text{latt}}$ [W m$^{-1}$ K$^{-1}$] | $\Delta$ [%] | $\bar{\kappa}_{\text{latt}}/\tau^{\text{CRTA}}$ [10$^{12}$ W m$^{-1}$ K$^{-1}$ s$^{-1}$] | $\Delta$ [%] | $\tau^{\text{CRTA}}$ [ps] | $\Delta$ [%] | $\tilde{P}$ [10$^{-12}$ eV$^2$] | $\Delta$ [%] | $\bar{\tau}_\lambda$ [ps] | $\bar{P}_\lambda$ [10$^{-12}$ eV$^2$] |
|---|---|---|---|---|---|---|---|---|---|---|
| CoSb$_3$ | 9.98 | - | 0.273 | - | 36.6 | - | 0.394 | - | 16.97 | 6.00 |
| HeCo$_8$Sb$_{24}$ | 9.11 | -8.71 | 0.260 | -4.62 | 35.0 | -4.30 | 0.399 | 1.35 | 16.46 | 5.65 |
| NeCo$_8$Sb$_{24}$ | 8.86 | -11.20 | 0.243 | -10.73 | 36.4 | -0.52 | 0.388 | -1.35 | 16.62 | 5.46 |
| ArCo$_8$Sb$_{24}$ | 9.17 | -8.12 | 0.249 | -8.71 | 36.8 | 0.65 | 0.391 | -0.71 | 16.30 | 5.35 |
| KrCo$_8$Sb$_{24}$ | 8.77 | -12.15 | 0.238 | -12.84 | 36.9 | 0.79 | 0.387 | -1.65 | 16.38 | 5.27 |
| XeCo$_8$Sb$_{24}$ | 8.49 | -14.90 | 0.239 | -12.52 | 35.6 | -2.72 | 0.386 | -2.03 | 15.79 | 5.18 |

**Table 3** Calculated lattice thermal conductivity $\kappa_{\text{latt}}$, $\kappa_{\text{latt}}/\tau^{\text{CRTA}}$, $\tau^{\text{CRTA}}$ and $\tilde{P}$ at $T$ = 300 K for the CoSb$_3$ and XCo$_8$Sb$_{24}$ (X = He, Ne, Ar, Kr, Xe) models examined in this work. The quantities $\kappa_{\text{latt}}/\tau^{\text{CRTA}}$ and $\tau^{\text{CRTA}}$ are defined in Eq. 6, and the $\tilde{P}$ are defined in the text. The % change in the parameters relative to pristine CoSb$_3$ are shown for comparison. The rightmost two columns list the averaged lifetimes and interaction strengths $\bar{\tau}_\lambda/\bar{P}_\lambda$ for comparison to the $\tau^{\text{CRTA}}$ and $\tilde{P}$ respectively.
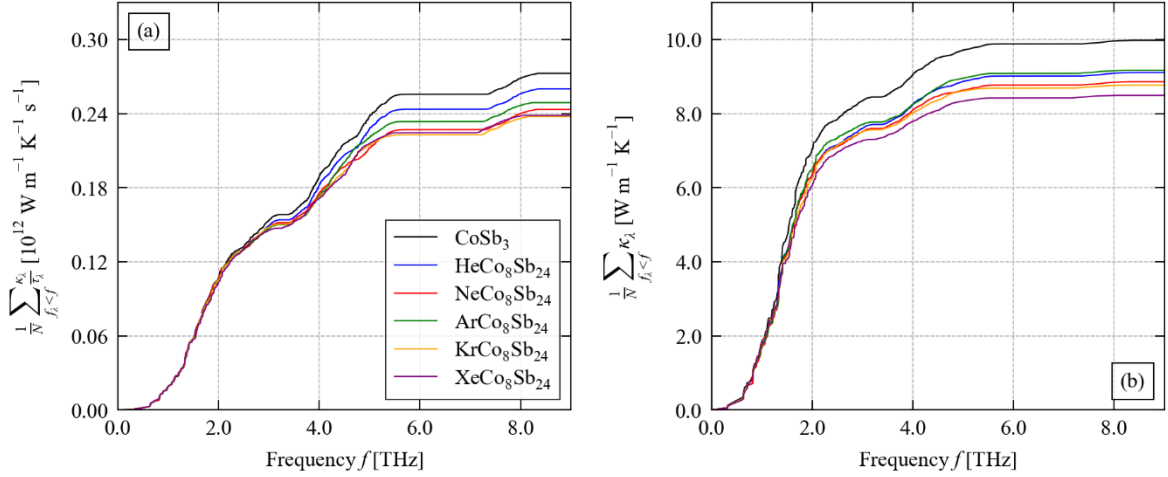
**Figure 9** Accumulation of the $\kappa_\lambda/\tau_\lambda$ (a) and $\kappa_\lambda$ (b) as a function of frequency at $T = 300$ K for pristine CoSb$_3$ and filled XCo$_8$Sb$_{24}$ models with X = He, Ne, Ar, Kr and Xe.

The differing impacts on the $\kappa_{latt}/\tau^{CRTA}$ and $\tau^{CRTA}$ combine to produce the trend in $\kappa_{latt}$ discussed above. In HeCo$_8$Sb$_{24}$, the ~4-5 % reduction in both parameters combine to reduce the $\kappa_{latt}$ by 8-9 % compared to pristine CoSb$_3$. In ArCo$_8$Sb$_{24}$, the $\kappa_{latt}/\tau^{CRTA}$ are reduced by a larger 8-9 % but the $\tau^{CRTA}$ are mostly unchanged, resulting in a $\kappa_{latt}$ higher than HeCo$_8$Sb$_{24}$ but lower than pristine CoSb$_3$. Filling with Ne and Kr reduces the $\kappa_{latt}/\tau^{CRTA}$ by ~11-12 % while changing the $\tau^{CRTA}$ by 0.5-1 %, producing a similar overall $\kappa_{latt}$. In XeCo$_8$Sb$_{24}$, the $\kappa_{latt}/\tau^{CRTA}$ and $\tau^{CRTA}$ are reduced by ~12.5 and 2.5 %, respectively, which produces the smallest $\kappa_{latt}$ of the five filled materials.

As for $\kappa_\lambda$, the $\kappa_\lambda/\tau_\lambda$ in the summand in Eq. 6 can be accumulated as a function of frequency (Fig. 9, Fig. S2.12). This shows that the largest change in the $\kappa_{latt}/\tau^{CRTA}$ on filling occurs in the optic modes between ~2.5-6 THz. Comparing accumulations of $\kappa_\lambda/\tau_\lambda$ and $\kappa_\lambda$, as in Fig. 4, shows a small reduction in heat transport through the acoustic modes between 1-2.5 THz and a larger reduction in transport through the optic modes, which is also reflected in the $\kappa_{latt}/\tau^{CRTA}$. Taking these analyses together, we conclude that the five fillers primarily suppress the heat transport in CoSb$_3$ by reducing the group velocity and lifetimes of the optic modes. Since the affected modes only account for ~20 % of the $\kappa_{latt}$, this explains why even the heaviest Xe filler produces only a 15 % reduction.

Since the CRTA method is not usually used for $\kappa_{latt}$ calculations, it is interesting to see how the $\tau^{CRTA}$ compare to the actual $\tau_\lambda$. In these calculations, the $\tau^{CRTA}$ at 300 and 600 K are around twice the average mode lifetime $\bar{\tau}_\lambda$ (Table 3, Table S2.3), which is not surprising given the order of magnitude variation in $\tau_\lambda$ with frequency in Fig. 5. The $\tau^{CRTA}$ do reflect the average order of magnitude of the $\tau_\lambda$, and might therefore serve as a useful metric to compare between systems.

To investigate the small effects of filling on the phonon lifetimes, we follow the analysis outlined in Ref. [49]. In the RTA, the $\tau_\lambda$ are calculated as the inverse of the phonon linewidths $\Gamma_\lambda$:

$$\tau_\lambda = \frac{1}{2\Gamma_\lambda} \tag{7}$$

$\Gamma_\lambda$ are calculated from the imaginary part of the phonon self energy by summing over interactions between triplets of modes $\lambda$, $\lambda'$ and $\lambda''$:

$$
\begin{aligned}
\Gamma_\lambda = \frac{18\pi}{\hbar^2} \sum_{\lambda'\lambda''} &|\Phi_{-\lambda\lambda'\lambda''}|^2 \\
&\times \{(n_{\lambda'} + n_{\lambda''} + 1)\delta(\omega_\lambda - \omega_{\lambda'} - \omega_{\lambda''}) \\
&+ (n_{\lambda'} - n_{\lambda''})[\delta(\omega_\lambda + \omega_{\lambda'} - \omega_{\lambda''}) - \delta(\omega_\lambda - \omega_{\lambda'} + \omega_{\lambda''})]\}
\end{aligned}
\tag{8}
$$

where $\Phi_{-\lambda\lambda'\lambda''}$ are the three-phonon interaction strengths, $\omega_\lambda$ are the angular frequencies, and $n_\lambda$ are the phonon occupation numbers from the Bose-Einstein distribution:

$$n_\lambda = \frac{1}{\exp(\hbar\omega_\lambda/k_\text{B}T) - 1} \tag{9}$$

The $\Phi_{\lambda\lambda'\lambda''}$ are calculated from the expression:

$$
\begin{aligned}
\Phi_{\lambda\lambda'\lambda''} = \frac{1}{\sqrt{N}}\frac{1}{3!} &\sum_{jj'j''}\sum_{\alpha\beta\gamma} W_{\lambda,\alpha}(j)W_{\lambda',\beta}(j')W_{\lambda'',\gamma}(j'')\sqrt{\frac{\hbar}{2m_j\omega_\lambda}}\sqrt{\frac{\hbar}{2m_{j'}\omega_{\lambda'}}}\sqrt{\frac{\hbar}{2m_{j''}\omega_{\lambda''}}} \\
&\times \sum_{l'l''}\Phi_{\alpha\beta\gamma}(j0,j'l',j''l'') \times \exp\{i\mathbf{q}_{\lambda'}\cdot[\boldsymbol{r}(j'l') - \boldsymbol{r}(j0)]\} \\
&\times \exp\{i\mathbf{q}_{\lambda''}\cdot[\boldsymbol{r}(j''l'') - \boldsymbol{r}(j0)]\} \times \exp\{i(\mathbf{q}_\lambda + \mathbf{q}_{\lambda'} + \mathbf{q}_{\lambda''})\cdot\boldsymbol{r}(j0)\} \\
&\times \Delta(\mathbf{q}_\lambda + \mathbf{q}_{\lambda'} + \mathbf{q}_{\lambda''})
\end{aligned}
\tag{10}
$$

where $W_\lambda$ are the phonon mode eigenvectors (displacement patterns), the indices $j$, $j'$ and $j''$ denote atoms with masses $m_j$ located at $\boldsymbol{r}(jl)$ in the $l$th unit cell, and $\boldsymbol{\Phi}(j0,j'l',j''l'')$ are the third-order force-constant matrices:

$$\Phi_{\alpha\beta\gamma}(j0,j'l',j''l'') = \frac{\partial^3 E}{\partial r_\alpha(j0)\partial r_\beta(j'l')\partial r_\gamma(j''l'')} \tag{11}$$

The functions $\delta$ and $\Delta$ in Eqs. 8 and 10 enforce conservation of energy and crystal momentum, respectively.

Eq. 8 encompasses two types of scattering processes, *viz.* collisions, where $\lambda + \lambda' \to \lambda''$ or $\lambda + \lambda'' \to \lambda'$, and decays, where $\lambda \to \lambda' + \lambda''$. These are sometimes referred to in the literature as absorption and emission processes. Broad linewidths $\Gamma_\lambda$, i.e. short $\tau_\lambda$, arise from strong $\Phi_{\lambda\lambda'\lambda''}$ and/or a high density of energy-conserving collision and decay pathways. Both factors can lead to short mode lifetimes - for example, the

picosecond lifetimes in the hybrid perovskite $(CH_3NH_3)PbI_3$ have been attributed to strong $\Phi_{\lambda\lambda'\lambda''}$,[31,32] whereas the low predicted $\kappa_{latt}$ in $Bi_2Sn_2O_7$ has been ascribed to a high density of scattering channels.[35] Another subtlety of note is that the phonon frequencies $\omega_\lambda$ and phonon-phonon interaction strengths $\Phi_{-\lambda\lambda'\lambda''}$ are temperature independent in the RTA model, and thus the strong temperature dependence of the $\tau_\lambda$ and $\tau^{CRTA}$ in Figs. 5 and 8 is due entirely to the changes in the $n_\lambda$.

The $\Phi_{-\lambda\lambda'\lambda''}$ can be averaged over the $(3n_a)^2$ pairs of interacting modes to obtain a phonon-phonon interaction strength $P_\lambda$ for each mode:

$$P_\lambda = \frac{1}{(3n_a)^2} \sum_{\lambda'\lambda''} |\Phi_{-\lambda\lambda'\lambda''}|^2 \tag{12}$$

An approximate linewidth $\tilde{\Gamma}_\lambda$ can then be defined as the product of the $P_\lambda$ and a weighted two-phonon joint density of states (w-JDoS) function $N_2(\mathbf{q}, \omega)$ counting the number of energy- and momentum-conserving scattering channels based on the phonon frequency spectrum:

$$\tilde{\Gamma}_\lambda = \frac{18\pi}{\hbar^2} P_\lambda N_2(\mathbf{q}_\lambda, \omega_\lambda) \tag{13}$$

The $N_2(\mathbf{q}, \omega)$ are defined as follows and are the sum of separate w-JDoS functions for collision and decay processes, which we denote Class 1 and Class 2, respectively, following Ref. [49]:

$$N_2(\mathbf{q}, \omega) = N_2^{(1)}(\mathbf{q}, \omega) + N_2^{(2)}(\mathbf{q}, \omega) \tag{14}$$

$$\begin{aligned} N_2^{(1)}(\mathbf{q}, \omega) = \frac{1}{N} \sum_{\lambda'\lambda''} &\Delta(-\mathbf{q} + \mathbf{q}_{\lambda'} + \mathbf{q}_{\lambda''}) \\ &\times (n_{\lambda'} - n_{\lambda''})[\delta(\omega + \omega_{\lambda'} - \omega_{\lambda''}) - \delta(\omega - \omega_{\lambda'} + \omega_{\lambda''})] \end{aligned} \tag{15}$$

$$N_2^{(2)}(\mathbf{q}, \omega) = \frac{1}{N} \sum_{\lambda'\lambda''} \Delta(-\mathbf{q} + \mathbf{q}_{\lambda'} + \mathbf{q}_{\lambda''}) \times (n_{\lambda'} + n_{\lambda''} + 1)\delta(\omega - \omega_{\lambda'} - \omega_{\lambda''}) \tag{16}$$

In a similar manner to how the CRTA analysis allows the impact of the fillers on the group velocities and lifetimes to be quantified, finding a constant value $\tilde{P}$ such that setting the $P_\lambda$ in Eq. 13 to $P_\lambda = \tilde{P}$ recovers the $\kappa_{latt}$ provides a means to quantify the impact of changes to the interaction strengths on the thermal transport.
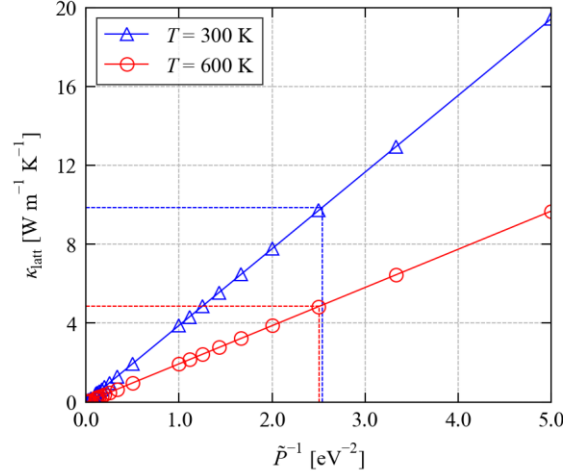
**Figure 10** Dependence of the $\kappa_{\text{latt}}$ of pristine CoSb$_3$ on the averaged three-phonon interaction strength $\tilde{P}$ defined in the text at $T = 300$ and 600 K (blue/red). The dashed lines mark the $\tilde{P}$ that recover the calculated $\kappa_{\text{latt}}$ at the two temperatures.

Based on Eqs. 7 and 13, the $\kappa_{\text{latt}}$ vary inversely with $\tilde{P}$. Fig. 10 plots the $\kappa_{\text{latt}}$ of CoSb$_3$ at 300 and 600 K as a function of $\tilde{P}^{-1}$. The calculated $\kappa_{\text{latt}}$ is recovered for $\tilde{P} = 3.94 \times 10^{-13}$ and $3.99 \times 10^{-13}$ eV$^2$ at the two temperatures, which are both roughly an order of magnitude smaller than the average $P_\lambda$ (Table 3, Table S2.3). The $P_\lambda$ vary by over an order of magnitude with frequency (Figs. S2.13-S2.18), so as for the $\tau^{\text{CRTA}}$ we would expect the $\tilde{P}$ to be weighted towards the modes that make the larger contributions to the $\kappa_{\text{latt}}$.

The $\Phi_{\lambda\lambda'\lambda''}$ in Eq. 10, and, by extension, the $P_\lambda$ and $\tilde{P}$, are formally temperature independent. The $\tilde{P}$ obtained at 300 and 600 K differ by 1.3 %, indicating that it is not strictly possible to replace the $\Phi_{\lambda\lambda'\lambda''}$ with a single value and reproduce the $\kappa_{\text{latt}}$ exactly over a wide range of temperatures. However, the remarkably small difference suggests the $\tilde{P}$ might also be a useful parameter for comparing materials.

Similar analyses to Fig. 10 were performed for the five filled materials (Figs. S2.19-S2.23), and the corresponding $\tilde{P}$ at 300 and 600 K are listed in Table 3 and Table S2.3. Taking into account the prefactor of $1/(3n_a)^2$ in Eq. 12 gives three possible scenarios: (1) if there are no interactions between the filler and framework modes - i.e. the corresponding $\Phi_{\lambda\lambda'\lambda''}$ are zero - the $P_\lambda$ would be scaled by $32^2/33^2 = 0.94$; (2) if the interactions between the filler and framework modes are of comparable strength to those between the framework modes, the $P_\lambda$ would be unchanged; and (2) if the filler and framework modes interact more strongly than the framework modes, the $P_\lambda$ would increase. For HeCo$_{12}$Sb$_{24}$, the $\tilde{P}$ are increased by ~1.3 % compared to pristine CoSb$_3$, indicating a strong interaction between the He and framework modes. For Ne-Xe the values are reduced by 0.5-2 %, indicating that the interactions between the filler and framework modes are not negligible, but are weaker than the interactions among framework modes. This contrast provides a natural explanation for why filling with He leads to a larger reduction in the $\tau^{\text{CRTA}}$ than the other four noble gases. The weaker

interaction strengths for the heavier fillers is also consistent with modelling studies on $YbFe_4Sb_{12}$, which found that the third-order (anharmonic) interactions involving Yb were relatively weak.[38]

We also examined the effect of the filler atoms on the numbers of energy-conserving scattering channels by comparing the $N_2(\mathbf{q}, \omega)$ defined in Eqs. 14-16 averaged over wavevectors $\mathbf{q}$, i.e.:

$$\bar{N}_2(\omega) = \bar{N}_2^{(1)}(\omega) + \bar{N}_2^{(2)}(\omega) = \frac{1}{N}\sum_{\mathbf{q}} N_2^{(1)}(\mathbf{q}, \omega) + \frac{1}{N}\sum_{\mathbf{q}} N_2^{(2)}(\mathbf{q}, \omega) \qquad (17)$$

As shown in Fig. 11a, collisions are the dominant process below 2 THz, while decay channels become available from ~2 THz, and the $\bar{N}_2^{(1)}(\omega)$ and $\bar{N}_2^{(2)}(\omega)$ are comparable around 4 THz. The number of collision pathways falls to zero from ~6-8 THz, and decay processes dominate at higher frequencies. The five filled models show significant changes in the number of collision channels over the 2-6 THz region where the largest reduction in the $\kappa_{latt}$ is observed (c.f. Fig. 9), while $KrCo_8Sb_{24}$ and $XeCo_8Sb_{24}$ also show an increase in the number of decay channels between 4-6 THz. Similar differences are seen at 600 K (see Figure S2.24), but both w-JDoS functions are scaled by a factor of two due to the larger phonon occupation numbers.

Combining these observations with the changes in the $P_\lambda$, we conclude that He reduces the phonon lifetimes by virtue of a relatively strong anharmonic interaction between the filler and framework modes and an increase in the number of collision channels, while the heavier fillers modulate the number of collision and, to a lesser extent, decay channels. These together produce the intricate variation in the lifetimes seen in the CRTA analysis.

*c. Discussion*

The calculations on the five $XCo_8Sb_{24}$ models show that the fillers can reduce the $\kappa_{latt}$ of pristine $CoSb_3$ by up to 15 % by limiting the thermal transport through the low-lying optic modes from 2.5-6 THz, by reducing the mode group velocities and, for some of the fillers, suppressing the phonon lifetimes. Although this reduction is nowhere near as substantial as those seen in some filled skutterudites, nanostructuring could be used to reduce the heat transport through the acoustic modes. Calculations similar to those in Fig. 6 for the filled models suggest that, for example, nanostructuring to 100 nm could reduce the room-temperature $\kappa_{latt}$ of the filled models by ~50 %, in addition to the smaller reductions compared to pristine $CoSb_3$ afforded by filling (Figs. S2.25-2.29). Alternatively, fillers of a similar chemical nature to the heavier noble gases could be combined with a second filler to suppress both acoustic- and optic-mode transport - this strategy of introducing two fillers with different rattling frequencies has proven successful in experiments.[62]
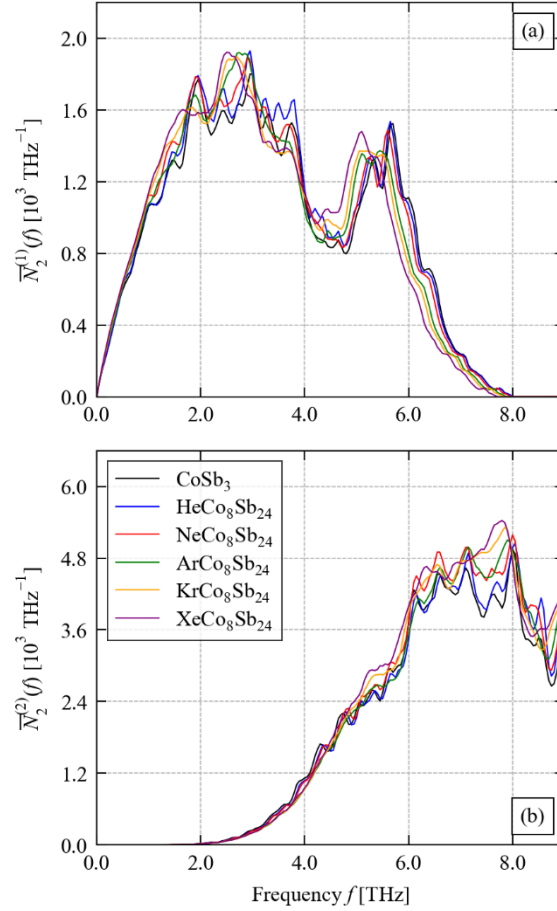
**Figure 11** Averaged weighted two-phonon joint density of states (w-JDoS) functions $\bar{N}_2^{(1)}(\omega)$ (a) and $\bar{N}_2^{(2)}(\omega)$ (b) for collision and decay processes, respectively, for $CoSb_3$ and $XCo_8Sb_{24}$ with X = He, Ne, Ar, Kr and Xe at $T = 300$ K. The two w-JDoS functions are defined in Eqs. 14-17.

Given that ~80 % of the heat transport in $CoSb_3$ is through the acoustic modes, the resonant-scattering and avoided-crossing mechanisms both predict that lowering the rattling frequency below 2.5 THz would produce a larger reduction in $\kappa_{latt}$. This is not possible with the five fillers studied here because the heavier noble gases interact more strongly with the framework. We can, however, perform a "thought experiment" to decouple the mass and interaction strength by changing the mass of the fillers while keeping the second- and third-order force constants fixed, and vice versa.

Fig. 12 shows how the rattling frequency and room-temperature $\kappa_{latt}$ vary for each filler as the mass $m_X$ is varied from He to Xe. The frequencies vary inversely with $m_X$ and fall below 2.5 THz when the mass of the weakly-interacting He filler is increased to $m_{Ar}$, $m_{Kr}$ and $m_{Xe}$, or when the mass of Ne is increased to $m_{Kr}$ and $m_{Xe}$. The changes in $\kappa_{latt}$ in Fig. 12b show two distinct effects. For higher $\tilde{f}_X$, the $\kappa_{latt}$ follow a general decreasing trend with $m_X$ to the maximum ~15 % reduction obtained with $XeCo_8Sb_{24}$. Once $\tilde{f}_X$ falls below a certain threshold, which from these tests appears to be around 1.5 THz, i.e. well within the acoustic bands, there is a large drop in the $\kappa_{latt}$.
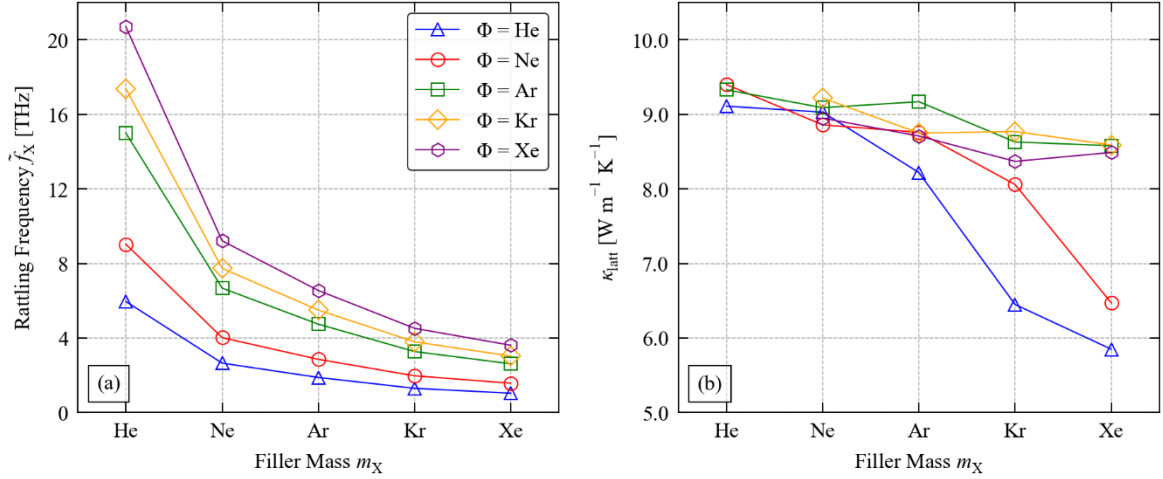
**Figure 12** Variation in the approximate filler rattling frequency $\tilde{f}_X$ (a) and 300 K lattice thermal conductivity $\kappa_{latt}$ (b) with the filler mass $m_X$ for fixed second- and third-order force constants $\Phi$.

The He and Ne calculations show that when the filler modes fall among the acoustic modes the $\kappa_{latt}$ can be reduced by up to 40 % compared to pristine $CoSb_3$. Using the CRTA analysis, we find that for He this is due to a 10-15 % reduction in the group velocities and a 20-30 % reduction in the lifetimes, while for Ne it is due to a 20 % reduction in the $v_\lambda$ and a 15 % reduction in the $\tau_\lambda$ (Figs. S2.30/S2.31). Comparison of the unfolded phonon band structures and projected phonon DoS curves of $HeCo_8Sb_{24}$ as the mass of the He atom is increased show that rattling frequencies within the acoustic bands lead to localised modes with narrow dispersion (Figs. S2.32-S2.35). Although there is some evidence of avoided crossings where the acoustic and filler modes cross, the CRTA analysis points to a minor effect on the group velocities, which suggests the reduced lifetimes are mainly due to a resonant scattering-like interaction with the filler modes.

We also note that lowering the masses of Kr and Xe, with the strongest filler-framework interactions, to that of He produces an unphysically large $\kappa_{latt}$. This combination results in rattling frequencies of 17.4 and 20.7 THz, which are both so far outside the frequency range of the $CoSb_3$ spectrum that there would be very few energy-conserving scattering channels to limit their modal $\kappa_\lambda$.

This analysis clearly shows, as per the "rattler" model of cage compounds, that the largest reductions in $\kappa_{latt}$ are obtained with heavy fillers that interact weakly with the framework. The mass is a known parameter, and the interaction strength, as we have shown, can be determined approximately from the second-order (harmonic) force constants, providing an efficient means to screen potential fillers theoretically.

## 4. Conclusions

In summary, we have used first-principles modelling to investigate the structural dynamics and thermal transport in pristine $CoSb_3$ and filled $XCo_8Sb_{24}$ containing a series of noble gas atoms.

The relaxation-time approximation provides a quantitative description of the thermal transport in $CoSb_3$ and highlights how synergistic nanostructuring could be used as an additional means to control the $\kappa_{latt}$ in these materials.

The rattling frequencies of the noble gas atoms are determined through a detailed balance of their atomic mass and how strongly they interact with the host framework, both of which increase from He to Xe. The heavier filler atoms suppress the heat transport through the low-lying optic modes, which accounts for ~20 % of the total $\kappa_{latt}$ in pristine $CoSb_3$, primarily by reducing the group velocity. The effect of the fillers on the phonon lifetimes depends intricately on changes in the phonon-phonon interaction strengths and changes in the number of energy-conserving scattering pathways for modes in different parts of the phonon spectrum. The heavier noble gases show comparatively weak phonon-phonon interactions, and their effect on the phonon lifetimes occurs mainly by providing additional scattering channels.

With the chemically-inert noble gas fillers, the effect of filling on the heat transport is effectively separated from any impact from the reduction or oxidation of the host framework that may occur with other filler chemistries. This makes these filled skutterudites an ideal "toy model" for exploring how the size and mass of filler atoms and their interaction with the host framework affect the thermal transport. However, we note that we would not expect these materials to be viable thermoelectrics for (at least) three reasons: (1) it would likely be impractical to introduce volatile inert gases such as these into $CoSb_3$, and to then retain them under the large temperature gradients across working thermoelectric devices; (2) the heavier noble gases, which have the largest impact on the $\kappa_{latt}$, are both rare and expensive; and (3) considerably larger reductions in $\kappa_{latt}$ have been demonstrated with other fillers.

In this vein, we have proposed various analyses that can be used to gain better insight into how fillers atoms suppress the thermal transport. Of particular note are the constant relaxation-time model to quantitatively attribute changes in $\kappa_{latt}$ to changes in the phonon mode group velocities and lifetimes, and the approximate model for phonon linewidths to attribute changes in lifetimes to changes in the phonon-phonon interaction strengths and the numbers of scattering pathways. These tools may prove useful both to better understand and to compare the impact of filler atoms on the heat transport in skutterudites and other cage compounds.

Finally, we have shown that approximate rattling frequencies, determined from the harmonic force constants, appear to be a useful predictor of the $\kappa_{latt}$ in the filled skutterudites. In particular, rattling frequencies in the range of the acoustic modes, obtained with heavy fillers that interact weakly with the $CoSb_3$ framework, are predicted to lead to the largest suppression of the thermal transport. Identifying descriptors to predict the interaction strength between the fillers and the framework (e.g. charge, electronegativity, and polarizability) is therefore likely to be a useful step towards the rational selection of fillers for controlling the heat transport in cage compounds.

## 5. Acknowledgements

of the calculations were performed on the UK Archer HPC facility *via* the UK Materials Chemistry Consortium (MCC), which is funded by the UK Engineering and Physical Sciences Research Council (grant nos. EP/L000202, EP/R029431). Some calculations were performed using the UoM Computational Shared Facility (CSF), which is maintained by UoM Research IT.

## 6. Data-Access Statement

Data from the modelling studies in this work including optimised structures, calculated force constants and phonon spectra, and raw data from the thermal-conductivity calculations are available to download from an online repository at [URL to be added on acceptance]. Data not available as supporting information or from the repository may be obtained from the authors on request. Some of the codes used to analyse the modelling data are available from the GitHub repository at: https://github.com/skelton-group/Phono3py-Power-Tools.

## 7. References

[1]     Freer R and Powell A V. 2020 Realising the potential of thermoelectric technology: A Roadmap *J. Mater. Chem. C* **8** 441–63

[2]     Tan G, Zhao L-D and Kanatzidis M G 2016 Rationally Designing High-Performance Bulk Thermoelectric Materials *Chem. Rev.* **116** 12123–49

[3]     Sootsman J R, Chung D Y and Kanatzidis M G 2009 New and Old Concepts in Thermoelectric Materials *Angew. Chemie Int. Ed.* **48** 8616–39

[4]     Slack G A 1995 New Materials and Performance Limits for Thermoelectric Cooling *CRC Handbook of Thermoelectrics* ed D M Rowe (London: CRC Press) p 407

[5]     Kleinke H 2010 New bulk materials for thermoelectric power generation: clathrates and complex antimonides *Chem. Mater.* **22** 604–11

[6]     Rull-Bravo M, Moure A, Fernández J F and Martín-González M 2015 Skutterudites as thermoelectric materials: Revisited *RSC Adv.* **5** 41653–67

[7]     Dolyniuk J A, Owens-Baird B, Wang J, Zaikina J V. and Kovnir K 2016 Clathrate thermoelectrics *Mater. Sci. Eng. R Reports* **108** 1–46

[8]     Rogl G and Rogl P 2019 Skutterudites: Progress and challenges *Novel Thermoelectric Materials and Device Design Concepts* (Springer International Publishing) pp 177–201

[9]     Ren P, Liu Y, He J, Lv T, Gao J and Xu G 2018 Recent advances in inorganic material thermoelectrics *Inorg. Chem. Front.* **5** 2380–98

[10]     Morelli D T, Caillat T, Fleurial J P, Borshchevsky A, Vandersande J, Chen B and Uher C 1995 Low-temperature transport properties of $p$-type $CoSb_3$ *Phys. Rev. B* **51** 9622–8

[11]     Caillat T, Borshchevsky A and Fleurial J P 1996 Properties of single crystalline semiconducting $CoSb_3$ *J. Appl. Phys.* **80** 4442–9

[12]     Kawaharada Y, Kurosaki K, Uno M and Yamanaka S 2001 Thermoelectric properties of $CoSb_3$ *J. Alloys Compd.* **315** 193–7

[13]     Itoh T, Hattori E and Kitagawa K 2008 Thermoelectric properties of iron- and lanthanum-doped $CoSb_3$ compounds by pulse discharge sintering *J. Propuls. Power* **24** 359–64

[14]     Lei Y, Gao W, Zheng R, Li Y, Chen W, Zhang L, Wan R, Zhou H, Liu Z and Chu P K 2019 Ultrafast Synthesis of Te-Doped $CoSb_3$ with Excellent Thermoelectric Properties *ACS Appl. Energy Mater.* **2** 4477–85

[15]     Zhao X Y, Shi X, Chen L D, Zhang W Q, Zhang W B and Pel Y Z 2006 Synthesis and thermoelectric properties of Sr-filled skutterudite $Sr_yCo_4Sb_{12}$ *J. Appl. Phys.* **99** 053711

[16]     Pei Y Z, Yang J, Chen L D, Zhang W, Salvador J R and Yang J 2009 Improving thermoelectric performance of caged compounds through light-element filling *Appl. Phys. Lett.* **95** 042101

[17]     Li G, Kurosaki K, Ohishi Y, Muta H and Yamanaka S 2013 Thermoelectric properties of indium-added Skutterudites $InxCo4Sb12$ *J. Electron. Mater.* **42** 1463–8

[18]     Battabyal M, Priyadarshini B, Pradipkanti L, Satapathy D K and Gopalan R 2016 Phase stability and lattice thermal conductivity reduction in $CoSb_3$ skutterudites, doped with chalcogen atoms *AIP Adv.* **6** 075308

[19]     Li X, Xu B, Zhang L, Duan F, Yan X, Yang J and Tian Y 2014 Synthesis of iodine filled $CoSb_3$ with extremely low thermal conductivity *J. Alloys Compd.* **615** 177–80

[20]     Zheng Y, Yu M, Li H, Zuo G, Jiang H, Huang H and Yin L 2014 Synthesis and thermoelectric properties of Cd-filled $CoSb_3$ *High Press. Res.* **34** 281–8

[21]     Pei Y Z, Bai S Q, Zhao X Y, Zhang W and Chen L D 2008 Thermoelectric properties of $Eu_yCo_4Sb_{12}$ filled skutterudites *Solid State Sci.* **10** 1422–8

[22]     Mona Y, Hayashi J I, Kawamura Y, Kihou K, Nishiate H, Lee C H and Sekine C 2018 Thermoelectric properties of partially filled skutterudites $R_xCo_4Sb_{12}$ ($R$ = Ce and Nd) synthesized under high pressures *Jpn. J. Appl. Phys.* **57** 125506

[23]     Lei Y, Ma L, Zheng R, Li Y, Wan R, Chen W, Zhou H and Gao W 2019 Thermoelectric performance of skutterudite $Ni_xCo_{4-x}Sb_{12}$ rapidly synthesized by microwave heating *J. Mater. Sci. Mater. Electron.* **30** 5929–35

[24]     Bai S Q, Huang X Y, Chen L D, Zhang W, Zhao X Y and Zhou Y F 2010 Thermoelectric properties of n-type $Sr_xM_yCo_4Sb_{12}$ ($M$ = Yb, Ba) double-filled skutterudites *Appl. Phys. A* **100** 1109–14

[25]     Shi X, Yang J, Salvador J R, Chi M, Cho J Y, Wang H, Bai S, Yang J, Zhang W and Chen L 2011 Multiple-Filled Skutterudites: High Thermoelectric Figure of Merit through Separately Optimizing Electrical and Thermal Transports *J. Am. Chem. Soc.* **133** 7837–46

[26]     Zhang S, Xu S, Gao H, Lu Q, Lin T, He P and Geng H 2020 Characterization of multiple-filled skutterudites with high thermoelectric performance *J. Alloys Compd.* **814** 152272

[27]     Tang X F, Chen L D, Goto T, Hirai T and Yuan R Z 2001 Synthesis and thermoelectric properties of filled skutterudite compounds $CeyFexCo4-xSb12$ by solid state reaction *J. Mater. Sci.* **36** 5435–9

[28]     Delaire O, Ma J, Marty K, May A F, McGuire M A, Du M-H, Singh D J, Podlesnyak A, Ehlers G, Lumsden M D and C S B 2011 Giant anharmonic phonon scattering in PbTe. *Nat. Mater.* **10** 614–9

[29]    Li C W, Hong J, May A F, Bansal D, Chi S, Hong T, Ehlers G and Delaire O 2015 Orbitally driven giant phonon anharmonicity in SnSe *Nat. Phys.* **11** 1063–9

[30]    Skelton J M, Burton L A, Parker S C, Walsh A, Kim C-E, Soon A, Buckeridge J, Sokol A A, Catlow C R A, Togo A and Tanaka I 2016 Anharmonicity in the High-Temperature *Cmcm* Phase of SnSe: Soft Modes and Three-Phonon Interactions *Phys. Rev. Lett.* **117**

[31]    Whalley L D, Skelton J M, Frost J M and Walsh A 2016 Phonon anharmonicity, lifetimes, and thermal transport in $CH_3NH_3PbI_3$ from many-body perturbation theory *Phys. Rev. B* **94** 220301(R)

[32]    Gold-Parker A, Gehring P M, Skelton J M, Smith I C, Parshall D, Frost J M, Karunadasa H I, Walsh A and Toney M F 2018 Acoustic phonon lifetimes limit thermal transport in methylammonium lead iodide. *Proc. Natl. Acad. Sci. U. S. A.* **115** 11905–10

[33]    Carrete J, Li W, Mingo N, Wang S and Curtarolo S 2014 Finding Unprecedentedly Low-Thermal-Conductivity Half-Heusler Semiconductors via High-Throughput Materials Modeling *Phys. Rev. X* **4** 011019

[34]    Alberi K, Nardelli M B, Zakutayev A, Mitas L, Curtarolo S, Jain A, Fornari M, Marzari N, Takeuchi I, Green M L, Kanatzidis M, Toney M F, Butenko S, Meredig B, Lany S, Kattner U, Davydov A, Toberer E S, Stevanovic V, Walsh A, Park N-G, Aspuru-Guzik A, Tabor D P, Nelson J, Murphy J, Setlur A, Gregoire J, Li H, Xiao R, Ludwig A, Martin L W, Rappe A M, Wei S-H and Perkins J 2019 The 2019 materials by design roadmap *J. Phys. D. Appl. Phys.* **52** 013001

[35]    Rahim W, Skelton J M and Scanlon D O 2020 α-$Bi_2Sn_2O_7$: A potential room temperature n-type oxide thermoelectric *J. Mater. Chem. A* **8**

[36]    Li W and Mingo N 2014 Thermal conductivity of fully filled skutterudites: Role of the filler *Phys. Rev. B* **89** 184304

[37]    Li W and Mingo N 2014 Lattice dynamics and thermal conductivity of skutterudites CoSb3 and IrSb3 from first principles: Why IrSb3 is a better thermal conductor than CoSb3 *Phys. Rev. B* **90** 094302

[38]    Li W and Mingo N 2015 Ultralow lattice thermal conductivity of the fully filled skutterudite $YbFe_4Sb_{12}$ due to the flat avoided-crossing filler modes *Phys. Rev. B* **91** 144304

[39]    Guo R, Wang X and Huang B 2015 Thermal conductivity of skutterudite $CoSb_3$ from first principles: Substitution and nanoengineering effects *Sci. Rep.* **5** 1–9

[40]    Liu Z, Yang X, Chen G and Zhai P 2016 Molecular dynamics study of the influence of Sb-vacancy defects on the lattice thermal conductivity of crystalline $CoSb_3$ *Comput. Mater. Sci.* **124** 403–10

[41]    Kresse G and Hafner J 1993 Ab initio molecular dynamics for liquid metals *Phys. Rev. B* **47** 558(R)-561(R)

[42]    Monkhorst H J and Pack J D 1976 Special points for Brillouin-zone integrations *Phys. Rev. B* **13** 5188–92

[43]    Perdew J P, Ruzsinszky A, Csonka G I, Vydrov O A, Scuseria G E, Constantin L A, Zhou X and Burke K 2008 Restoring the Density-Gradient Expansion for Exchange in Solids and Surfaces *Phys. Rev. Lett.* **100** 136406

[44]     Dudarev S L, Botton G A, Savrasov S Y, Humphreys C J and Sutton A P 1998 Electron-energy-loss spectra and the structural stability of nickel oxide: An LSDA+U study *Phys. Rev. B* **57** 1505–9

[45]     Grimme S, Antony J, Ehrlich S and Krieg H 2010 A consistent and accurate *ab initio* parametrization of density functional dispersion correction (DFT-D) for the 94 elements H-Pu *J. Chem. Phys.* **132** 154104

[46]     Blöchl P E 1994 Projector augmented-wave method *Phys. Rev. B* **50** 17953–79

[47]     Kresse G and Joubert D 1999 From ultrasoft pseudopotentials to the projector augmented-wave method *Phys. Rev. B* **59** 1758–75

[48]     Togo A and Tanaka I 2015 First principles phonon calculations in materials science *Scr. Mater.* **108** 1–5

[49]     Togo A, Chaput L and Tanaka I 2015 Distributions of phonon lifetimes in Brillouin zones *Phys. Rev. B* **91** 094306

[50]     Parlinski K, Li Z Q and Kawazoe Y 1997 First-Principles Determination of the Soft Mode in Cubic $ZrO_2$ *Phys. Rev. Lett.* **78** 4063–6

[51]     Allen P B, Berlijn T, Casavant D A and Soler J M 2013 Recovering hidden Bloch character: Unfolding electrons, phonons, and slabs *Phys. Rev. B* **87** 085322

[52]     Lutz H D and Kliche G 1982 Far-Infrared Reflection Spectra, Optical and Dielectric Constants, Effective Charges, and Lattice Dynamics of the Skutterudites $CoP_3$, $CoAs_3$, and $CoSb_3$ *Phys. Status Solidi* **112** 549–57

[53]     Schmidt T, Kliche G and Lutz H D 1987 Structure refinement of skutterudite-type cobalt triantimonide, $CoSb_3$ *Acta Crystallogr. Sect. C* **43** 1678–9

[54]     Rotter M, Rogl P, Grytsiv A, Wolf W, Krisch M and Mirone A 2008 Lattice dynamics of skutterudites: Inelastic x-ray scattering on $CoSb_3$ *Phys. Rev. B* **77** 144301

[55]     Momma K and Izumi F 2011 VESTA 3 for three-dimensional visualization of crystal, volumetric and morphology data *J. Appl. Crystallogr.* **44** 1272–6

[56]     Nolas G S, Slack G A, Caillat T and Meisner G P 1996 Raman scattering study of antimony-based skutterudites *J. Appl. Phys.* **79** 2622–6

[57]     Nolas G S and Kendziora C A 1999 Raman spectroscopy investigation of lanthanide-filled and unfilled skutterudites *Phys. Rev. B* **59** 6189–92

[58]     Leszczynski J, Wojciechowski K T and Malecki A L 2011 Studies on thermal decomposition and oxidation of $CoSb_3$ *J. Therm. Anal. Calorim.* **105** 211–22

[59]     Toberer E S, Zevalkink A and Snyder G J 2011 Phonon engineering through crystal chemistry *J. Mater. Chem.* **21** 15843–52

[60]     Dong J, Sankey O F and Myles C W 2001 Theoretical study of the lattice thermal conductivity in Ge framework semiconductors *Phys. Rev. Lett.* **86** 2361–4

[61]     Christensen M, Abrahamsen A B, Christensen N B, Juranyi F, Andersen N H, Lefmann K, Andreasson J, Bahl C R H and Iversen B B 2008 Avoided crossing of rattler modes in thermoelectric materials *Nat.*

*Mater.* **7** 811–5

[62]    Yang J, Zhang W, Bai S Q, Mei Z and Chen L D 2007 Dual-frequency resonant phonon scattering in Ba$_x$R$_y$Co$_4$Sb$_{12}$ ($R$ = La, Ce, and Sr) *Appl. Phys. Lett.* **90** 192111

# Impact of noble-gas filler atoms on the lattice thermal conductivity of CoSb$_3$ skutterudites: first-principles modelling

# Electronic supporting information

Jianqin Tang[1] and Jonathan M. Skelton[1*]

[1] Department of Chemistry, University of Manchester, Oxford Road, Manchester M13 9PL, UK

[*] Corresponding author. E-Mail: jonathan.skelton@manchester.ac.uk.

# 1. Computational modelling

*a. Supercell size for determining the second- and third-order interatomic force constants*

To verify the suitability of our chosen supercell for computing the second-order interatomic force constants (IFCs), we compared phonon dispersion and density of states (DoS) curves for $CoSb_3$ obtained from IFCs computed in $2 \times 2 \times 2$ expansions of the primitive and conventional cells containing 128 and 256 atoms respectively. The technical parameters listed in the text were used for the calculations on the primitive cell, with $4 \times 4 \times 4$ and $2 \times 2 \times 2$ **k**-point meshes used for the base cell and supercell expansion. As shown in Figure S1.1, the results are practically superimposable.

To verify the suitability of the base $CoSb_3$ conventional cell for computing the third-order IFCs, we also calculated third-order IFCs in the base primitive cell with 16 atoms and a $2 \times 2 \times 2$ expansion with 128 atoms. As shown in Figures S1.2 and Table S1, the thermal conductivity calculated using the conventional-cell model is ~10 % larger than the primitive-cell model with the small third-order supercell, but is within 1 % of the model using the larger 128-atom third-order supercell.

These tests therefore suggest that the conventional-cell model is an appropriate balance between accuracy and cost, and is particularly convenient for these calculations given that it makes it possible to model filled $CoSb_3$ with a reasonable filling fraction.
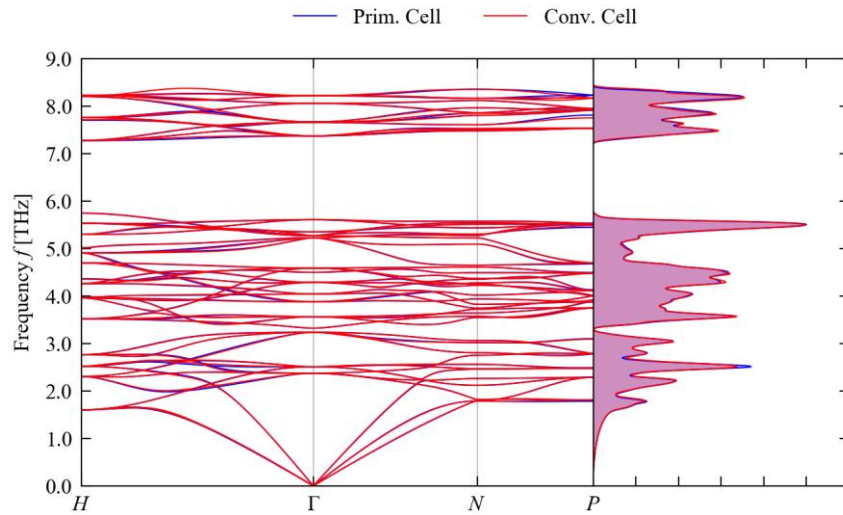


**Figure S1.1** Comparison of the phonon dispersion and density of states $g(f)$ (DoS) of pristine $CoSb_3$ calculated using force constants obtained in $2 \times 2 \times 2$ supercell expansions of the primitive (blue) and conventional cells (red) with 128 and 256 atoms, respectively.
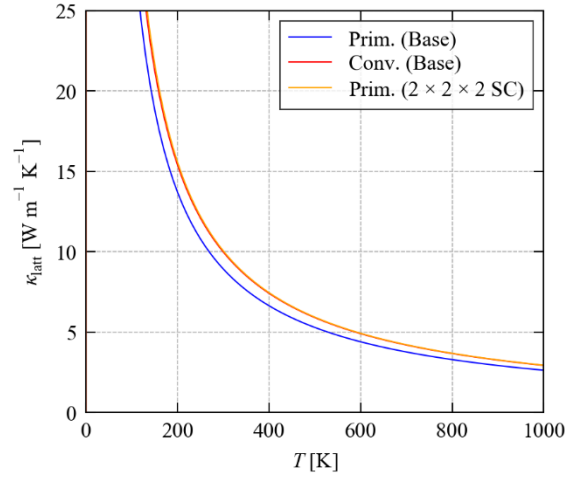
**Figure S1.2** Lattice thermal-conductivity $\kappa_{\text{latt}}$ of pristine $CoSb_3$ as a function of temperature calculated using three models: (1) the primitive cell with the 2$^{\text{nd}}$-order IFCs computed using a $2 \times 2 \times 2$ supercell expansion and the 3$^{\text{rd}}$-order IFCs evaluated in the base cell (blue); (2) the conventional cell (red); and (3) the primitive cell with the 2$^{\text{nd}}$- and 3$^{\text{rd}}$-order IFCs computed using a $2 \times 2 \times 2$ supercell expansion (orange). The $\kappa_{\text{latt}}$ of the conventional cell model was computed from modal properties evaluated on a $9 \times 9 \times 9$ grid of phonon wavevectors **q**, while the $\kappa_{\text{latt}}$ of the primitive cell models was computed on $11 \times 11 \times 11$ grids with ~2× as many wavevectors in proportion to their 2× larger Brillouin zones.

*b. Numerical quality of the interatomic force constants*

A good proxy for the numerical quantity of the calculated force constants is to compare thermal-conductivity calculations performed with and without applying symmetrisation to the force constants. Figures S1.3-S1.10 compare thermal-conductivity curves for all the pristine $CoSb_3$ and filled $XCo_8Sb_{24}$ models considered in this work computed with and without force-constant symmetrisation, and values at 300 and 600 K are compared in Table S1.2. We find a maximum absolute difference of 1.05 % in the two sets of values, which indicates that the calculated force constants have a low level of numerical noise.
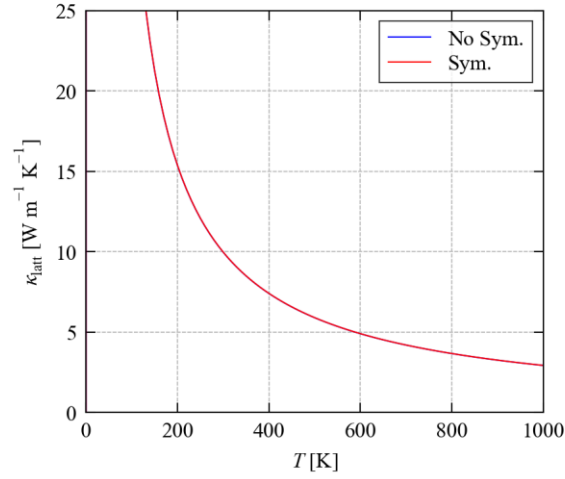
**Figure S1.3** Lattice thermal-conductivity $\kappa_{latt}$ of pristine $CoSb_3$ calculated with (red) and without (blue) force-constant symmetrisation (conventional cell model). In both cases the $\kappa_{latt}$ was computed from modal properties evaluated on a $9 \times 9 \times 9$ grid of phonon wavevectors $\mathbf{q}$.
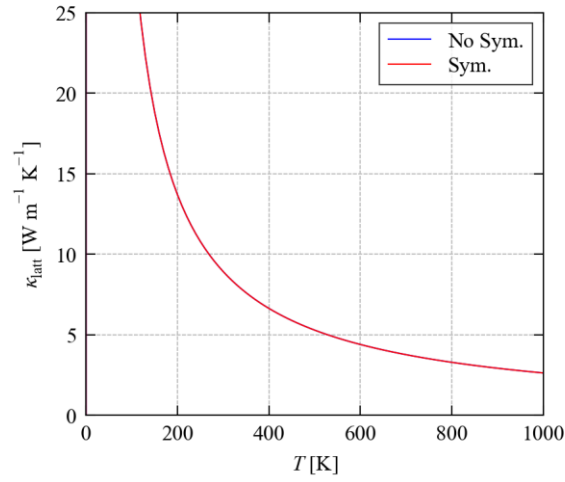


**Figure S1.4** Lattice thermal-conductivity $\kappa_{latt}$ of pristine $CoSb_3$ calculated with (red) and without (blue) force-constant symmetrisation (primitive cell model with $2^{nd}$-order IFCs computed using a $2 \times 2 \times 2$ supercell expansion and $3^{rd}$-order IFCs evaluated in the base cell). In both cases the $\kappa_{latt}$ was computed from modal properties evaluated on an $11 \times 11 \times 11$ grid of phonon wavevectors $\mathbf{q}$.
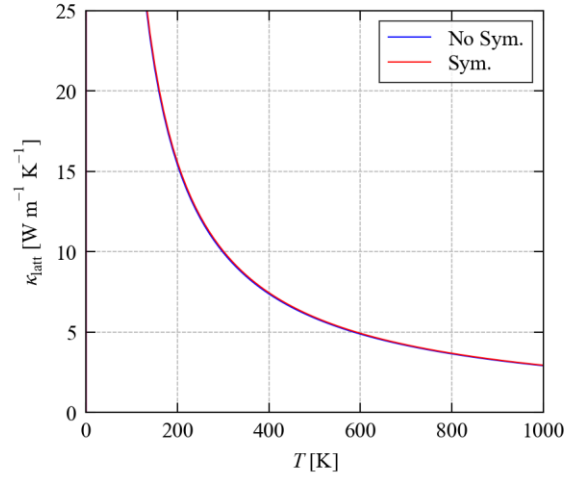
**Figure S1.5** Lattice thermal-conductivity $\kappa_{latt}$ of pristine CoSb$_3$ calculated with (red) and without (blue) force-constant symmetrisation (primitive cell model with 2$^{nd}$- and 3$^{rd}$-order IFCs computed using a $2 \times 2 \times 2$ supercell expansion). In both cases the $\kappa_{latt}$ was computed from modal properties evaluated on an $11 \times 11 \times 11$ grid of phonon wavevectors **q**.
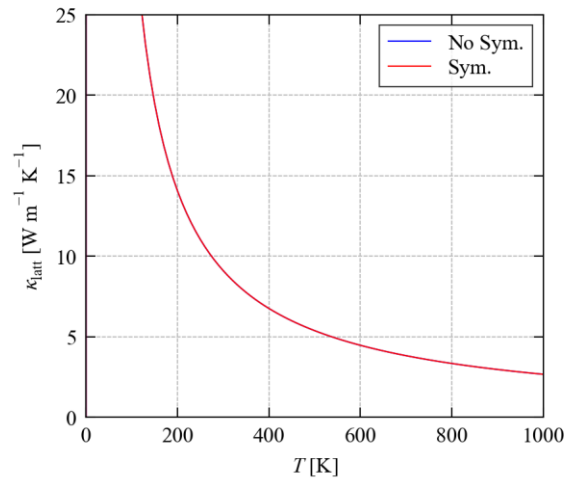


**Figure S1.6** Lattice thermal-conductivity $\kappa_{latt}$ of HeCo$_8$Sb$_{24}$ calculated with (red) and without (blue) force-constant symmetrisation. In both cases the $\kappa_{latt}$ was computed from modal properties evaluated on a $9 \times 9 \times 9$ grid of phonon wavevectors **q**.
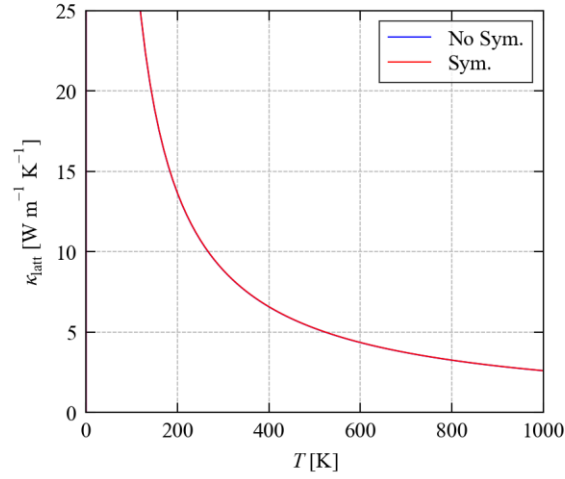
**Figure S1.7** Lattice thermal-conductivity $\kappa_{latt}$ of NeCo$_8$Sb$_{24}$ calculated with (red) and without (blue) force-constant symmetrisation. In both cases the $\kappa_{latt}$ was computed from modal properties evaluated on a $9 \times 9 \times 9$ grid of phonon wavevectors $\mathbf{q}$.
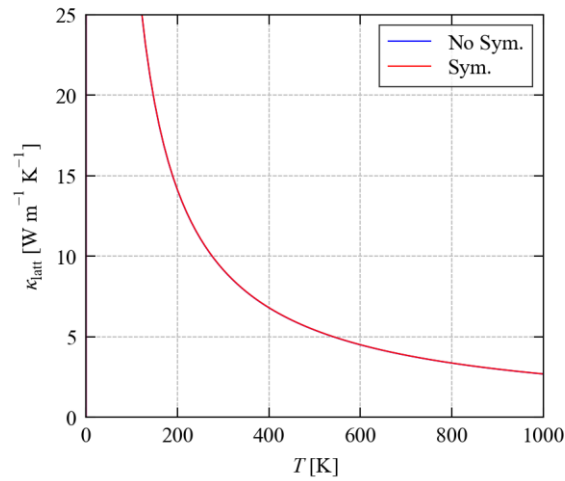


**Figure S1.8** Lattice thermal-conductivity $\kappa_{latt}$ of ArCo$_8$Sb$_{24}$ calculated with (red) and without (blue) force-constant symmetrisation. In both cases the $\kappa_{latt}$ was computed from modal properties evaluated on a $9 \times 9 \times 9$ grid of phonon wavevectors $\mathbf{q}$.
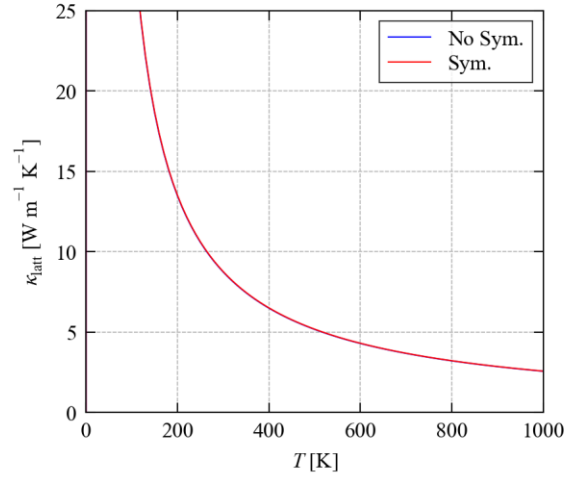
**Figure S1.9** Lattice thermal-conductivity $\kappa_{latt}$ of KrCo$_8$Sb$_{24}$ calculated with (red) and without (blue) force-constant symmetrisation. In both cases the $\kappa_{latt}$ was computed from modal properties evaluated on a $9 \times 9 \times 9$ grid of phonon wavevectors **q**.
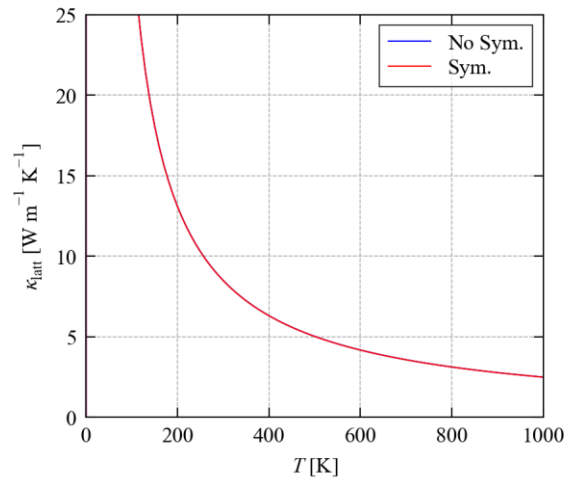


**Figure S1.10** Lattice thermal-conductivity $\kappa_{latt}$ of XeCo$_8$Sb$_{24}$ calculated with (red) and without (blue) force-constant symmetrisation. In both cases the $\kappa_{latt}$ was computed from modal properties evaluated on a $9 \times 9 \times 9$ grid of phonon wavevectors **q**.

| Cell | IFC Supercell | | Sampling Mesh | $T = 300$ K | | $T = 600$ K | |
|---|---|---|---|---|---|---|---|
| | $2^{nd}$-order | $3^{rd}$-order | | $\kappa_{latt}$ [W m$^{-1}$ K$^{-1}$] | $\Delta$ [%] | $\kappa_{latt}$ [W m$^{-1}$ K$^{-1}$] | $\Delta$ [%] |
| Conv. | $2 \times 2 \times 2$ | Base | $9 \times 9 \times 9$ | 9.981 | - | 4.909 | - |
| Prim. | $2 \times 2 \times 2$ | Base | $11 \times 11 \times 11$ | 8.927 | -10.6 | 4.402 | -10.3 |
| Prim. | $2 \times 2 \times 2$ | $2 \times 2 \times 2$ | $11 \times 11 \times 11$ | 10.054 | 0.73 | 4.931 | 0.45 |

**Table S1.1** Comparison of the calculated lattice thermal conductivity $\kappa_{latt}$ of CoSb$_3$ at $T = 300$ and 600 K obtained using three different models, *viz.* (1) $2^{nd}$- and $3^{rd}$-order IFCs computed in a $2 \times 2 \times 2$ expansion and a single unit of the 32-atom conventional cell, (2) $2^{nd}$- and $3^{rd}$-order IFCs computed in a $2 \times 2 \times 2$ expansion and a single unit of the 16-atom primitive cell; and (3) $2^{nd}$- and $3^{rd}$-order IFCs computed in a $2 \times 2 \times 2$ expansion of the 16-atom primitive cell. The $\kappa_{latt}$ for the three models were evaluated using the sampling meshes indicated.

| | | $T = 300$ K | | | $T = 600$ K | | |
|---|---|---|---|---|---|---|---|
| | | $\kappa_{latt}$ [W m$^{-1}$ K$^{-1}$] | | | $\kappa_{latt}$ [W m$^{-1}$ K$^{-1}$] | | |
| | Sampling Mesh | No Sym. | Sym. | $\Delta$ [%] | No Sym. | Sym. | $\Delta$ [%] |
| CoSb$_3$ (Conv.) | $9 \times 9 \times 9$ | 9.974 | 9.981 | 0.08 | 4.905 | 4.909 | 0.08 |
| CoSb$_3$ (Prim.) | $11 \times 11 \times 11$ | 8.929 | 8.927 | -0.02 | 4.403 | 4.402 | -0.02 |
| CoSb$_3$ (Prim. - $2 \times 2 \times 2$ SC) | $11 \times 11 \times 11$ | 9.950 | 10.054 | 1.04 | 4.881 | 4.931 | 1.02 |
| HeCo$_8$Sb$_{24}$ | $9 \times 9 \times 9$ | 9.110 | 9.112 | 0.02 | 4.476 | 4.476 | 0.01 |
| NeCo$_8$Sb$_{24}$ | $9 \times 9 \times 9$ | 8.852 | 8.864 | 0.13 | 4.355 | 4.360 | 0.13 |
| ArCo$_8$Sb$_{24}$ | $9 \times 9 \times 9$ | 9.160 | 9.171 | 0.12 | 4.506 | 4.512 | 0.12 |
| KrCo$_8$Sb$_{24}$ | $9 \times 9 \times 9$ | 8.744 | 8.768 | 0.28 | 4.300 | 4.312 | 0.28 |
| XeCo$_8$Sb$_{24}$ | $9 \times 9 \times 9$ | 8.503 | 8.494 | -0.10 | 4.183 | 4.179 | -0.10 |

**Table S1.2** Comparison of the calculated lattice thermal conductivity $\kappa_{latt}$ at $T = 300$ and 600 K for the pristine CoSb$_3$ and filled XCo$_8$Sb$_{24}$ models considered in this work, obtained with and without force-constant symmetrisation using the sampling meshes indicated.

*c. Brillouin-zone sampling meshes for the thermal-conductivity calculations*

Using the single-mode relaxation-time approximation, the macroscopic thermal conductivity $\kappa_{\text{latt}}$ is calculated as a sum of modal contributions evaluated on a regular grid of wavevectors sampling the phonon Brillouin zone (Eq. 2 in the text). Appropriate sampling meshes for each of the models investigated in this work were determined by explicit convergence testing to be $9 \times 9 \times 9$ for the pristine and filled models based on the CoSb$_3$ conventional cell and $11 \times 11 \times 11$ for the pristine model based on the primitive cell.

Figs. S1.11-S1.18 plot for each of the models the thermal conductivity as a function of temperature obtained using a series of sampling meshes. Tables S1.3-S1.10 compare $\kappa_{\text{latt}}$ values at $T = 300$ and 600 K on each of the meshes tested to the chosen converged meshes. For the pristine and filled models based on the conventional cell, the thermal conductivities calculated using the $9 \times 9 \times 9$ sampling meshes differ by at most 2.7 % compared to those calculates using larger $11 \times 11 \times 11$ meshes. We note in passing that for most of the models sampling meshes with an odd number of subdivisions appear to converge faster than "even" meshes, which we attribute to a flattening of the acoustic mode dispersion close to the zone boundary (c.f. Fig. 2 in the text).

Finally, a smaller $7 \times 7 \times 7$ mesh was used to compare the two-phonon joint density of states (w-JDoS) functions and averaged phonon-phonon interaction strengths for the pristine and filled models based on the CoSb$_3$ conventional cell, and to investigate the effect of varying the atomic mass of the noble gas atoms in the filled models. The thermal conductivities calculated using these reduced meshes are within 1-5 % of those obtained using the $9 \times 9 \times 9$ meshes, and the approximately twofold reduction in the number of grid points makes the post processing much less computationally intensive.

| | $T = 300$ K | | $T = 600$ K | |
|---|---|---|---|---|
| Sampling Mesh | $\kappa_{\text{latt}}$ [W m$^{-1}$ K$^{-1}$] | $\Delta$ [%] | $\kappa_{\text{latt}}$ [W m$^{-1}$ K$^{-1}$] | $\Delta$ [%] |
| $2 \times 2 \times 2$ | 4.135 | -58.6 | 2.036 | -58.5 |
| $3 \times 3 \times 3$ | 8.316 | -16.7 | 4.097 | -16.5 |
| $4 \times 4 \times 4$ | 9.071 | -9.12 | 4.463 | -9.09 |
| $5 \times 5 \times 5$ | 9.692 | -2.90 | 4.769 | -2.86 |
| $6 \times 6 \times 6$ | 9.549 | -4.33 | 4.699 | -4.27 |
| $7 \times 7 \times 7$ | 9.872 | -1.10 | 4.857 | -1.06 |
| $8 \times 8 \times 8$ | 9.853 | -1.29 | 4.847 | -1.26 |
| $9 \times 9 \times 9$ | 9.981 | 0.00 | 4.909 | 0.00 |
| $10 \times 10 \times 10$ | 10.007 | 0.26 | 4.922 | 0.26 |
| $11 \times 11 \times 11$ | 10.093 | 1.12 | 4.965 | 1.14 |

**Table S1.3** Calculated lattice thermal conductivity $\kappa_{\text{latt}}$ at $T = 300$ and 600 K for pristine CoSb$_3$ obtained with the series of sampling meshes shown in Fig. 1.11 (conventional cell model).

| Sampling Mesh | T = 300 K | | T = 600 K | |
| --- | --- | --- | --- | --- |
| | $\kappa_{latt}$ [W m$^{-1}$ K$^{-1}$] | $\Delta$ [%] | $\kappa_{latt}$ [W m$^{-1}$ K$^{-1}$] | $\Delta$ [%] |
| $2 \times 2 \times 2$ | 0.000 | -100.00 | -4.402 | -100.00 |
| $3 \times 3 \times 3$ | 6.054 | -32.18 | -1.407 | -31.95 |
| $4 \times 4 \times 4$ | 8.118 | -9.06 | -0.392 | -8.90 |
| $5 \times 5 \times 5$ | 8.467 | -5.15 | -0.222 | -5.05 |
| $6 \times 6 \times 6$ | 8.433 | -5.53 | -0.244 | -5.53 |
| $7 \times 7 \times 7$ | 8.797 | -1.45 | -0.061 | -1.39 |
| $8 \times 8 \times 8$ | 8.803 | -1.38 | -0.059 | -1.34 |
| $9 \times 9 \times 9$ | 8.818 | -1.22 | -0.053 | -1.21 |
| $10 \times 10 \times 10$ | 8.734 | -2.16 | -0.095 | -2.17 |
| $11 \times 11 \times 11$ | 8.927 | 0.00 | 0.000 | 0.00 |

**Table S1.4** Calculated lattice thermal conductivity $\kappa_{latt}$ at $T$ = 300 and 600 K for pristine CoSb$_3$ obtained with the series of sampling meshes shown in Fig. 1.12 (primitive cell model with 2$^{nd}$-order IFCs computed using a 2 $\times$ 2 $\times$ 2 supercell expansion and 3$^{rd}$-order IFCs evaluated in the base cell).

| Sampling Mesh | T = 300 K | | T = 600 K | |
| --- | --- | --- | --- | --- |
| | $\kappa_{latt}$ [W m$^{-1}$ K$^{-1}$] | $\Delta$ [%] | $\kappa_{latt}$ [W m$^{-1}$ K$^{-1}$] | $\Delta$ [%] |
| $2 \times 2 \times 2$ | 0.000 | -100.00 | 0.000 | -100.00 |
| $3 \times 3 \times 3$ | 6.241 | -37.93 | 3.085 | -37.43 |
| $4 \times 4 \times 4$ | 8.650 | -13.96 | 4.267 | -13.47 |
| $5 \times 5 \times 5$ | 9.109 | -9.40 | 4.483 | -9.08 |
| $6 \times 6 \times 6$ | 9.337 | -7.13 | 4.587 | -6.97 |
| $7 \times 7 \times 7$ | 9.847 | -2.06 | 4.838 | -1.89 |
| $8 \times 8 \times 8$ | 9.781 | -2.71 | 4.805 | -2.57 |
| $9 \times 9 \times 9$ | 9.873 | -1.80 | 4.845 | -1.75 |
| $10 \times 10 \times 10$ | 9.823 | -2.29 | 4.818 | -2.29 |
| $11 \times 11 \times 11$ | 10.054 | 0.00 | 4.931 | 0.00 |

**Table S1.5** Calculated lattice thermal conductivity $\kappa_{latt}$ at $T$ = 300 and 600 K for pristine CoSb$_3$ obtained with the series of sampling meshes shown in Fig. 1.13 (primitive cell model with 2$^{nd}$- and 3$^{rd}$-order IFCs computed using a 2 $\times$ 2 $\times$ 2 supercell expansion).

| Sampling Mesh | T = 300 K | | T = 600 K | |
| --- | --- | --- | --- | --- |
| | $\kappa_{latt}$ [W m$^{-1}$ K$^{-1}$] | $\Delta$ [%] | $\kappa_{latt}$ [W m$^{-1}$ K$^{-1}$] | $\Delta$ [%] |
| $2 \times 2 \times 2$ | 0.157 | -98.28 | 0.077 | -98.27 |
| $3 \times 3 \times 3$ | 7.757 | -14.86 | 3.818 | -14.70 |
| $4 \times 4 \times 4$ | 6.422 | -29.51 | 3.153 | -29.56 |
| $5 \times 5 \times 5$ | 8.825 | -3.15 | 4.336 | -3.12 |
| $6 \times 6 \times 6$ | 7.746 | -14.99 | 3.807 | -14.95 |
| $7 \times 7 \times 7$ | 9.018 | -1.03 | 4.432 | -0.99 |
| $8 \times 8 \times 8$ | 8.082 | -11.30 | 3.970 | -11.31 |
| $9 \times 9 \times 9$ | 9.112 | 0.00 | 4.476 | 0.00 |
| $10 \times 10 \times 10$ | 8.288 | -9.03 | 4.071 | -9.05 |
| $11 \times 11 \times 11$ | 9.150 | 0.43 | 4.496 | 0.44 |

**Table S1.6** Calculated lattice thermal conductivity $\kappa_{latt}$ at $T$ = 300 and 600 K for HeCo$_8$Sb$_{32}$ obtained with the series of Brillouin-zone sampling meshes shown in Fig. 1.14.

| Sampling Mesh | $T = 300$ K | | $T = 600$ K | |
|---|---|---|---|---|
| | $\kappa_{latt}$ [W m$^{-1}$ K$^{-1}$] | $\Delta$ [%] | $\kappa_{latt}$ [W m$^{-1}$ K$^{-1}$] | $\Delta$ [%] |
| $2 \times 2 \times 2$ | 0.000 | -100.00 | 0.000 | -100.00 |
| $3 \times 3 \times 3$ | 7.395 | -16.57 | 3.644 | -16.44 |
| $4 \times 4 \times 4$ | 6.451 | -27.22 | 3.173 | -27.23 |
| $5 \times 5 \times 5$ | 8.631 | -2.63 | 4.247 | -2.59 |
| $6 \times 6 \times 6$ | 7.581 | -14.47 | 3.730 | -14.45 |
| $7 \times 7 \times 7$ | 8.523 | -3.85 | 4.194 | -3.81 |
| $8 \times 8 \times 8$ | 7.774 | -12.29 | 3.824 | -12.30 |
| $9 \times 9 \times 9$ | 8.864 | 0.00 | 4.360 | 0.00 |
| $10 \times 10 \times 10$ | 7.961 | -10.19 | 3.915 | -10.20 |
| $11 \times 11 \times 11$ | 8.774 | -1.02 | 4.316 | -1.00 |

**Table S1.7** Calculated lattice thermal conductivity $\kappa_{latt}$ at $T = 300$ and 600 K for NeCo$_8$Sb$_{32}$ obtained with the series of Brillouin-zone sampling meshes shown in Fig. 1.15.

| Sampling Mesh | $T = 300$ K | | $T = 600$ K | |
|---|---|---|---|---|
| | $\kappa_{latt}$ [W m$^{-1}$ K$^{-1}$] | $\Delta$ [%] | $\kappa_{latt}$ [W m$^{-1}$ K$^{-1}$] | $\Delta$ [%] |
| $2 \times 2 \times 2$ | 0.000 | -100.00 | 0.000 | -100.00 |
| $3 \times 3 \times 3$ | 8.317 | -9.31 | 4.096 | -9.20 |
| $4 \times 4 \times 4$ | 6.803 | -25.82 | 3.346 | -25.84 |
| $5 \times 5 \times 5$ | 8.981 | -2.08 | 4.419 | -2.05 |
| $6 \times 6 \times 6$ | 7.888 | -13.99 | 3.880 | -13.99 |
| $7 \times 7 \times 7$ | 8.807 | -3.98 | 4.334 | -3.95 |
| $8 \times 8 \times 8$ | 8.209 | -10.49 | 4.038 | -10.50 |
| $9 \times 9 \times 9$ | 9.171 | 0.00 | 4.512 | 0.00 |
| $10 \times 10 \times 10$ | 8.262 | -9.91 | 4.063 | -9.94 |
| $11 \times 11 \times 11$ | 9.003 | -1.84 | 4.428 | -1.85 |

**Table S1.8** Calculated lattice thermal conductivity $\kappa_{latt}$ at $T = 300$ and 600 K for ArCo$_8$Sb$_{32}$ obtained with the series of Brillouin-zone sampling meshes shown in Fig. 1.16.

| Sampling Mesh | $T = 300$ K | | $T = 600$ K | |
|---|---|---|---|---|
| | $\kappa_{latt}$ [W m$^{-1}$ K$^{-1}$] | $\Delta$ [%] | $\kappa_{latt}$ [W m$^{-1}$ K$^{-1}$] | $\Delta$ [%] |
| $2 \times 2 \times 2$ | 0.000 | -100.00 | 0.000 | -100.00 |
| $3 \times 3 \times 3$ | 7.847 | -10.51 | 3.865 | -10.36 |
| $4 \times 4 \times 4$ | 6.324 | -27.87 | 3.110 | -27.86 |
| $5 \times 5 \times 5$ | 8.330 | -5.00 | 4.097 | -4.99 |
| $6 \times 6 \times 6$ | 7.787 | -11.19 | 3.830 | -11.17 |
| $7 \times 7 \times 7$ | 8.360 | -4.66 | 4.113 | -4.61 |
| $8 \times 8 \times 8$ | 7.924 | -9.63 | 3.896 | -9.64 |
| $9 \times 9 \times 9$ | 8.768 | 0.00 | 4.312 | 0.00 |
| $10 \times 10 \times 10$ | 7.929 | -9.57 | 3.898 | -9.60 |
| $11 \times 11 \times 11$ | 8.531 | -2.70 | 4.194 | -2.72 |

**Table S1.9** Calculated lattice thermal conductivity $\kappa_{latt}$ at $T = 300$ and 600 K for KrCo$_8$Sb$_{32}$ obtained with the series of Brillouin-zone sampling meshes shown in Fig. 1.17.

| Sampling Mesh | $T = 300$ K | | $T = 600$ K | |
|---|---|---|---|---|
| | $\kappa_{latt}$ [W m$^{-1}$ K$^{-1}$] | $\Delta$ [%] | $\kappa_{latt}$ [W m$^{-1}$ K$^{-1}$] | $\Delta$ [%] |
| $2 \times 2 \times 2$ | 0.000 | -100.00 | 0.000 | -100.00 |
| $3 \times 3 \times 3$ | 7.588 | -10.67 | 3.738 | -10.55 |
| $4 \times 4 \times 4$ | 6.332 | -25.46 | 3.114 | -25.48 |
| $5 \times 5 \times 5$ | 8.005 | -5.76 | 3.939 | -5.75 |
| $6 \times 6 \times 6$ | 7.586 | -10.70 | 3.732 | -10.69 |
| $7 \times 7 \times 7$ | 8.087 | -4.80 | 3.980 | -4.76 |
| $8 \times 8 \times 8$ | 7.813 | -8.03 | 3.843 | -8.04 |
| $9 \times 9 \times 9$ | 8.494 | 0.00 | 4.179 | 0.00 |
| $10 \times 10 \times 10$ | 7.766 | -8.58 | 3.820 | -8.60 |
| $11 \times 11 \times 11$ | 8.356 | -1.63 | 4.110 | -1.64 |

**Table S1.10** Calculated lattice thermal conductivity $\kappa_{latt}$ at $T = 300$ and 600 K for XeCo$_8$Sb$_{32}$ obtained with the series of Brillouin-zone sampling meshes shown in Fig. 1.18.
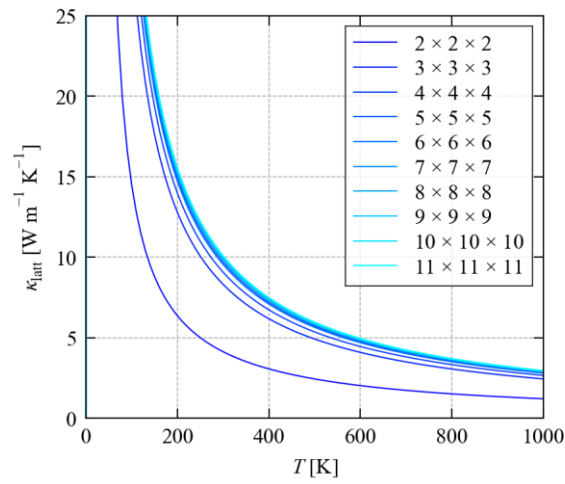


**Figure S1.11** Lattice thermal-conductivity $\kappa_{latt}$ of pristine CoSb$_3$ calculated with a series of Brillouin-zone sampling meshes (conventional cell model).
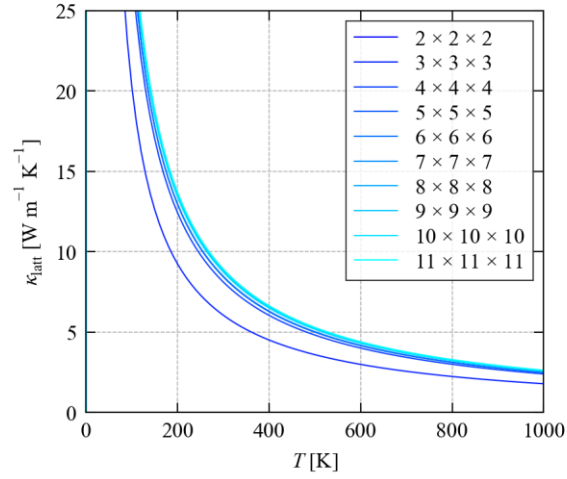
**Figure S1.12** Lattice thermal-conductivity $\kappa_{latt}$ of pristine CoSb$_3$ calculated with a series of Brillouin-zone sampling meshes (primitive cell model with 2$^{nd}$-order IFCs computed using a $2 \times 2 \times 2$ supercell expansion and 3$^{rd}$-order IFCs evaluated in the base cell).
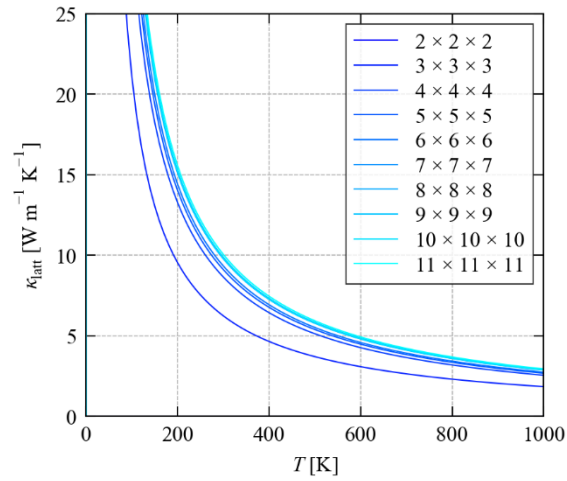


**Figure S1.13** Lattice thermal-conductivity $\kappa_{latt}$ of pristine CoSb$_3$ calculated with a series of Brillouin-zone sampling meshes (primitive cell model with 2$^{nd}$- and 3$^{rd}$-order IFCs computed using a $2 \times 2 \times 2$ supercell expansion).
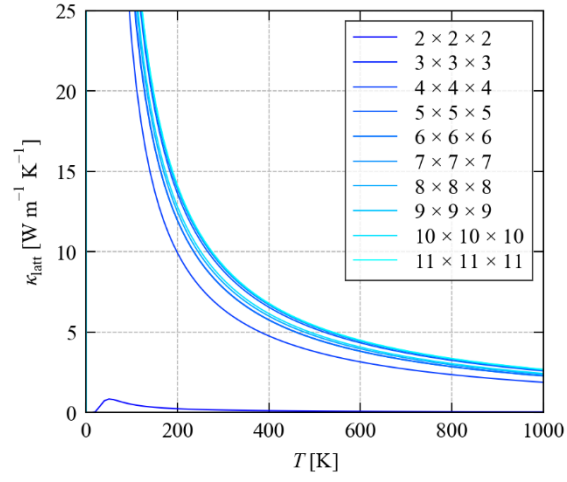
**Figure S1.14** Lattice thermal-conductivity $\kappa_{latt}$ of HeCo$_8$Sb$_{24}$ calculated with a series of Brillouin-zone sampling meshes.
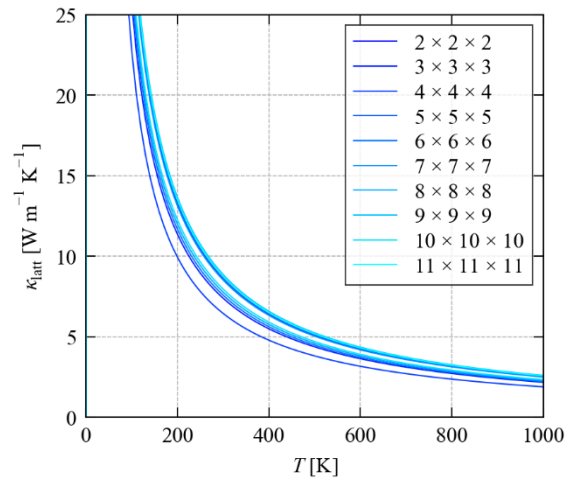


**Figure S1.15** Lattice thermal-conductivity $\kappa_{latt}$ of NeCo$_8$Sb$_{24}$ calculated with a series of Brillouin-zone sampling meshes.
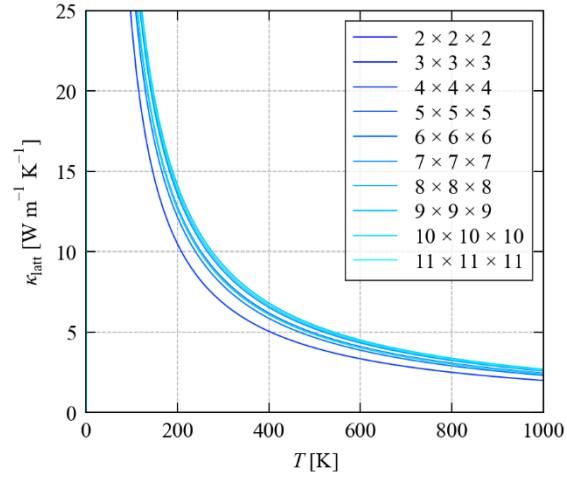
**Figure S1.16** Lattice thermal-conductivity $\kappa_{\text{latt}}$ of ArCo$_8$Sb$_{24}$ calculated with a series of Brillouin-zone sampling meshes.
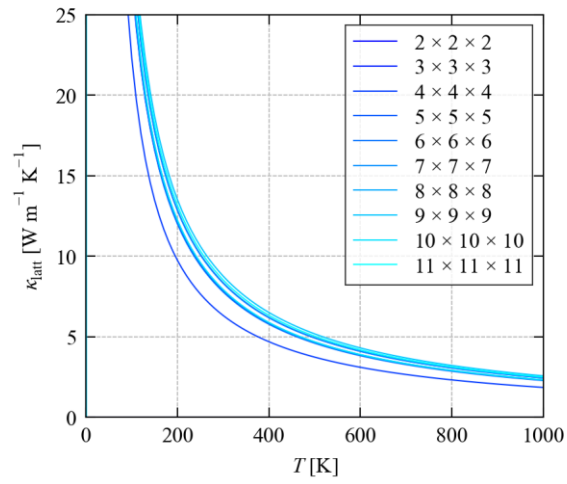


**Figure S1.17** Lattice thermal-conductivity $\kappa_{\text{latt}}$ of KrCo$_8$Sb$_{24}$ calculated with a series of Brillouin-zone sampling meshes.
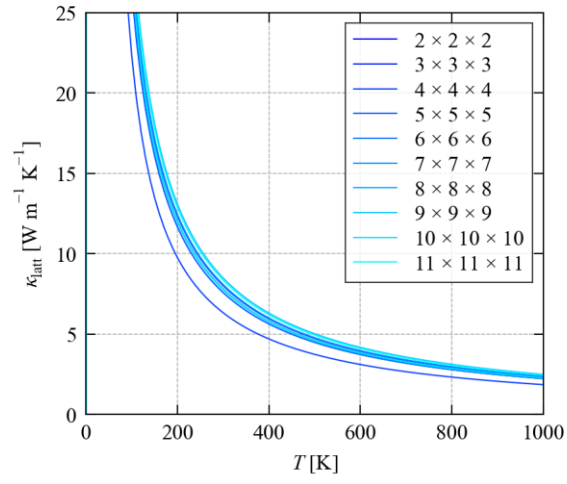
**Figure S1.18** Lattice thermal-conductivity $\kappa_{latt}$ of $XeCo_8Sb_{24}$ calculated with a series of Brillouin-zone sampling meshes.

## 3. Results and Discussion
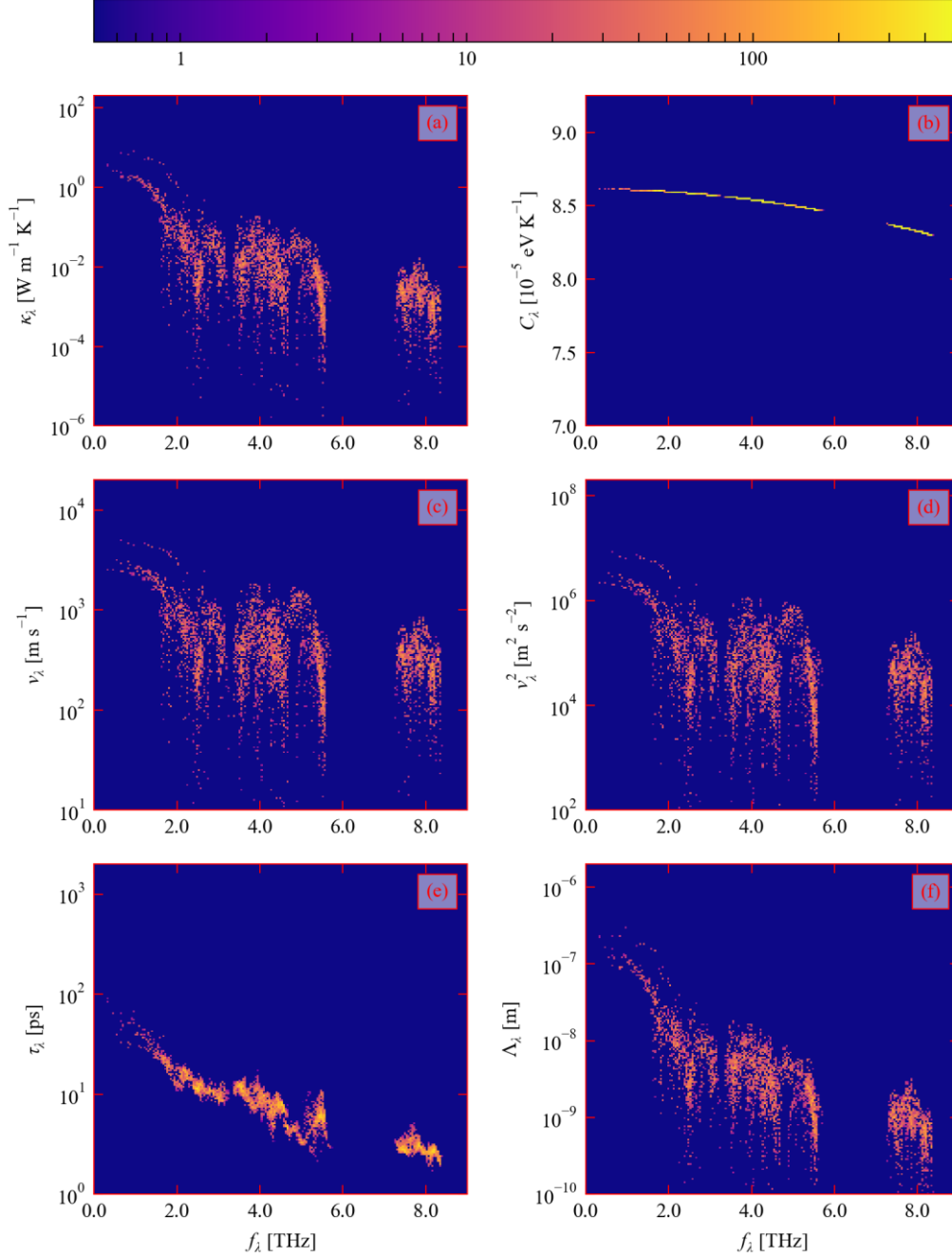
*a. Pristine CoSb₃*



**Figure S2.1** Frequency spectra of the modal terms in Eq. 2 in the text for pristine CoSb₃ at $T = 600$ K, *viz.* the thermal conductivities $\kappa_\lambda$ (a), heat capacities $C_\lambda$ (b), group velocities $v_\lambda$ (c) and outer products $v_\lambda^2$ (d), and the lifetimes $\tau_\lambda$ (e), together with the mean-free paths $\Lambda_\lambda = v_\lambda \tau_\lambda$ (f). Note that quantities in (a) and (c)-(f) are shown on a logarithmic scale, while the $C_\lambda$ in (b) are shown on a linear scale. The y-axis limits are set to the same as Fig. 5 in the text for easy comparison between the two sets of data.

*b. CoSb₃ with noble gas fillers*

| | $a_0$ [Å] | | |
|---|---|---|---|
| | PBesol | PBEsol + D3 | Δ [%] |
| CoSb₃ | 8.952 | 8.885 | -0.75 |
| HeCo₈Sb₂₄ | 8.952 | 8.886 | -0.73 |
| NeCo₈Sb₂₄ | 8.960 | 8.892 | -0.76 |
| ArCo₈Sb₂₄ | 8.975 | 8.909 | -0.74 |
| KrCo₈Sb₂₄ | 8.987 | 8.922 | -0.73 |
| XeCo₈Sb₂₄ | 9.010 | 8.943 | -0.74 |

**Table S2.1** Optimise lattice constants of pristine CoSb₃ and filled XCo₈Sb₂₄ with X = He, Ne, Ar, Kr and Xe obtained with the PBEsol functional with and without the DFT-D3 dispersion correction. The right-hand column shows the % differences for comparison.

| | NN 1 - 12 Sb | | NN 2 - 8 Co | | NN 3 - 24 Sb | |
|---|---|---|---|---|---|---|
| | $d$ [Å] | $\|\Phi\|$ [eV Å⁻²] | $d$ [Å] | $\|\Phi\|$ [eV Å⁻²] | $d$ [Å] | $\|\Phi\|$ [eV Å⁻²] |
| HeCo₈Sb₂₄ | 3.312 | $1.70 \times 10^{-1}$ | 3.875 | $1.78 \times 10^{-2}$ | 5.615 | $4.66 \times 10^{-3}$ |
| NeCo₈Sb₂₄ | 3.320 | $3.38 \times 10^{-1}$ | 3.880 | $1.54 \times 10^{-2}$ | 5.621 | $6.67 \times 10^{-3}$ |
| ArCo₈Sb₂₄ | 3.342 | $8.50 \times 10^{-1}$ | 3.890 | $9.94 \times 10^{-2}$ | 5.631 | $2.07 \times 10^{-2}$ |
| KrCo₈Sb₂₄ | 3.355 | 1.15 | 3.897 | $1.53 \times 10^{-1}$ | 5.639 | $3.01 \times 10^{-2}$ |
| XeCo₈Sb₂₄ | 3.377 | 1.63 | 3.911 | $2.32 \times 10^{-1}$ | 5.655 | $4.88 \times 10^{-2}$ |

**Table S2.2** Neighbour distances $d$ between the filler atom X and the three nearest neighbours in XCo₈Sb₂₄ (X = He, Ne, Ar, Kr and Xe), together with the Frobenius norms $\|\Phi\|$ of the corresponding second-order (harmonic) force constants (see Eq. 5 in the text).

| | $\bar{\kappa}_{latt}$ [W m$^{-1}$ K$^{-1}$] | $\Delta$ [%] | $\bar{\kappa}_{latt}/\tau^{CRTA}$ [10$^{12}$ W m$^{-1}$ K$^{-1}$ s$^{-1}$] | $\Delta$ [%] | $\tau^{CRTA}$ [ps] | $\Delta$ [%] | $\tilde{P}$ [10$^{-12}$ eV$^2$] | $\Delta$ [%] | $\bar{\tau}_\lambda$ [ps] | $\bar{P}_\lambda$ [10$^{-12}$ eV$^2$] |
|---|---|---|---|---|---|---|---|---|---|---|
| CoSb$_3$ | 4.91 | - | 0.278 | - | 17.6 | - | 0.399 | - | 8.31 | 6.00 |
| HeCo$_8$Sb$_{24}$ | 4.48 | -8.82 | 0.265 | -4.64 | 16.9 | -4.38 | 0.404 | 1.30 | 8.06 | 5.65 |
| NeCo$_8$Sb$_{24}$ | 4.36 | -11.18 | 0.248 | -10.83 | 17.6 | -0.39 | 0.393 | -1.53 | 8.14 | 5.46 |
| ArCo$_8$Sb$_{24}$ | 4.51 | -8.09 | 0.254 | -8.81 | 17.8 | 0.79 | 0.395 | -0.90 | 7.98 | 5.35 |
| KrCo$_8$Sb$_{24}$ | 4.31 | -12.17 | 0.242 | -13.02 | 17.8 | 0.98 | 0.391 | -1.88 | 8.01 | 5.27 |
| XeCo$_8$Sb$_{24}$ | 4.18 | -14.87 | 0.243 | -12.71 | 17.2 | -2.47 | 0.389 | -2.31 | 7.72 | 5.18 |

**Table S2.3** Calculated lattice thermal conductivity $\kappa_{latt}$, $\kappa_{latt}/\tau^{CRTA}$, $\tau^{CRTA}$ and $\tilde{P}$ at $T$ = 600 K for the CoSb$_3$ and XCo$_8$Sb$_{24}$ (X = He, Ne, Ar, Kr) models examined in this work. The quantities $\kappa_{latt}/\tau^{CRTA}$, $\tau^{CRTA}$ and $\tilde{P}$ are defined in the text. The percentage change in the parameters relative to pristine CoSb$_3$ are shown for comparison. The rightmost two columns list the averaged lifetimes and interaction strengths $\bar{\tau}_\lambda/\bar{P}_\lambda$ for comparison to the $\tau^{CRTA}$ and $\tilde{P}$ respectively.
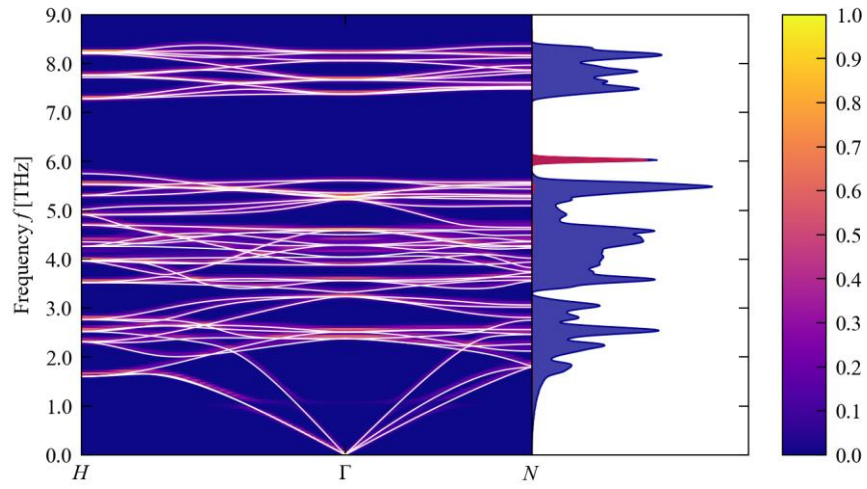
**Figure S2.2** Unfolded band dispersion and phonon density of states $g(f)$ (DoS) of HeCo$_8$Sb$_{24}$. The colour scale shows the spectral weights obtained from the band-unfolding procedure. The band structure of pristine CoSb$_3$ is overlaid on the dispersion in white, and the projection of the DoS onto the He filler is overlaid on the $g(f)$ in red.
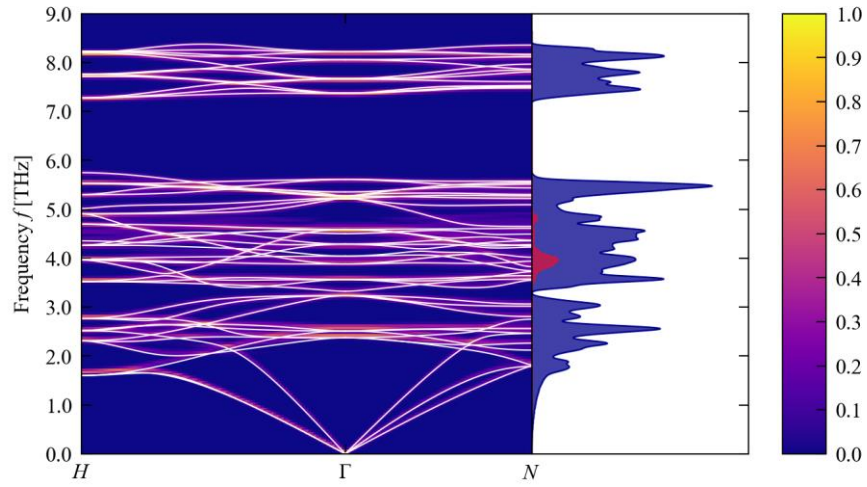


**Figure S2.3** Unfolded band dispersion and phonon density of states $g(f)$ (DoS) of NeCo$_8$Sb$_{24}$. The colour scale shows the spectral weights obtained from the band-unfolding procedure. The band structure of pristine CoSb$_3$ is overlaid on the dispersion in white, and the projection of the DoS onto the Ne filler is overlaid on the $g(f)$ in red.
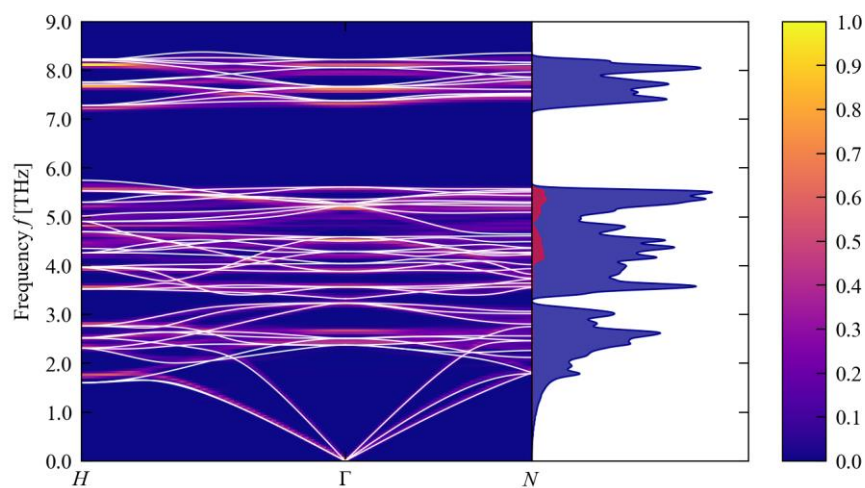
**Figure S2.4** Unfolded band dispersion and phonon density of states $g(f)$ (DoS) of $ArCo_8Sb_{24}$. The colour scale shows the spectral weights obtained from the band-unfolding procedure. The band structure of pristine $CoSb_3$ is overlaid on the dispersion in white, and the projection of the DoS onto the Ar filler is overlaid on the $g(f)$ in red.
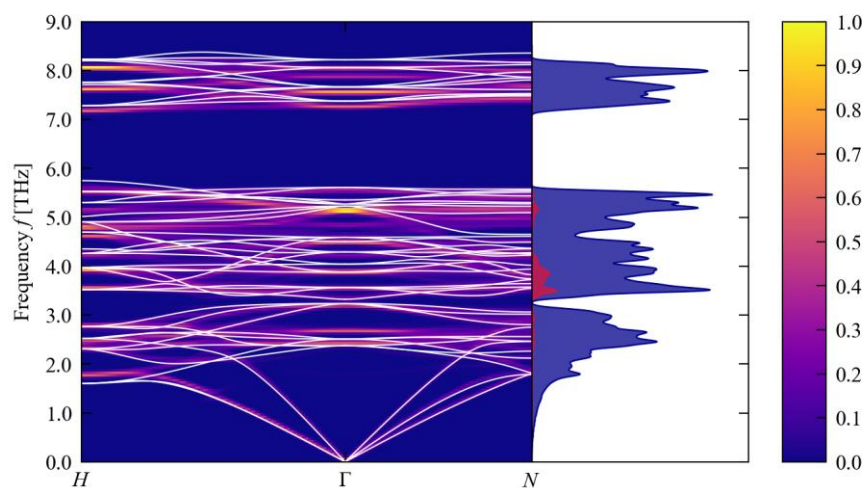


**Figure S2.5** Unfolded band dispersion and phonon density of states $g(f)$ (DoS) of $KrCo_8Sb_{24}$. The colour scale shows the spectral weights obtained from the band-unfolding procedure. The band structure of pristine $CoSb_3$ is overlaid on the dispersion in white, and the projection of the DoS onto the Kr filler is overlaid on the $g(f)$ in red.
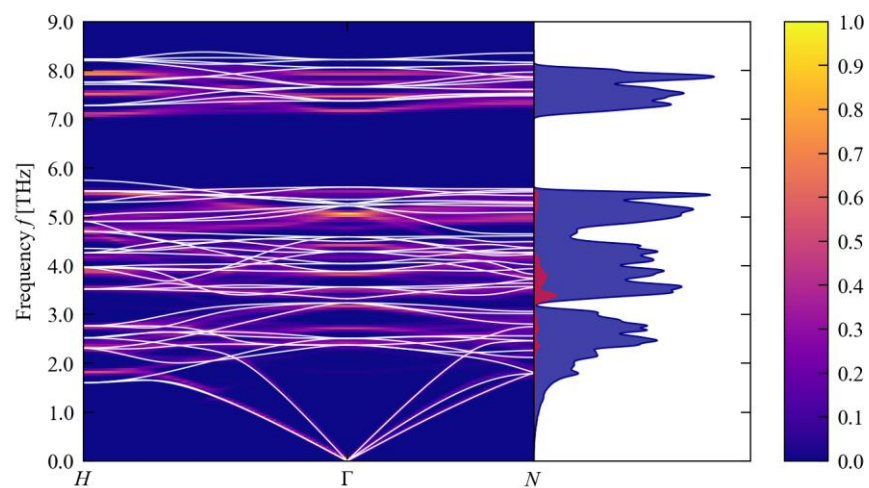
**Figure S2.6** Unfolded band dispersion and phonon density of states $g(f)$ (DoS) of $XeCo_8Sb_{24}$. The colour scale shows the spectral weights obtained from the band-unfolding procedure. The band structure of pristine $CoSb_3$ is overlaid on the dispersion in white, and the projection of the DoS onto the Xe filler is overlaid on the $g(f)$ in red.
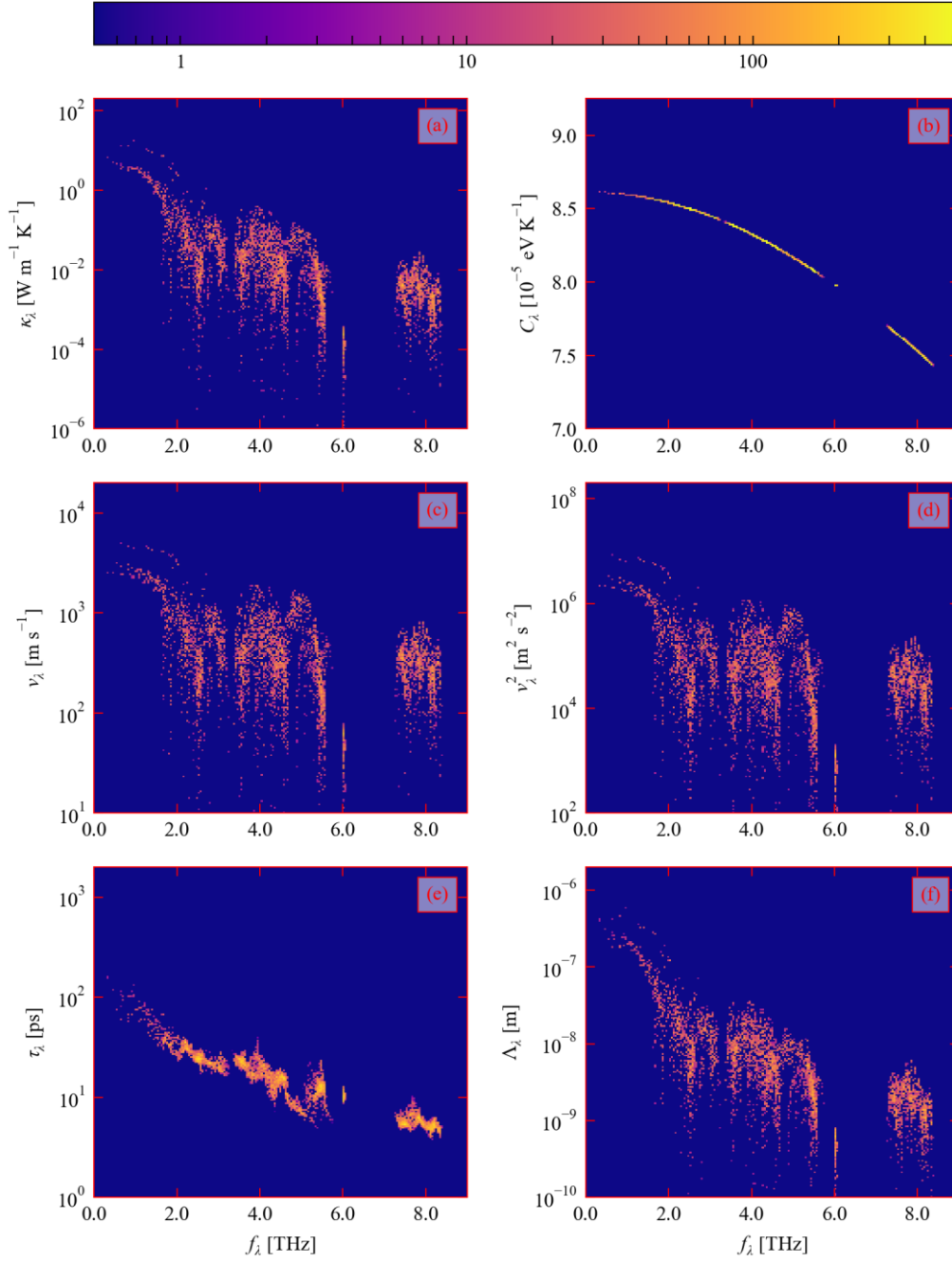
**Figure S2.7** Frequency spectra of the modal terms in Eq. 2 in the text for HeCo$_8$Sb$_{24}$ at $T$ = 300 K, *viz.* the thermal conductivities $\kappa_\lambda$ (a), heat capacities $C_\lambda$ (b), group velocities $v_\lambda$ (c) and outer products $v_\lambda^2$ (d), and the lifetimes $\tau_\lambda$ (e), together with the mean-free paths $\Lambda_\lambda = v_\lambda \tau_\lambda$ (f). Note that quantities in (a) and (c)-(f) are shown on a logarithmic scale, while the $C_\lambda$ in (b) are shown on a linear scale.
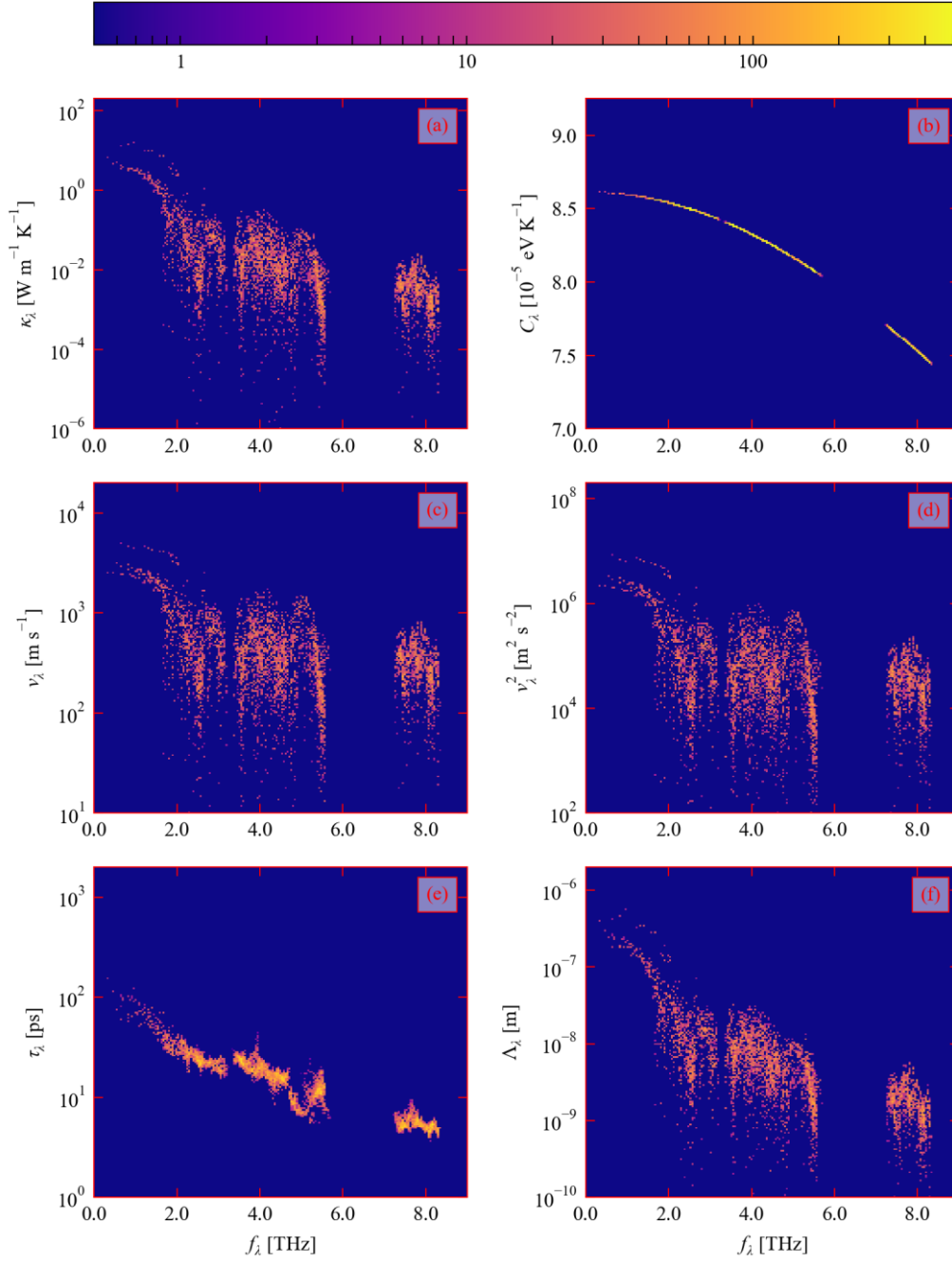
**Figure S2.8** Frequency spectra of the modal terms in Eq. 2 in the text for NeCo$_8$Sb$_{24}$ at $T = 300$ K, *viz.* the thermal conductivities $v_\lambda$ (a), heat capacities $C_\lambda$ (b), group velocities $\kappa_\lambda$ (c) and outer products $v_\lambda^2$ (d), and the lifetimes $\tau_\lambda$ (e), together with the mean-free paths $\Lambda_\lambda = v_\lambda \tau_\lambda$ (f). Note that quantities in (a) and (c)-(f) are shown on a logarithmic scale, while the $C_\lambda$ in (b) are shown on a linear scale.
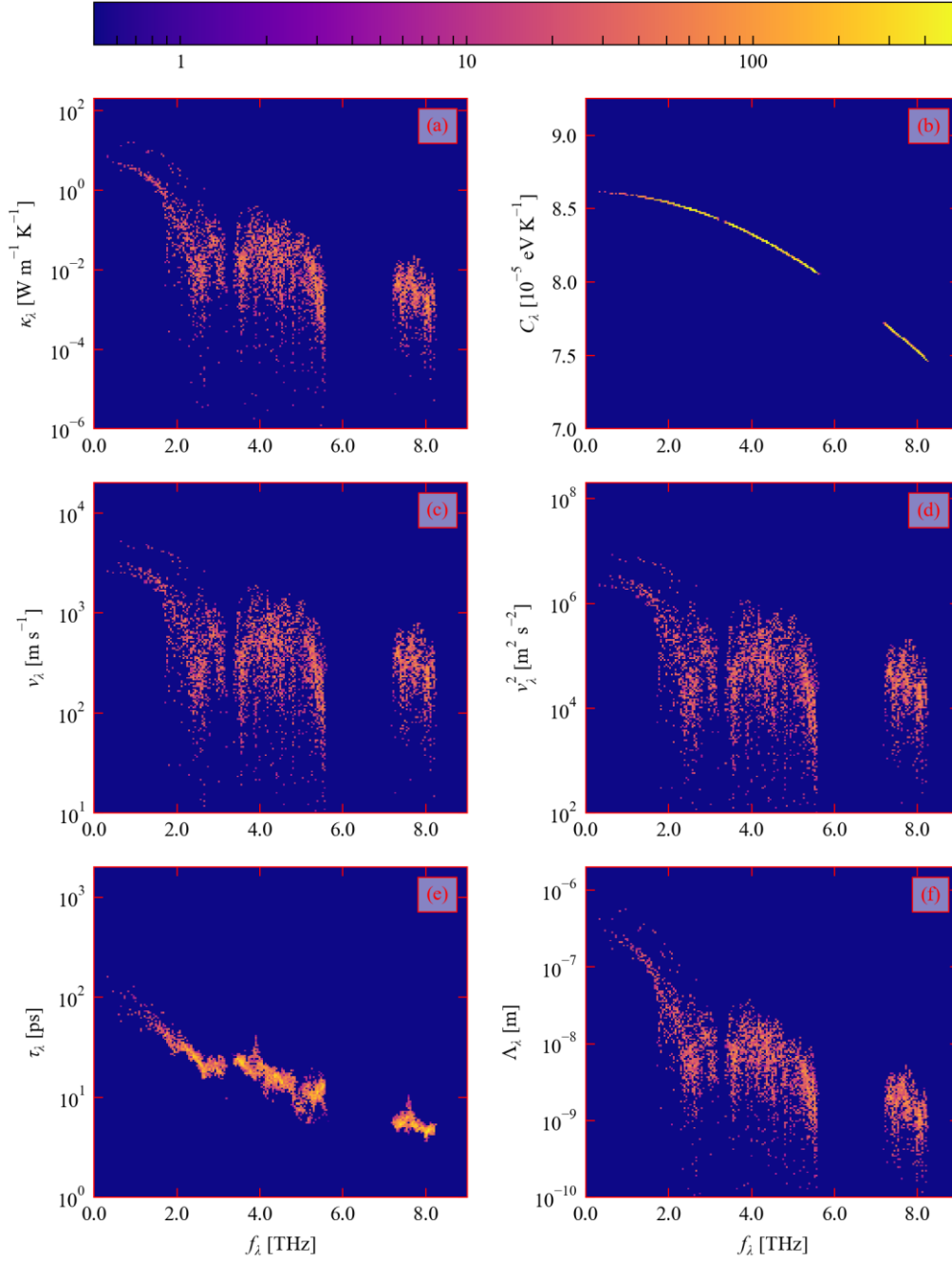
**Figure S2.9** Frequency spectra of the modal terms in Eq. 2 in the text for ArCo$_8$Sb$_{24}$ at $T = 300$ K, *viz.* the thermal conductivities $\kappa_\lambda$ (a), heat capacities $C_\lambda$ (b), group velocities $v_\lambda$ (c) and outer products $v_\lambda^2$ (d), and the lifetimes $\tau_\lambda$ (e), together with the mean-free paths $\Lambda_\lambda = v_\lambda \tau_\lambda$ (f). Note that quantities in (a) and (c)-(f) are shown on a logarithmic scale, while the $C_\lambda$ in (b) are shown on a linear scale.
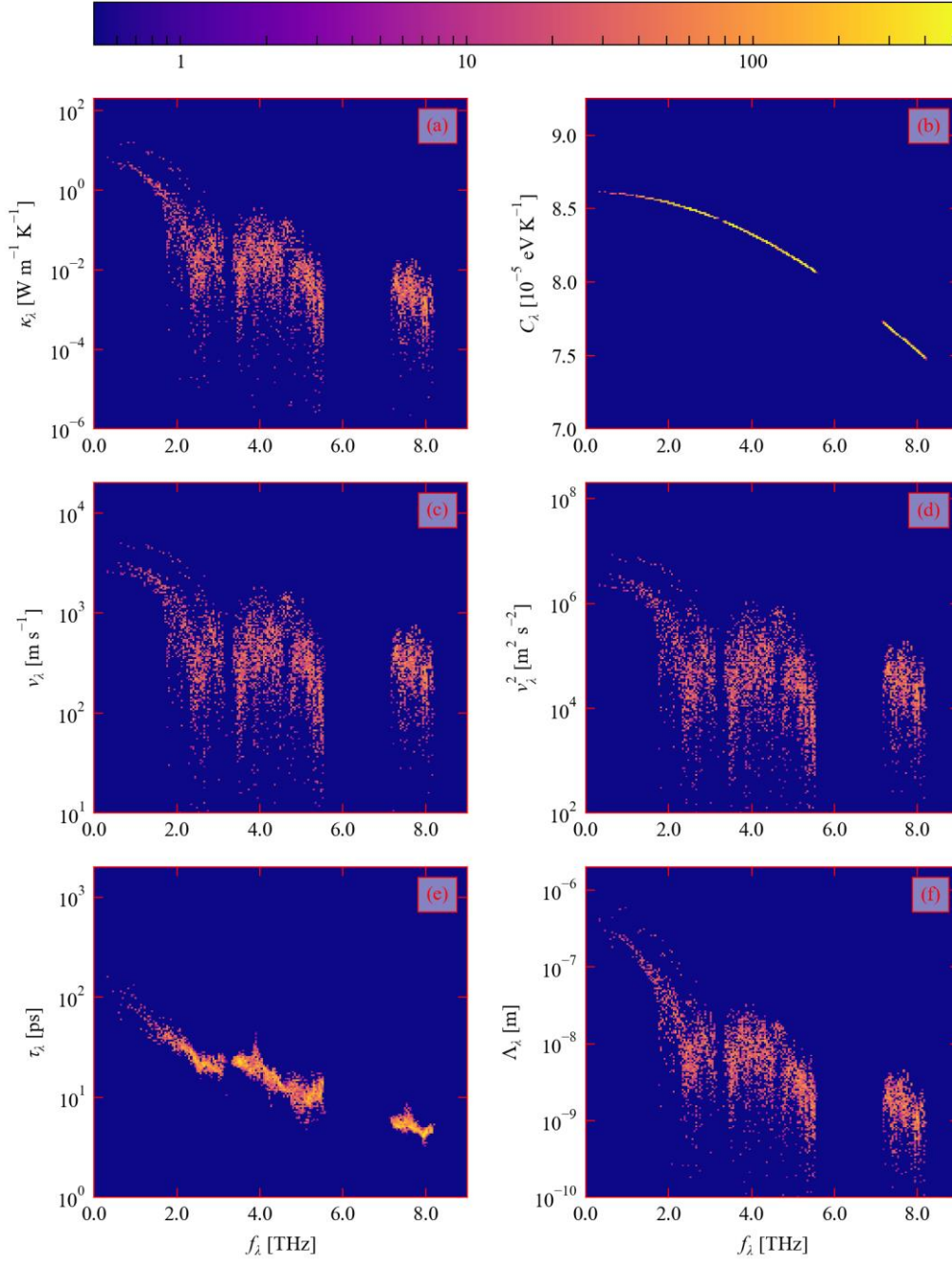
**Figure S2.10** Frequency spectra of the modal terms in Eq. 2 in the text for $KrCo_8Sb_{24}$ at $T = 300$ K, *viz.* the thermal conductivities $\kappa_\lambda$ (a), heat capacities $C_\lambda$ (b), group velocities $v_\lambda$ (c) and outer products $v_\lambda^2$ (d), and the lifetimes $\tau_\lambda$ (e), together with the mean-free paths $\Lambda_\lambda = v_\lambda \tau_\lambda$ (f). Note that quantities in (a) and (c)-(f) are shown on a logarithmic scale, while the $C_\lambda$ in (b) are shown on a linear scale.
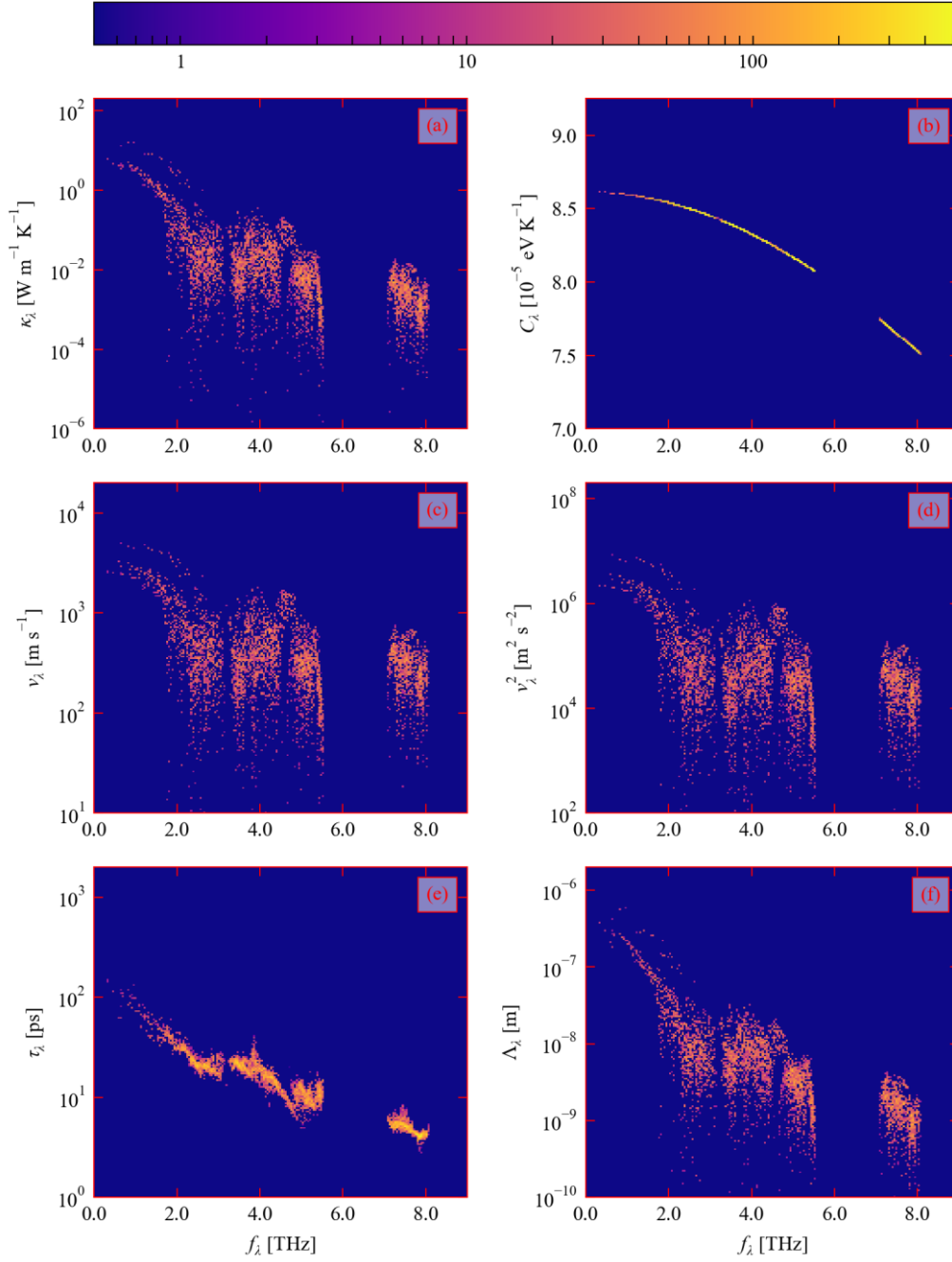
**Figure S2.11** Frequency spectra of the modal terms in Eq. 2 in the text for XeCo$_8$Sb$_{24}$ at $T$ = 300 K, *viz.* the thermal conductivities $\kappa_\lambda$ (a), heat capacities $C_\lambda$ (b), group velocities $v_\lambda$ (c) and outer products $v_\lambda^2$ (d), and the lifetimes $\tau_\lambda$ (e), together with the mean-free paths $\Lambda_\lambda = v_\lambda \tau_\lambda$ (f). Note that quantities in (a) and (c)-(f) are shown on a logarithmic scale, while the $C_\lambda$ in (b) are shown on a linear scale.
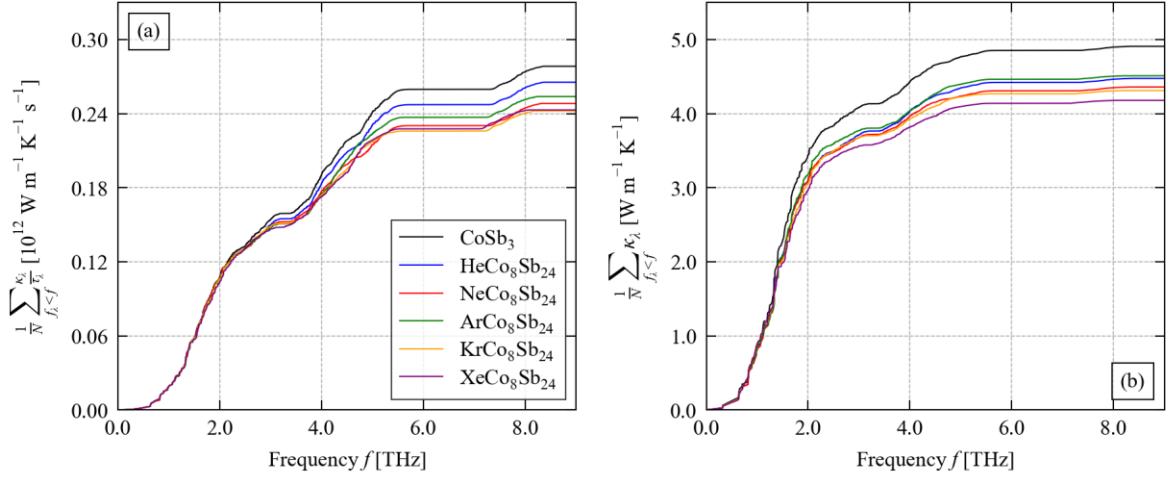
**Figure S2.12** Accumulation of the $\kappa_\lambda/\tau_\lambda$ (a) and $\kappa_\lambda$ (b) as a function of frequency at $T = 600$ K for pristine $CoSb_3$ and filled $XCo_8Sb_{24}$ models with X = He, Ne, Ar, Kr and Xe.
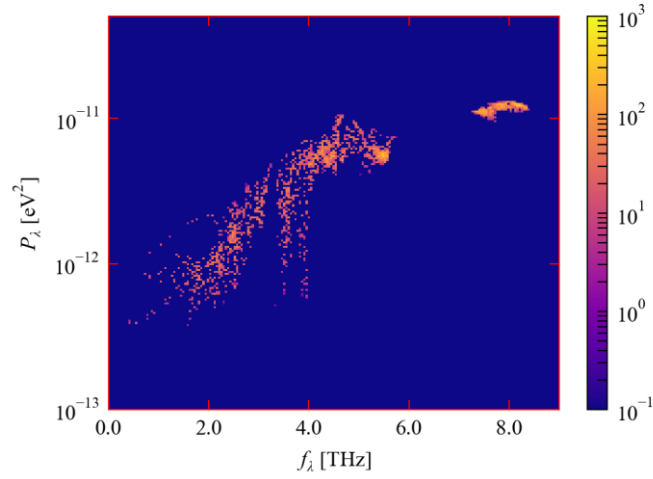


**Figure S2.13** Frequency spectra of the averaged modal three-phonon interaction strengths $P_\lambda$ of $CoSb_3$ as defined in Eq. 12 in the text.
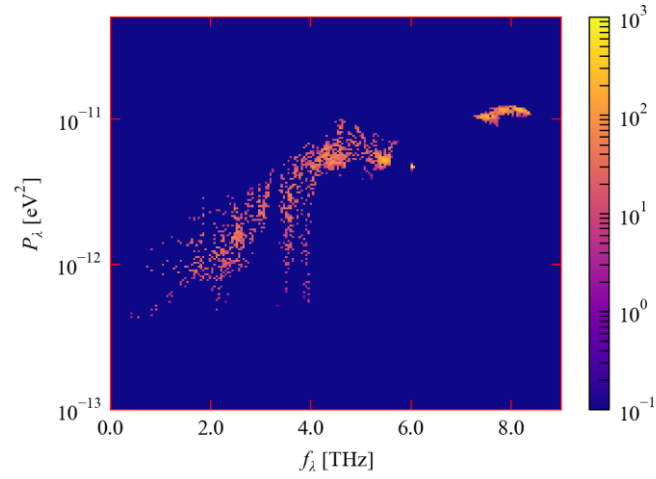
**Figure S2.14** Frequency spectra of the averaged modal three-phonon interaction strengths $P_\lambda$ of $HeCo_8Sb_{24}$ as defined in Eq. 12 in the text.
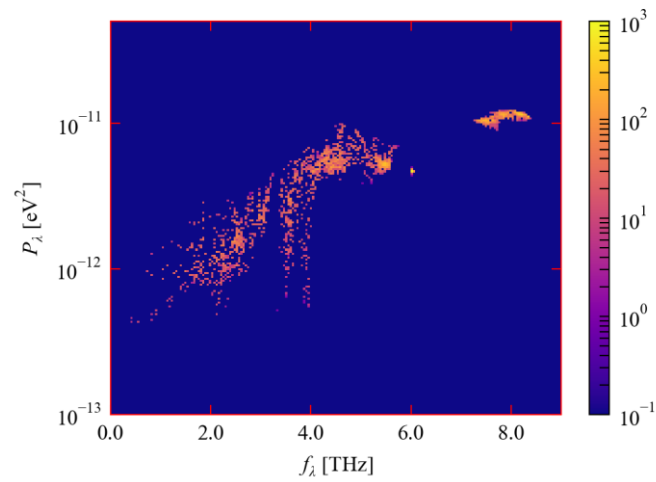


**Figure S2.15** Frequency spectra of the averaged modal three-phonon interaction strengths $P_\lambda$ of $NeCo_8Sb_{24}$ as defined in Eq. 12 in the text.
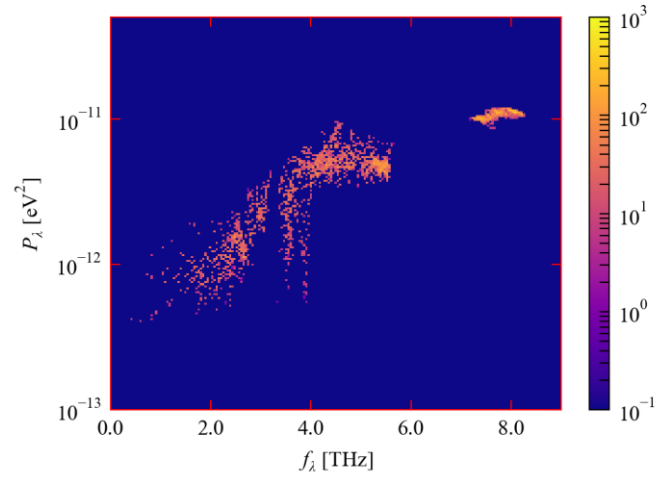
**Figure S2.16** Frequency spectra of the averaged modal three-phonon interaction strengths $P_\lambda$ of ArCo$_8$Sb$_{24}$ as defined in Eq. 12 in the text.
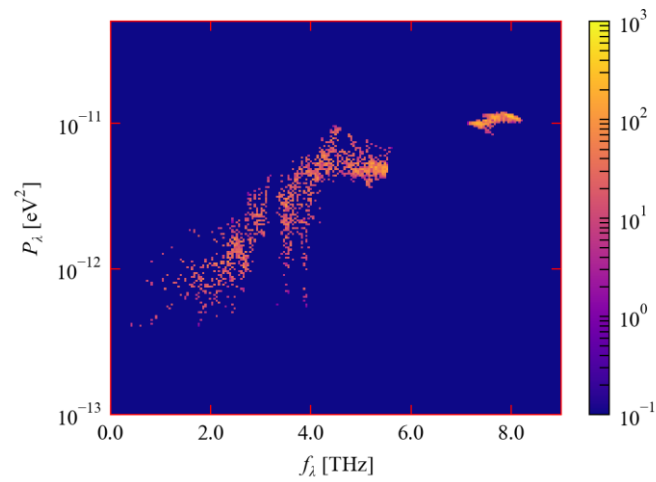


**Figure S2.17** Frequency spectra of the averaged modal three-phonon interaction strengths $P_\lambda$ of KrCo$_8$Sb$_{24}$ as defined in Eq. 12 in the text.
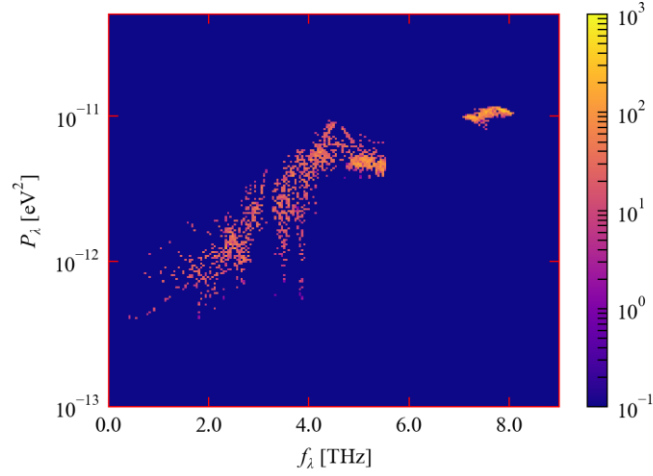
**Figure S2.18** Frequency spectra of the averaged modal three-phonon interaction strengths $P_\lambda$ of $XeCo_8Sb_{24}$ as defined in Eq. 12 in the text.
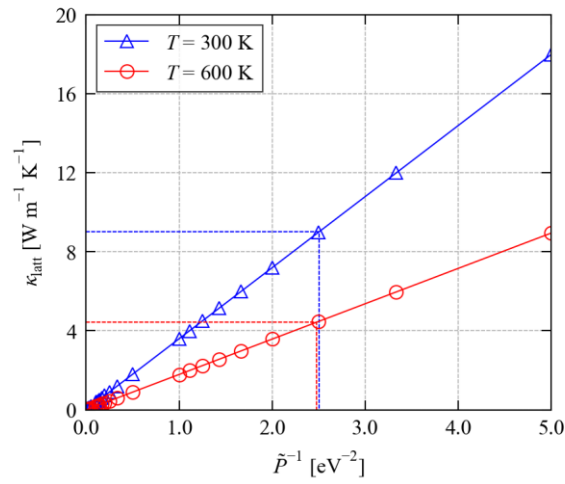


**Figure S2.19** Dependence of the $\kappa_{latt}$ of $HeCo_8Sb_{24}$ on the averaged three-phonon interaction strength $\tilde{P}$ defined in the text at $T = 300$ and 600 K (blue/red). The dashed lines mark the $\tilde{P}$ that recover the calculated $\kappa_{latt}$ at the two temperatures.
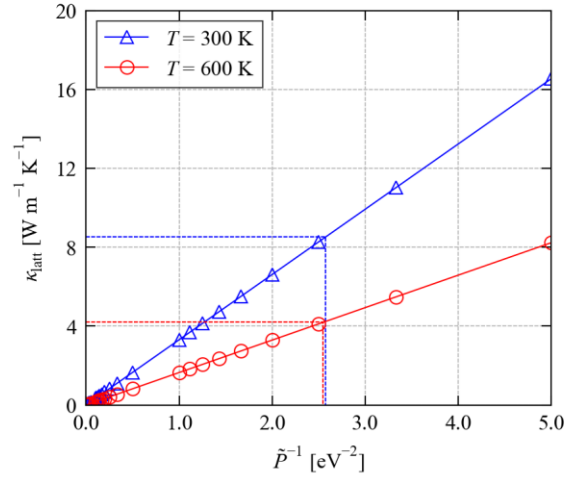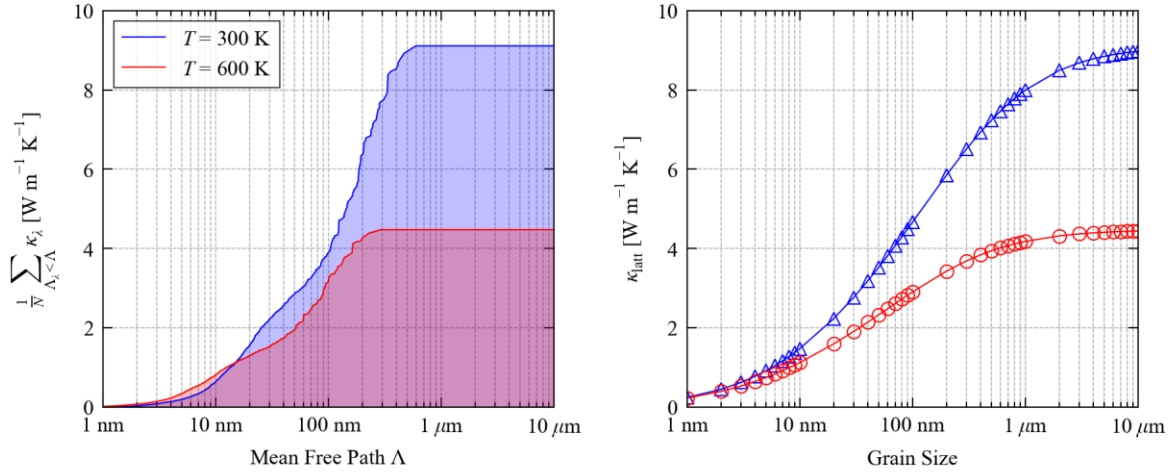
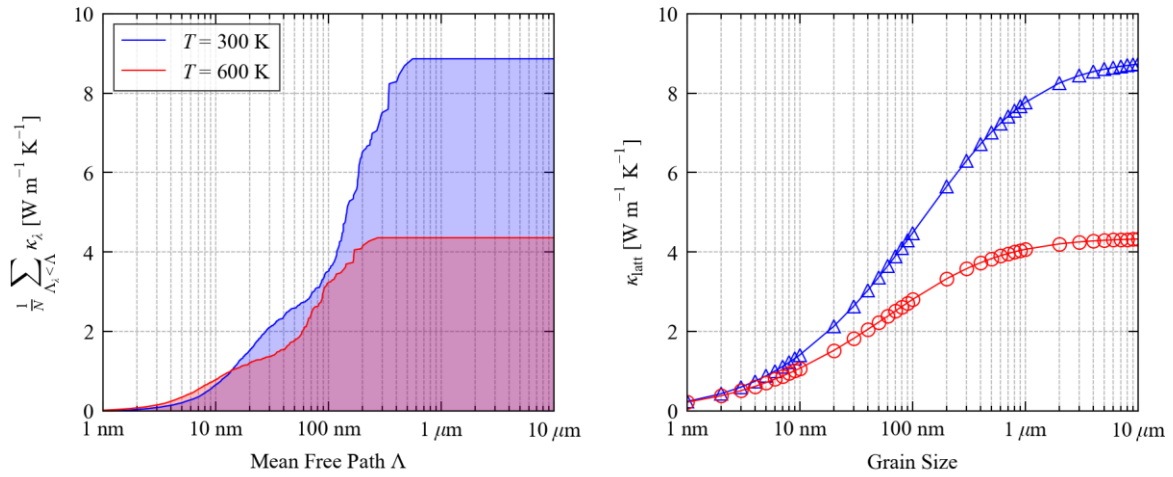**Figure S2.20** Dependence of the $\kappa_{\mathrm{latt}}$ of NeCo$_8$Sb$_{24}$ on the averaged three-phonon interaction strength $\tilde{P}$ defined in the text at $T = 300$ and 600 K (blue/red). The dashed lines mark the $\tilde{P}$ that recover the calculated $\kappa_{\mathrm{latt}}$ at the two temperatures.
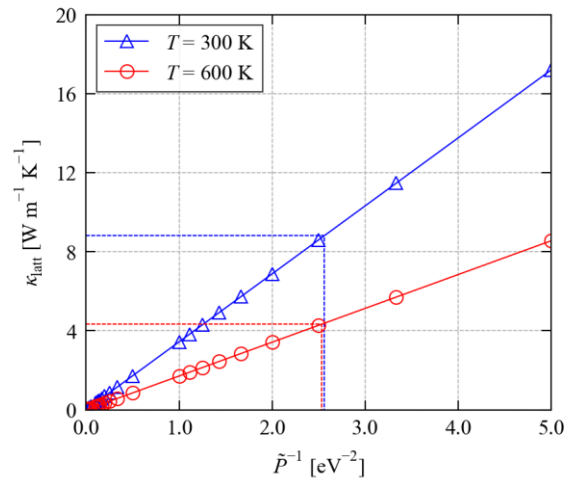


**Figure S2.21** Dependence of the $\kappa_{\mathrm{latt}}$ of ArCo$_8$Sb$_{24}$ on the averaged three-phonon interaction strength $\tilde{P}$ defined in the text at $T = 300$ and 600 K (blue/red). The dashed lines mark the $\tilde{P}$ that recover the calculated $\kappa_{\mathrm{latt}}$ at the two temperatures.
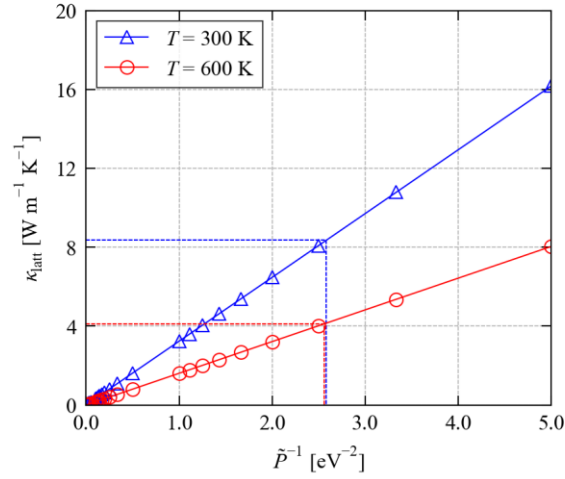
**Figure S2.22** Dependence of the $\kappa_{\text{latt}}$ of KrCo$_8$Sb$_{24}$ on the averaged three-phonon interaction strength $\tilde{P}$ defined in the text at $T = 300$ and 600 K (blue/red). The dashed lines mark the $\tilde{P}$ that recover the calculated $\kappa_{\text{latt}}$ at the two temperatures.
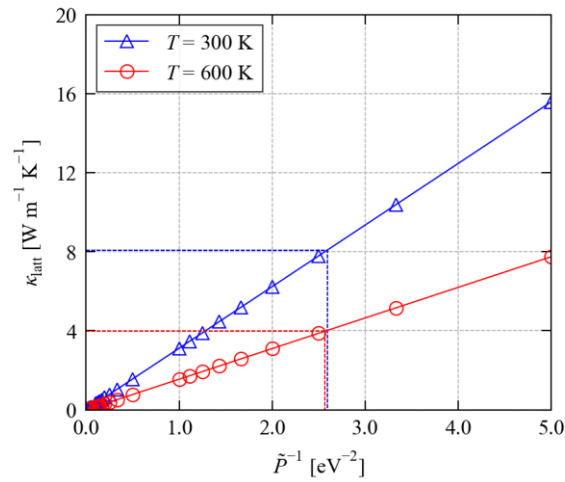


**Figure S2.23** Dependence of the $\kappa_{\text{latt}}$ of XeCo$_8$Sb$_{24}$ on the averaged three-phonon interaction strength $\tilde{P}$ defined in the text at $T = 300$ and 600 K (blue/red). The dashed lines mark the $\tilde{P}$ that recover the calculated $\kappa_{\text{latt}}$ at the two temperatures.
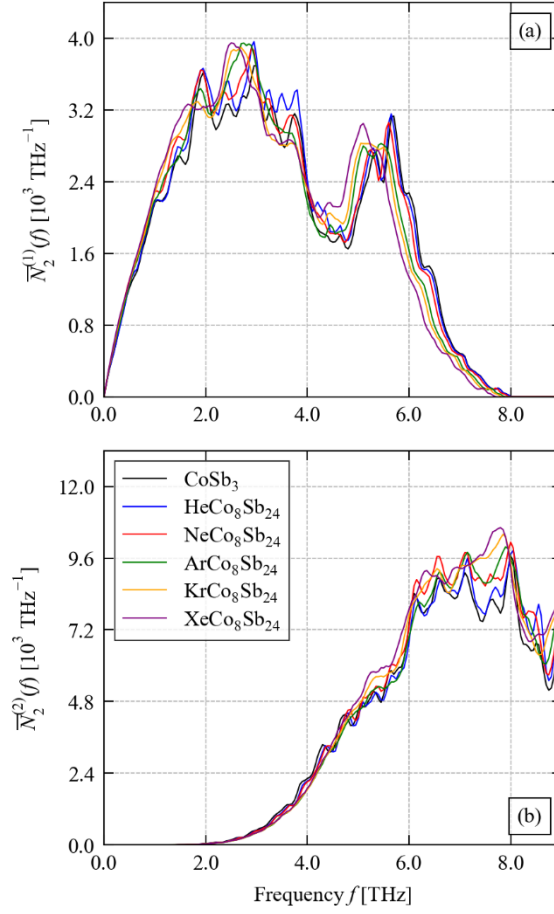
**Figure S2.24** Averaged weighted two-phonon joint density of states (w-JDoS) functions $\bar{N}_2^{(1)}(\omega)$ (a) and $\bar{N}_2^{(2)}(\omega)$ (b) for collision and decay processes, respectively, for $CoSb_3$ and $XCo_8Sb_{24}$ with X = He, Ne, Ar, Kr and Xe at $T = 600$ K. The two w-JDoS functions are defined in Eqs. 14-17 in the text.
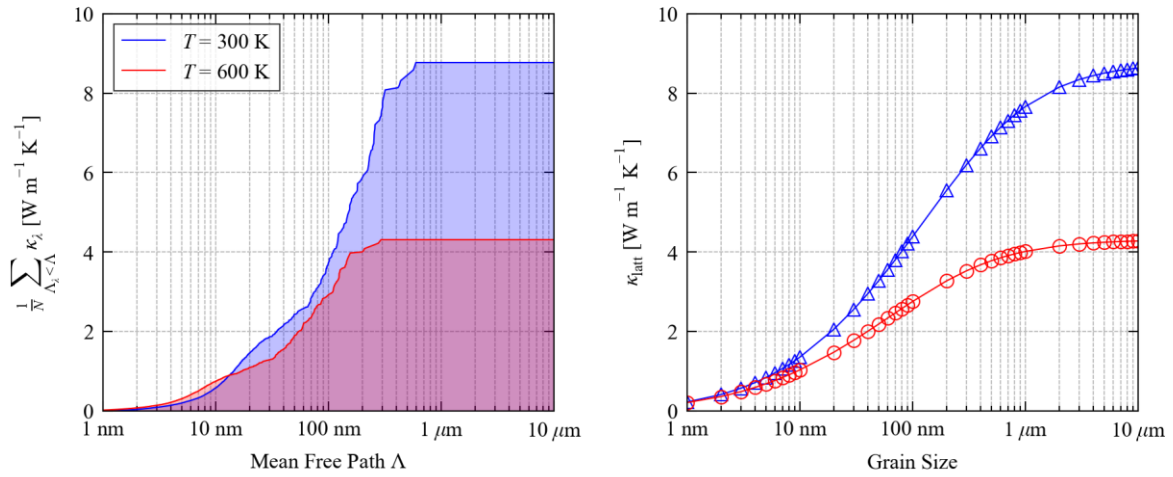
**Figure S2.25** (a) Accumulation of the thermal conductivity $\kappa_{latt}$ of HeCo$_8$Sb$_{24}$ as a function of the phonon mean-free path $\Lambda_\lambda = v_\lambda \tau_\lambda$ at $T = 300$ and 600 K (blue/red). (b) Estimated dependence of the $\kappa_{latt}$ at 300 and 600 K on the crystal grain size using a boundary-scattering model.
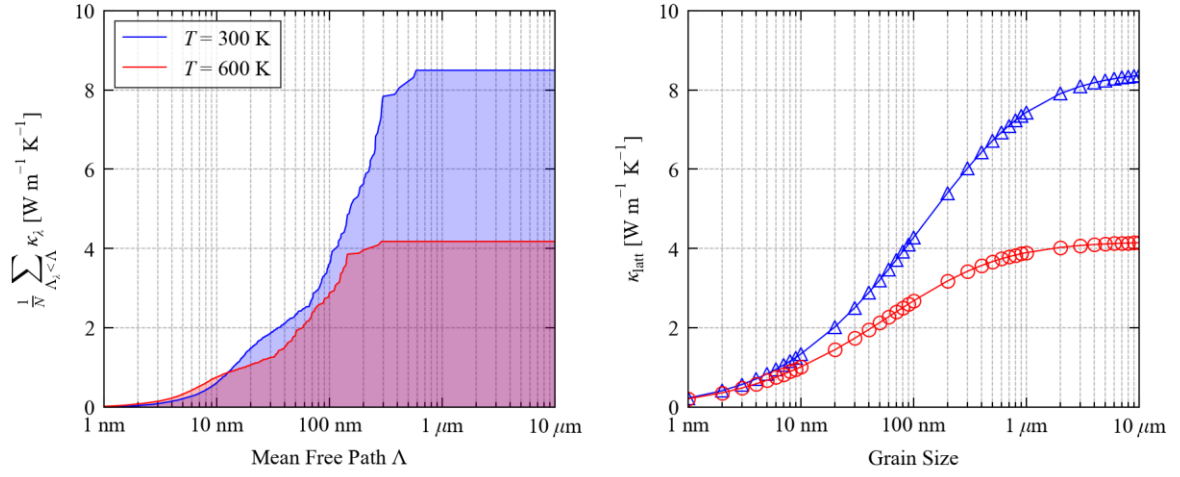


**Figure S2.26** (a) Accumulation of the thermal conductivity $\kappa_{latt}$ of NeCo$_8$Sb$_{24}$ as a function of the phonon mean-free path $\Lambda_\lambda = v_\lambda \tau_\lambda$ at $T = 300$ and 600 K (blue/red). (b) Estimated dependence of the $\kappa_{latt}$ at 300 and 600 K on the crystal grain size using a boundary-scattering model.
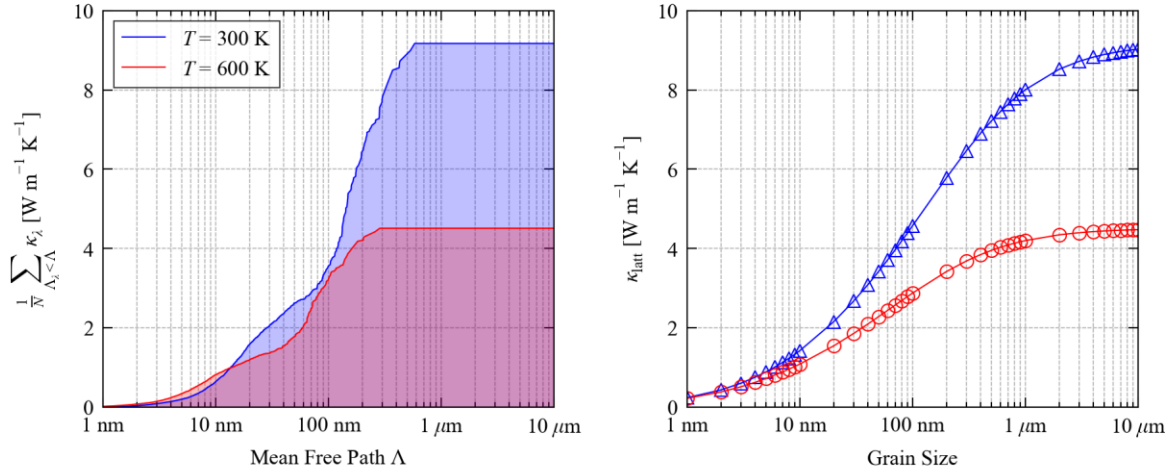
**Figure S2.27** (a) Accumulation of the thermal conductivity $\kappa_{latt}$ of ArCo$_8$Sb$_{24}$ as a function of the phonon mean-free path $\Lambda_\lambda = v_\lambda \tau_\lambda$ at $T = 300$ and 600 K (blue/red). (b) Estimated dependence of the $\kappa_{latt}$ at 300 and 600 K on the crystal grain size using a boundary-scattering model.



**Figure S2.28** (a) Accumulation of the thermal conductivity $\kappa_{latt}$ of KrCo$_8$Sb$_{24}$ as a function of the phonon mean-free path $\Lambda_\lambda = v_\lambda \tau_\lambda$ at $T = 300$ and 600 K (blue/red). (b) Estimated dependence of the $\kappa_{latt}$ at 300 and 600 K on the crystal grain size using a boundary-scattering model.

**Figure S2.29** (a) Accumulation of the thermal conductivity $\kappa_{\text{latt}}$ of $XeCo_8Sb_{24}$ as a function of the phonon mean-free path $\Lambda_\lambda = v_\lambda \tau_\lambda$ at $T = 300$ and $600$ K (blue/red). (b) Estimated dependence of the $\kappa_{\text{latt}}$ at 300 and 600 K on the crystal grain size using a boundary-scattering model.
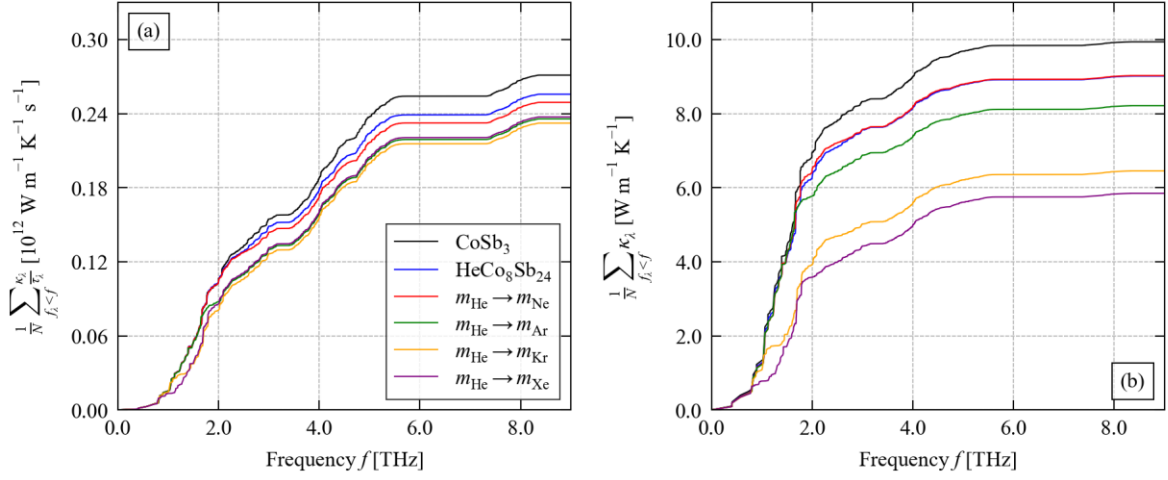
**Figure S2.30** Accumulation of the $\kappa_\lambda/\tau_\lambda$ (a) and $\kappa_\lambda$ (b) as a function of frequency at $T = 300$ K for pristine CoSb$_3$, HeCo$_8$Sb$_{24}$ and HeCo$_8$Sb$_{24}$ with the mass of the He atom $m_{\mathrm{He}}$ changed to the masses of Ne, Ar, Kr and Xe while keeping the force constants fixed.
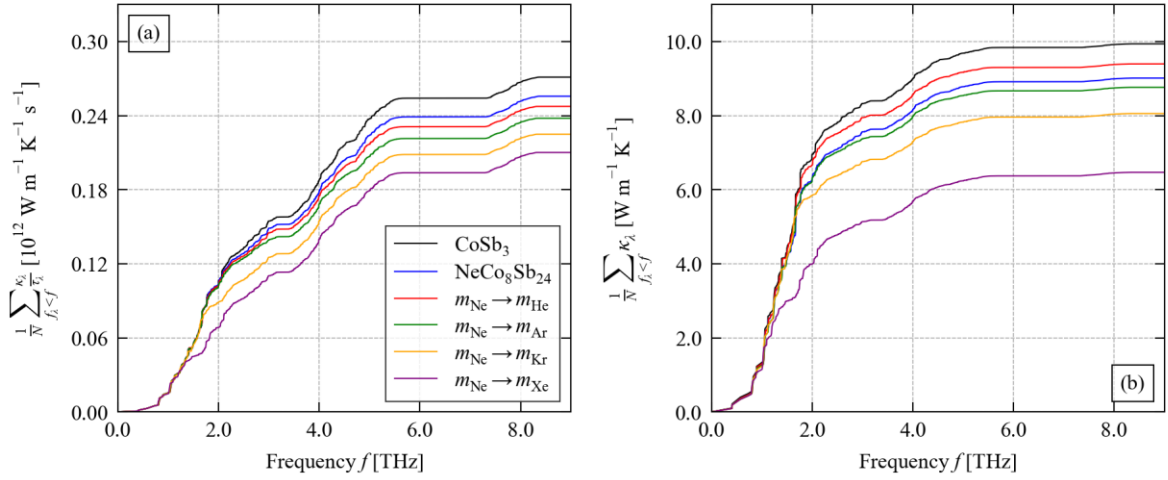


**Figure S2.31** Accumulation of the $\kappa_\lambda/\tau_\lambda$ (a) and $\kappa_\lambda$ (b) as a function of frequency at $T = 300$ K for pristine CoSb$_3$, NeCo$_8$Sb$_{24}$ and NeCo$_8$Sb$_{24}$ with the mass of the He atom $m_{\mathrm{Ne}}$ changed to the masses of He, Ar, Kr and Xe while keeping the force constants fixed.
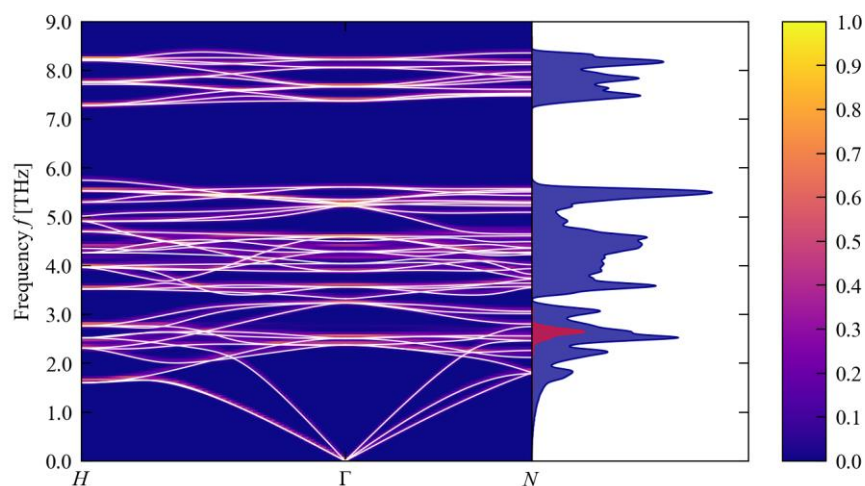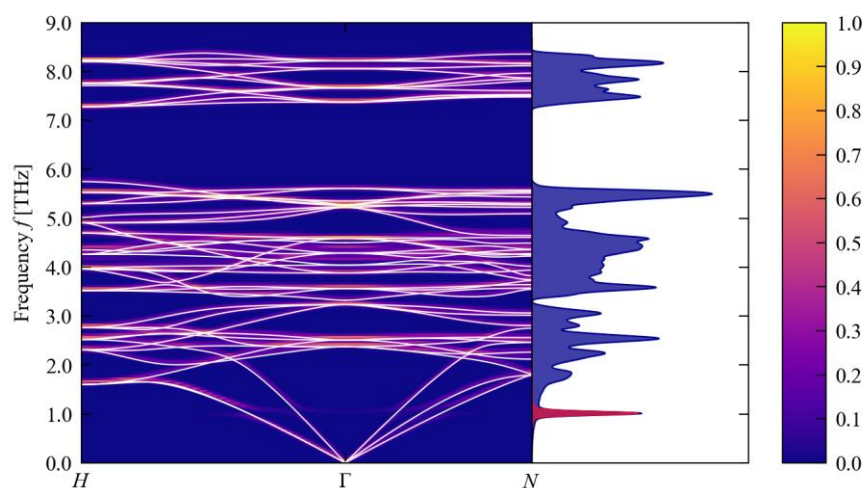
**Figure S2.32** Unfolded band dispersion and phonon density of states $g(f)$ (DoS) of $HeCo_8Sb_{24}$ with the mass of the He atom $m_{He}$ changed to the mass of Ne. The colour scale shows the spectral weights obtained from the band-unfolding procedure. The band structure of pristine $CoSb_3$ is overlaid on the dispersion in white, and the projection of the DoS onto the filler is overlaid on the $g(f)$ in red.
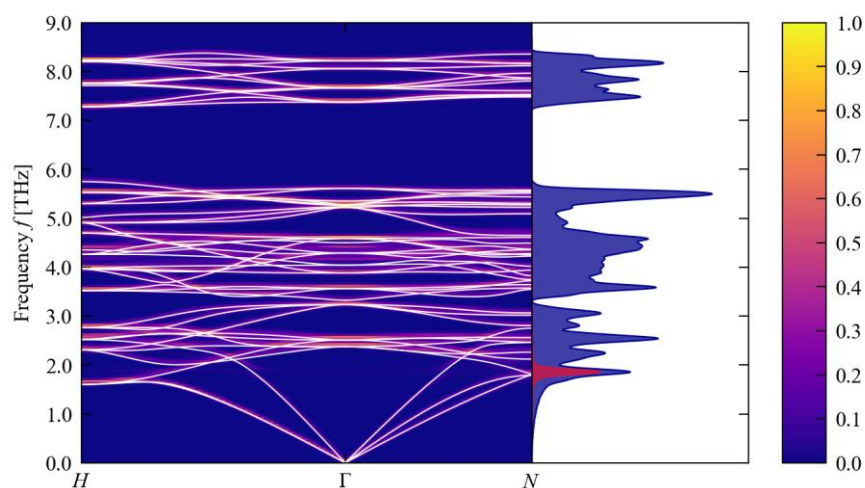


**Figure S2.33** Unfolded band dispersion and phonon density of states $g(f)$ (DoS) of $HeCo_8Sb_{24}$ with the mass of the He atom $m_{He}$ changed to the mass of Ar. The colour scale shows the spectral weights obtained from the band-unfolding procedure. The band structure of pristine $CoSb_3$ is overlaid on the dispersion in white, and the projection of the DoS onto the filler is overlaid on the $g(f)$ in red.
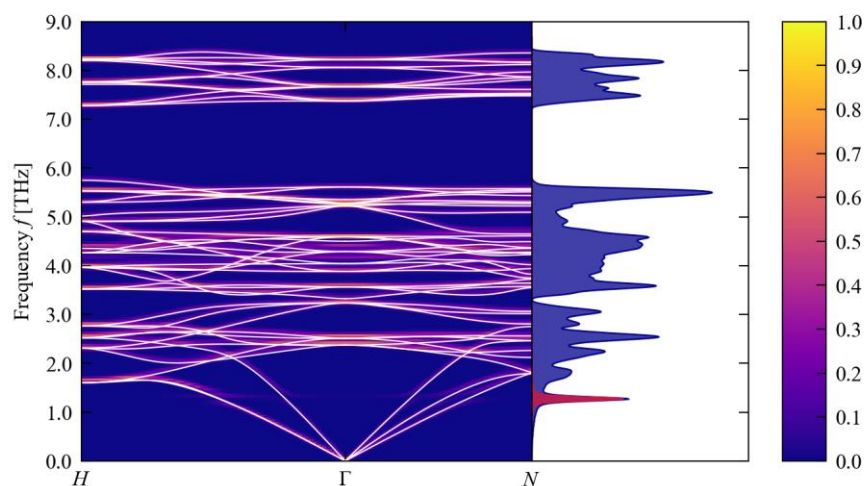
**Figure S2.34** Unfolded band dispersion and phonon density of states $g(f)$ (DoS) of HeCo$_8$Sb$_{24}$ with the mass of the He atom $m_{He}$ changed to the mass of Kr. The colour scale shows the spectral weights obtained from the band-unfolding procedure. The band structure of pristine CoSb$_3$ is overlaid on the dispersion in white, and the projection of the DoS onto the filler is overlaid on the $g(f)$ in red.



**Figure S2.35** Unfolded band dispersion and phonon density of states $g(f)$ (DoS) of HeCo$_8$Sb$_{24}$ with the mass of the He atom $m_{He}$ changed to the mass of Xe. The colour scale shows the spectral weights obtained from the band-unfolding procedure. The band structure of pristine CoSb$_3$ is overlaid on the dispersion in white, and the projection of the DoS onto the filler is overlaid on the $g(f)$ in red.